Towards an Effective Automated Interpretation Method for Modern Hydrocarbon Borehole Geophysical Images

A thesis presented for the degree of

DOCTOR OF PHILOSOPHY IN

GEOPHYSICS

by

ANGELEENA THOMAS

School of Geosciences

The University of Edinburgh

2012

Supervisors: Prof. Andrew Curtis and Dr. Malcolm Rider

Dedicated to my parents, my husband Anish and little Nathen…

Declaration

I herewith declare that all of the scientific works reported in this thesis are my own unless otherwise noted. None of this work has been submitted in any other application for a higher degree.

Angeleena Thomas

Abstract

Borehole imaging is one of the fastest and most precise methods for collecting subsurface data that provides high resolution information on layering, texture and dips, permitting a core-like description of the subsurface. Although the range of information recoverable from this technology is widely acknowledged, image logs are still used in a strictly qualitative manner. Interpreting image logs manually is cumbersome, time consuming and is subjective based on the experience of the interpreter. This thesis outlines new methods that automate image log interpretation and extract subsurface lithofacies information in a quantitative manner.

We developed two methodologies based on advanced image analysis techniques successfully employed in remote sensing and medical imaging. The first one is a pixel-based pattern recognition technique applying textural analysis to quantify image textural properties. These properties together with standard logs and core-derived lithofacies information are used to train a back propagation Neural Network. In principle the trained and tested Neural Network is applicable for automated borehole image interpretation from similar geological settings. However, this pixel-based approach fails to make use explicitly of the spatial characteristics of a high resolution image.

A second methodology is introduced which groups identical neighbouring pixels into objects. The resultant spectrally and spatially consistent objects are then related to geologically meaningful groups such as lithofacies by employing fuzzy classifiers. This method showed better results and is applied to outcrop photos, core photos and image logs, including a ‘difficult’ data set from a deviated well. The latter image log did not distinguish some of the conductive and resistive regions, as observed from standard logs and core photos. This is overcome by marking bed boundaries using standard logs. Bed orientations were estimated using an automated sinusoid fitting algorithm within a formal uncertainty framework in order to distinguish dipping beds and horizontal stratification. Integration of these derived logs in the methodology yields a complete automated lithofacies identification, even from the difficult dataset. The results were validated through the interpretation of cored intervals by a geologist.

This is a supervised classification method which incorporates the expertise of one or several geologists, and hence includes human logic, reasoning, and current knowledge of the field heterogeneity. By including multiple geologists in the training, the results become less dependent on each individual's subjectivity and prior experience. The method is also easily adaptable to other geological settings. In addition, it is applicable to several kinds of borehole images, for example wireline electrical borehole wall images, core photographs, and logging-while-drilling (LWD) images. Thus, the theme of this dissertation is the development of methodologies which makes image log interpretation simpler, faster, less subjective, and efficient such that it can be applied to large quantities of data.

Acknowledgements

First of all, I would like to thank my supervisors Prof. Andrew Curtis and Dr. Malcolm Rider for giving me the opportunity to work with them on this exciting project. It has been a great learning experience for me which I will cherish for a long time to come. Thank you Andrew and Malcolm, for your advice and support, especially during the difficult times.

I would like to thank Shell UK for sponsoring my PhD program through the Dorothy Hodgkin Postgraduate Award.

Many thanks to my initial supervisor, Dr. Roger Scrutton and the remote sensing expert, Alasdair Mac Arthur, I appreciate your help and guidance.

I would like to thank Shell and Melrose Resources for providing me the datasets.

I would like to thank my colleagues, for the stimulating and friendly atmosphere in the office. Thank you for your support.

Special thanks to Dr. John Owens, my industry mentor, for the many helpful discussions we had on the project. Thanks to Mike Mcgonigal, Melrose Resources Plc for the valuable inputs and insights to the dataset.

I would also like to thank all the members of staff at the School of Geosciences, your help and support was extremely valuable.

Finally, to the special people in my life; my parents Mr. N.T.Thomas and Dr. Saramma Thomas, thank you so much for all the love and support. Thank you, Anish, for your love and understanding during these tough years. This thesis is dedicated to you and our little Nathen.

Table of Contents

List of Tables

List of Figures

Chapter 1

TOWARDS AN EFFECTIVE AUTOMATED INTERPRETATION OF ELECTRICAL BOREHOLE IMAGES: AN INTRODUCTION

Summary: This chapter gives a brief introduction to the importance of lithofacies identification from geophysical logs, especially from 'image logs' and the significance of developing automated lithofacies identification from image logs. The chapter is concluded with a thesis outline introducing the following chapters in this thesis (section 1.2).

1.1 INTRODUCTION

The demand for energy is continually growing and fossil fuels are expected to continue supplying much of the energy used worldwide. This in turn necessitates an increase in the exploration and production of hydrocarbons leading to the development of both conventional and unconventional reservoirs around the world, and also maximizing recovery from existing fields. Hence, regardless of the hydrocarbon type, reservoir type or play type, the need for detailed reservoir evaluation is becoming increasingly important (Kuchinski and Kalathingal, 2010).

Each reservoir is unique with many forms of heterogeneity in the rock properties (Mirowski, 2005). Hence, in reservoir evaluation, understanding the form and spatial distribution of these heterogeneities is very important. Porosity, permeability and fluid saturation are the key variables for

characterizing a reservoir in order to estimate the volume of hydrocarbons and their flow patterns to optimize production of a field which are different for different rocks (Bhatt and Helle, 2002; Hruska et al., 2009). Hence, identification of lithofacies, which are the 'different rock types in a stratigraphic unit distinguishable based on their distinctive lithological properties, including composition, grain texture, bedding characteristics, sedimentary structures and biological features' (Bhatt, 2002), is an important task in knowing the heterogeneity of any reservoir.

The common practice in the oil industry is to manually examine various lithofacies identified on cores (actual rock samples retrieved from borehole) by expert geologists (Chikhi et al., 2005; Kraipeerapun et al., 2006). However, continuous coring, especially in today's environment of targeting very deep sub-sea reservoirs and drilling horizontal wells, is very expensive. Therefore, only the first few wells, or certain geological or depth intervals drilled in a field are usually cored (Blackbourn, 1990).

Geophysical logs - the continuous recording of geophysical parameters along the borehole - offer an indirect, less expensive way to measure rock properties. These logs are run in nearly every well drilled and it is very common to estimate lithofacies from them. Log signatures are initially correlated with available core and then used to estimate lithofacies from logs alone (Bhatt, 2002; Martin, 2004). Thus, modeling and propagating core description over uncored area from geophysical logs is important in any reservoir understanding (Mathis et al., 2004). This is done in many ways: manually examining well logs, using graphical techniques such as cross plotting (Bruke et al., 1969; Clavier and Rust, 1976; Rider, 2004) or by automated approaches using various statistical classification algorithms such as discriminant function analysis (Bush et al., 1987; Delfiner et al., 1987; Doveton, 1994), principal

component analysais (Luthi, 2001), fuzzy logic (Bagheri et al., 2005; Cuddy, 2000), clustering (Elphick and Moore, 1999; Gill et al., 1993; Martinius et al., 2002; Ye and Rabiller, 2000), and neural networks (Bhatt and Helle, 2002; Derek et al., 1990; Maiti et al., 2007; Martin, 2004; Roger et al., 1992; Wadge et al., 1998; Zhang et al., 1999). Though these studies showed reasonably good lithofacies classification from conventional geophysical logs; the low vertical resolution (2-4 ft or greater) limits their utility for characterizing fine-scale geological heterogeneity that may exist in the study area.

Down-hole tools are now available to acquire high resolution maps of the acoustic and electrical properties of the borehole wall and display them as computer generated images (hereafter referred to as image logs) of the formations encountered during drilling. These imaging tools sample the borehole wall many times both horizontally and vertically and hence the image has a wide coverage of the borehole wall (a detailed account of various borehole imaging tools, tool design, data acquisition, processing can be found in Schlumberger (1994), Cheung (1999), Lofts and Bourke (1999), Prensky (1999), Rider (2004) and Passey et al., (2006)). In reservoir evaluation, electrical borehole imaging is proving to be a useful tool providing critical information that complements evaluation tools such as seismics, core, cuttings logging, and formation testing (Poppelreiter et al., 2010). Nowadays, high definition electrical borehole images (image logs) are increasingly generated in all borehole conditions (Poppelreiter et al., 2010), even in oil-based mud drilling environments (Maddock and Ravnas, 2010), and which now form a large industrial data base.

The image logs used in this study were acquired using Schlumberger's Fullbore Formation MicroImager (FMI). The tool consists of four pads fixed to two orthogonal arms, each pad having a hinged flap to extend the area of

electrical contact and hence the circumferential borehole coverage (Goodall et al., 1998; Schlumberger, 1994). The device samples the formation via a large array of buttons (electrodes) attached to these pads and flaps that press against the borehole wall. Electrical current is forced into the rock through the electrodes, and remote sensors measure the current after it interacts with the formation (Hurley, 2004). These data form a dense matrix of measurements, which are displayed as a computer-generated image. In these images (image logs), each measurement corresponds to a pixel, the conductivity value of which defines its grayscale value or color (the series of processing steps by which the grayscale or color images are produced is detailed by Hurley (2004), and Harker *et al., (*1990), and Serra (1989)). A schematic diagram illustrating this process is given in figure 1.1.

While a standard geophysical log records only a single reading at each depth point, an image log covers the entire wall, for example FMI records 192 resistivity responses around the borehole wall at each depth with a vertical resolution of 0.0082 feet (0.25 cm) (Hurley, 2004; Rider, 2004). Hence, this image-log data permits a detailed description of layering, texture and dip of various thick and thin beds and can be considered as one of the best sources of data to derive even fine details of the reservoir (Chitale, 2005; Onu et al., 2008).

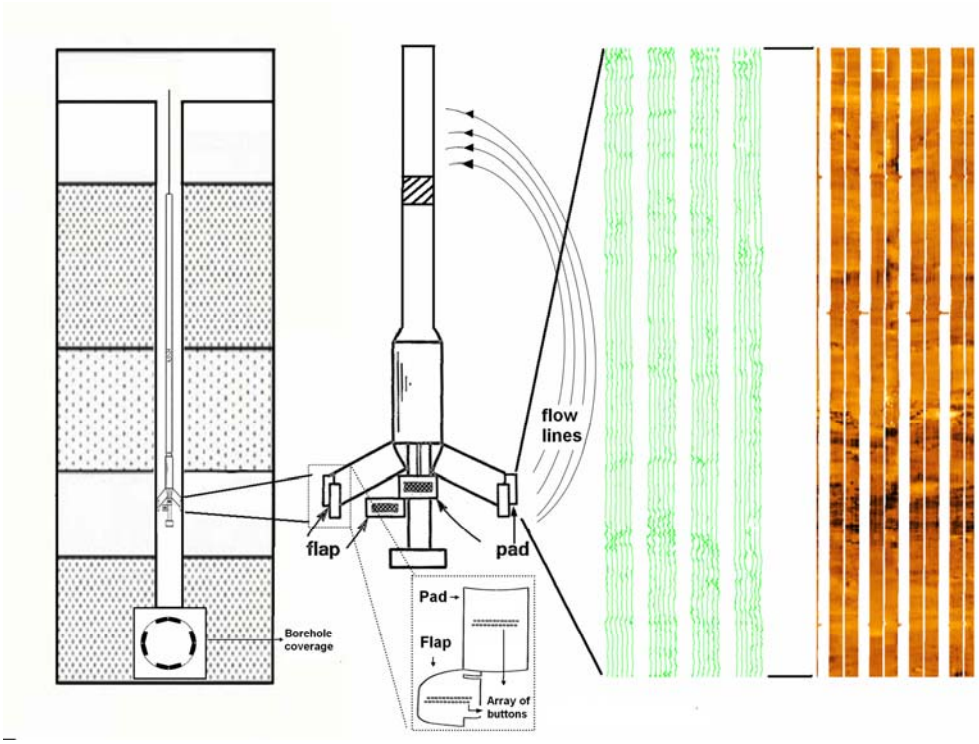

Figure 1.1*: Schematic diagram illustrating the acquisition of resistivity image using Formation MicroImager (FMI), the tool records formation resistivity variations which are translated into matrix and color coded. Figure also shows a schematic representation of the borehole coverage and Pad/flap arrangement and assemblage.*

The detail captured by image logs allows them to be used in many different ways (Martin, 2004). Mostly, the high resolution image logs are widely used in the industry in a strictly qualitative manner (visual interpretation). Experts interpret the image log visually and compare it with the signatures observed in standard logs and with details in core. Integration of borehole images and core data in a visual manner has proven to provide detailed stratigraphic information on carbonate platforms (Cooper et al., 1995), volcaniclastic sequences (Pezard et al., 1992), facies reconstruction of extrusive sequences (Bartetzko et al., 2003), and basement lithology (Barr et al., 2002). The

manual interpretation is efficient for analysis of small intervals but becomes tedious and time consuming when large amounts of data need to be interpreted. Interpretation can thus be both highly labor intensive and subjective. It is also possible for human errors to creep in when large amounts of data are interpreted manually - for example leaving some fine details of the formation unnoticed, such as thin beds which may be recorded in the image logs but not in standard logs due to their lower resolution. Hence, in visual interpretation, even though image logs are of high resolution and provide an exceptionally detailed description of the subsurface, there is a large gap between the theoretically available information and the information used in decision making processes. Also, the continual growth of the oil industry has lead to a rapid increase in the number of wells to be analyzed simultaneously. It is therefore important to develop interpretation methods that can incorporate any amount of data, reducing the amount of time necessary for each study (Knecht et al., 2003). Only an automated interpretation can serve this purpose. Moreover, the results of an automated method become objective, consistent, and reproducible.

Different approaches have been made to automate and quantify information from borehole images. To date, quantitative interpretation methods extract information directly from the resistivity measurements themselves (Delhomme, 1992; Tyagi and Bhaduri, 2002), derive structural features like orientation data from image logs (Antoine and Delhomme, 1990; Haller and Porturas, 1998; Luthi, 1990; Prensky, 1999; Russell et al., 2002; Ye et al., 1997a; Ye et al., 1997b), or perform fracture analysis (Ke, 2008; Ozkaya, 2003; Prioul and Jocker, 2009; Thapa et al., 1997). Much additional information can be extracted from the image logs as a whole and consequently many borehole image interpretation packages are available. However, these packages mainly contain utilities for image display for small intervals of data,

interactive picking of planar events, computation of plane orientations, calculation of petrophysical quantities, unsupervised image quantification and the presentation of summary statistics. Hence, they do not obviate the need for the labor intensive visual interpretation of image logs, a widely accepted routine in the industry.

Image logs are created by assigning color maps to different ranges of resistivity values, and these colored pixels are properly arranged in their geometric position around the borehole wall (Hurley, 2004). Since, resistivity is a function of both rocks and included fluids[] in place, it can provide information on lithofacies[†] types (Reid and Enderlin, 1998). Convention dictates that dark colour indicates relatively electrically conductive features such as shale or fluid-filled fractures while light colour (shades of brown, yellow and white) represents relatively resistive features, such as sandstone or limestone (Hurley and Zhang, 2009a; Passey et al., 2006). In addition there are pattern/texture[‡] variations corresponding to geological heterogeneity like cross-beds, ripple beds, planar lamination and bioturbation (Chen et al., 2001; Geng et al., 2002; Hua et al., 2009; Leduc et al., 2002; Li and Zhou, 2008; Linek, 2003). Based on these image properties the image interpreter visually interprets lithofacies from an image log. Thus, in principle, these image

[] *Most rock materials are insulators (resist the passage of electric current), while their enclosed fluids are conductors, except hydrocarbons which are resistive. For example, when a formation is porous and contains salty water, the overall resistivity will be low however, if the same formation contains hydrocarbons, its resistivity will be high (Malcolm, 2004).*

[†] *Lithofacies from image log are equivalent but not identical to the lithofacies inferred from core. The latter are obtained directly from the visible features of rocks whereas lithofacies from image logs are defined by attributes derived from image logs.*

[‡] *Texture defined from the image log is not same as the geologists' texture (Delhomme, J. P., (1992)): from a geological point of view, texture could be defined as the spatial relationship of geological objects observed on an image, while in an image analysis point of view, texture is the spatial organization of color or grey levels on an image (Ye et. al., (1998)) hence, represents the geometrical aspects of the component particles of a rock*

characteristics can be linked to different lithofacies in the core and to train a classification algorithm in order to develop an automated image log interpretation which could result in an analogous classification obtained by visual manual interpretation.

There exist a number of attempts to automate textural feature extraction from image logs. Delhomme (1992) applied mathematical morphology (Serra, 1982) for image segmentation to quantify resistivity heterogeneity. Textural segmentation based on Law's energy (Laws, 1980) was implemented by Luthi (1994), in which, the image is filtered by assigned texture masks and the resulting variance between mask and image is studied to classify bedding units. Harris et al., (1993), Hall et. al., (1996) and Linek *et* al., (2007) derived texture features from image logs using pattern recognition analysis employing a co-occurrence matrix (Haralick et al., 1973) and assigned the texture features to each rock class. But all of these different approaches are made to extract different parameters from image logs or directly from the resistivity measurements to achieve image log interpretation. However, the properties of the image logs can be spatially variable and irregular in texture, shape and size (Chitale, 2005; Hua et al., 2009). Hence, these kinds of texture feature quantification which result in average single or a number of single image properties for each depth are not an actual representation of the detail recorded in the image log. A meaningful image log quantification method should go beyond extracting an average image property for each depth. It should take into consideration the spatial variations in spectral and textural property in the image log which could quantify the geological heterogeneity around as well as along the borehole.

Properties vary from field to field, between wells within a field, and even with depth within a single well due to the difference in depositional systems and

environment, temperature, pressure, compaction, etc. Hence, each well is unique and there are local factors that may affect the data in unexpected ways. Hence, associating down-hole logs to various lithofacies classes based on simplified theoretical analysis and data clustering (Chang et al., 2002; Knecht et al., 2003; Machecler and Nadal, 2004; Mathis et al., 2004; Ye et al., 1998) which excludes the local geological knowledge is risky (Mirowski, 2005). A solution to this issue is to incorporate both the power of computers and the expertise of one or more geologists in an automated image log interpretation.

Hua et. al., (2009) presented nine typical borehole image interpretation patterns based on his studies and previous studies by Chen et al., (2001), Geng et al., (2002), Leduc et al., (2002), Li and Zhou, (2008), and Linek (2003) to automatically classify various lithofacies from image logs. Though this study took into account the spatial property of the patterns characterising various lithofacies and could deal with image properties in image log depth, adapting to new fields is difficult as each field is unique and hence, each differs in the lithofacies pattern. Also, the same pattern could represent different classes, for example carbonate cement and structureless sand could result in the 'block pattern' defined by Hua et al., (2009) while both could be easily distinguished if spectral properties are also considered. Hence, one should consider all relevant image properties such as spectral, textural and spatial properties rather than a lithofacies classification based on any one image property. Further, pre-defined properties may not be an apt solution for any geological classification. The usage of image properties should be flexible according to data and field requirements. For example, a simple sand shale sequence could be distinguishable based on a spectral property alone. However, a combination of all features is needed in most other cases. Also, the methods presented by Hua et.al., (2009) rely on image logs alone. There may be situations when image

log data cannot stand alone due to poor image log quality. In such cases, both image log and conventional logs need to be combined or evaluated together for a successful lithofacies classification of the reservoir. Chitale (2005) gives a detailed explanation of reservoir characterization goals that could be achieved from image logs alone and by combining image logs with other open hole logs.

By integrating all necessary data, the interpreter may not be biased by the signatures of any one data type. For example, in evaluating thin bed reservoirs, conventional logs will only give an average of volumetric properties/bulk petrophysical properties (Knecht et al., 2004) while the image logs can provide high resolution information on layering, texture and dip of rocks and subsurface sediments (Chitale, 2005). On the other hand, gamma logs are good indicators of shale (Martin, 2004) while caliper logs give detail about borehole conditions and hence could explain why image logs show strange responses at areas of borehole washouts (Linek et al., 2007). Thus, a proper integration of electrical images with conventional logs can provide an extremely powerful tool for reservoir characterization.

This is similar to some extent to the visual interpretation of image logs, where geologists compare the properties in image logs with standard logs. In so doing, the information from one data type compliments the other for a more accurate classification. Hence, unlike the various automated lithofacies identification methods proposed in literature, from standard logs alone (Bagheri et al., 2005; Bhatt and Helle, 2002; Chang et al., 2000; Chikhi et al., 2005; Dubois et al., 2005; Kraipeerapun et al., 2006; Maiti et al., 2007; Mirowski, 2005), from image logs alone (Hruska et al., 2009; Hua et al., 2009; Kowalik et al., 2009), and from image-derived logs alone (Linek et al., 2007; Mathis et al., 2003), we wish to integrate the wealth of information from

standard logs, image, and image derived logs. We therefore need to combine data of different resolutions (high resolution image log with low resolution standard logs) and dimensions (2-dimensional image log with 1-dimensional standard log). The integration of different resolution data can be approached in two ways, either up-scaling the high resolution image log and core data to the low resolution conventional log data, which is the standard petrophysical procedure (Knecht et al., 2004) or by downscaling the conventional log to high resolution image log and thus retaining the fine details of the formation recorded in the image log, as approached in this study. Similarly the integration of different dimensions of data can be approached in two different ways, either taking an averaged image log and hence the formation resistivity response at each depth and combine it with conventional logs, thus compromising the spatial importance of irregular textural features in the image log (Martin, 2004) or imaging the one dimensional conventional logs and depth matching with image logs hence, preserving the actual spectral, spatial and textural details of the subsurface recorded in the image log. This evaluation of data in two-dimensions enables the visualization of the exact arrangement of lithofacies in the reservoir compared to the modeled lithofacies prediction quantified from one dimensional image log properties and conventional logs, and can be more accurate in depth and bed boundary definition. Both approaches have been attempted in this study. Thus, the central theme of this thesis is an attempt to develop an automated lithofacies identification method from image logs, affecting a shift from human interactive qualitative interpretation to quantitative automated image log interpretation.

Summary of main questions addressed in this research:

- How can we develop an automated image log interpretation method which could yield much simpler and faster results in comparison to manual identification?

- How can we perform an effective integration of standard logs with the image log whenever necessary for a better image log interpretation, without losing the image log resolution and hence the fine details recorded in the image log?

- How can we include the expertise of one or more image interpreters and thus local geological knowledge in the classification scheme?

- How can we develop a classification scheme which is easily adaptable to different geological settings?

1.2 THESIS OUTLINE

Chapter 1: "Towards an Effective Automated Interpretation of Electrical Borehole Images: An Introduction"; gives the rationale behind this study.

Chapter 2: "Methodology"; gives a brief introduction to the two different types of methods investigated to address these research questions.

Chapter 3: "Automated Lithofacies Identification from Electrical Borehole Images – Neural Network Approach": illustrates a case study employing neural networks for automated lithofacies identification from image logs. Quantitative textural information extracted from image logs along with

interpolated standard logs and local geological knowledge derived from core were used to train the neural network.

Chapter 4: “An Introduction to Object-Based Image Analysis –Outcrop Photograph Analysis”: an introduction to object-based image analysis is given by applying the methodology to classify an outcrop photograph which has a ‘ground truth’ interpretation from a geologist for automated lithology classification.

Chapter 5: “Automated Lithology Extraction from Core Photographs”: the object-based image analysis methodology is extended to core photograph analysis for an automated lithology classification. A one-to-one comparison of the automated lithology classification is made with the ground truth obtained by a qualitative visual core photograph interpretation by the geologist.

Chapter 6: “Automated Lithofacies Identification from Electrical Borehole Images”: given the success of the outcrop and core photograph classification in chapters 4 and 5, the object based image analysis methodology is applied to provide an automated image log classification.

Chapter 7: “Automated Lithofacies Identification from Electrical Borehole Images – An Interpretation of a ‘Difficult’ Data Set from a Deviated Well”: the application of the developed methodology using object-based image analysis is further applied on a ‘difficult’ data set from a deviated well. The difficulty arises in distinguishing various beds from the image log alone, and we overcome these difficulties by application of various filters derived both from standard logs and image logs.

Chapter 8: “Conclusions”: details the conclusions and inferences from this research, along with suggestions for future work.

Chapter 2

METHODOLOGY

Summary: The objective of this study is to develop an automated method to extract lithofacies information from image logs. This has been approached in two different ways. (1) Textural features are extracted from image logs at pixel level. A neural network classifier is used to classify the image log based on the extracted information from image logs along with standard logs and local geological knowledge derived from core (section 2.2). (2) Similar neighboring pixels in the image log are grouped together as image-objects; their spatial, spectral and textural features are assessed and classified them into appropriate lithofacies classes based on their similarity using fuzzy set classifiers (section 2.3). Each of these methods is explained separately in this chapter. The chapter concludes with the method that is used to assess the accuracy of the automated classification result by comparing it to the ground truth, which in this study is the independent interpretation by a geologist entirely based on core photographs (section 2.4).

2.1 INTRODUCTION

Automated classification of any image type proceeds in two main steps. First, features that could distinguish different classes present in the image (eg: roads, buildings and vegetation in a satellite picture, various lithofacies from image log in this study, etc.) are extracted. Then an appropriate classification algorithm can be used to classify the image into corresponding classes based on their distinctive features.

Hence, feature extraction is a key function in various image processing applications. A feature is an image characteristic that can capture certain visual properties of the image. For example, texture is an important feature

of many image types, which is the pattern of information or arrangement of the structure found in a picture. Spectral variation is another feature. These features can be extracted in several ways and are used in different applications such as remote sensing, and medical imaging.

In chapter one, it is seen that image logs provide a detailed description of the subsurface, in terms of colour coded resistivity responses of various lithofacies (rock types). Hence, the features recorded in the image log can be related to the local geological heterogeneity (lithofacies, in this study) for a meaningful image log classification. This has been approached in two different ways and two methodologies for an automated image log classification are introduced.

1. Features were extracted from the image log at pixel level and used to train a neural network classification algorithm for an automated lithofacies classification.

2. Features were extracted from the image log at image-object level (similar, neighboring pixels grouped together as an image-object) and used in a fuzzy set classification algorithm for an automated lithofacies classification.

Each of these methodologies is explained below.

2.2 METHODOLOGY 1

2.2.1 Feature Extraction from Image Logs Using Gray Level Co-Occurrence Matrix (GLCM) Method

Electrical borehole wall images are generated from the resistivity measurements recorded at the borehole wall. Each measurement corresponds

to a pixel, the conductivity value of which defines its grayscale value or color. The variations in grayscale value or color create pattern/texture corresponding to borehole heterogeneities such as lithofacies. Hence, these textures play an important role in image log classification. In order to progress from qualitative and subjective to quantitative and objective image interpretation, these textural features need to be quantified (Linek et al., 2007).

Among various approaches of quantifying textural features from images, the most common method is the Gray Level Co-occurrence Matrix (GLCM) based measurements (Wang and Georganas, 2009), used widely in image processing and remote sensing (Roumi, 2009). The Grey-Level Co-occurrence Matrix texture measurements have been the workhorse of image texture since they were proposed by Haralick in the 1970s. This texture recognition aims to classify images based on statistical information which is a function of spatial variation in grey level intensities (Van De Wouver, 1998). The main steps in texture feature extraction from an image using this methodology are;

(a) GLCM creation

(b) Calculating texture features from GLCM

(a) GLCM Creation

The GLCM is a tabulation of how often different combinations of pixel pairs occur in an image. That is, it considers the relationship between two pixels at a time, called the reference *'i'* and the neighbor pixel *'j'* (Horng et al., 2003). The main steps involved in creating a GLCM are given below

1. Assign the spatial relation between *i* and *j*
2. Counting the occurrences of pixel pairs and fill in the framework matrix

3. Add the matrix to its transpose to make it symmetrical
4. Normalize the matrix to turn it into probabilities.

A different co-occurrence matrix exists for each spatial relationship, defined by the displacement vector *d (*the inter pixel distance) and orientation θ (horizontal (*θ=0)*, vertical (*θ=-90)* and two diagonal *(θ=-45 and -135)*). The occurrences of pixel pairs are counted and then fill the frame-work as shown in figure 2.1, where $d = 1$ and $\theta = 0^0$. Each pixel within the window becomes the reference pixel in turn, starting in the upper left corner and proceeding to the lower right. The top left cell will be filled with the number of times the combination 1, 1 occurs and so on.

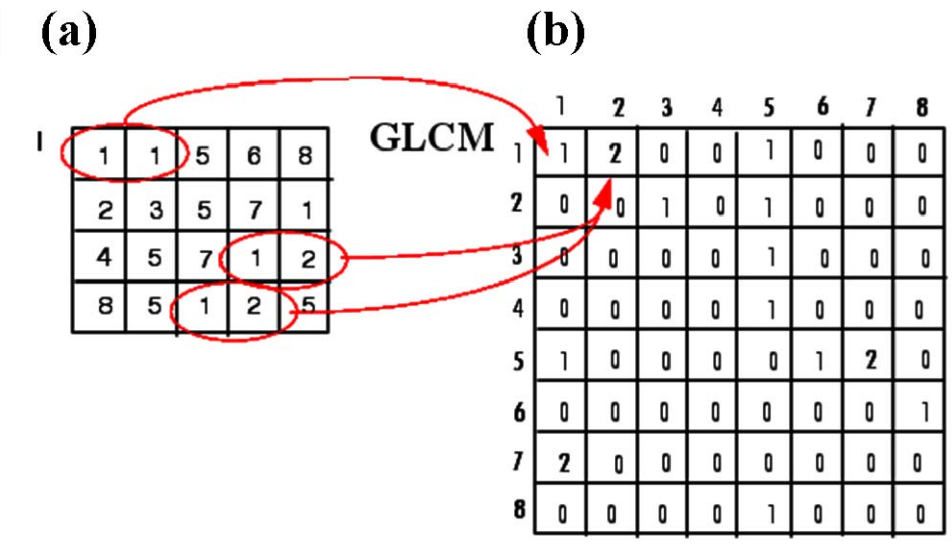

Figure 2. 1 : *Creation of co-occurrence matrix (a) image matrix, (b) tabulation of occurrence of pixel pairs for d = 1 and $\theta = 0^0$*

The texture calculations require a symmetrical matrix. A symmetrical matrix means that the same values occur in cells on opposite sides of the diagonal. For example, the value in cell 3,2 would be the same as the value in cell 2,3.

For this we add the matrix to its transpose. That is, if $C_{i,j}$ is the GLCM representing the co occurrence of the grey values at pixels *i* and *j* separated by the fixed distance *d* and direction *θ,* then the symmetrical GLCM will be,

$$V_{i,j} = \quad C_{i,j} + C^{T}_{i,j} \tag{2.1}$$

The measures require that each GLCM cell contain not a count, but rather a probability. The simplest definition of the probability of a given outcome is "the number of times this outcome occurs, divided by the total number of possible outcomes". This process is called normalizing the matrix. The Normalized GLCM $P_{i,j}$ is given by,

$$P_{i,j} = \quad \frac{V_{i,j}}{\sum_{i,j=0}^{N-1} V_{i,j}} \tag{2.2}$$

Thus, each element *(i, j)* in the GLCM represents an estimate of the probability of the presence of the two pixel pairs with a specified displacement *d* and orientation *θ.* Textural features are extracted from the GLCM.

(b) Calculating Texture Measures from GLCM:

Haralick et. al., (1973) defined texture features which contain the information about the image such as homogeneity, contrast and are used in many applications such as biological applications and image retrieval (Roumi, 2009). Common co-occurrence parameters, known as Haralick texture features are listed in table 1.

Contrast (*C*)	$C = \sum_{i,j=0}^{N-1} P_{i,j}(i-j)^2$
Dissimilarity (D)	$D = \sum_{i,j=0}^{N-1} P_{i,j} \mid i-j \mid$
Homogeneity (H)	$H = \sum_{i,j=0}^{N-1} \frac{P_{i,j}}{1+(i-j)^2}$
*A*ngular Second Moment *(A)*	$A = \sum_{i,j=0}^{N-1} P_{i,j}^{\ 2}$
Energy *(E)*	$E = \sqrt{\sum_{i,j=0}^{N-1} P_{i,j}^{\ 2}}$
Entropy *(EN)*	$EN = P_{i,j}(-\ln P_{i,j})$
GLCM Mean (μ)	$\mu_i = \sum_{i,j=0}^{N-1} i(P_{i,j})$; $\mu_j = \sum_{i,j=0}^{N-1} j(P_{i,j})$
GLCM Variance *(σ)*	$\sigma_i^{\ 2} = \sum_{i,j=0}^{N-1} P_{i,j}(i-\mu_i)^2$; $\sigma_j^{\ 2} = \sum_{i,j=0}^{N-1} P_{i,j}(i-\mu_j)$
Correlation (*CO)*	$CO = \sum_{i,j=0}^{N-1} P_{i.j}[\frac{(i-\mu_i)(i-\mu_j)}{\sqrt{(\sigma_i^2)(\sigma_j^2)}}]$

Table 2.1*: Haralick texture features*

The calculated texture value from a GLCM is a single number. In an image log, a sliding window is designed to calculate textural features from the

entire image and they are used to train a neural network along with interpolated geophysical logs.

2.2.2 Neural Network

Artificial Intelligence is defined as 'the study of how to make computers do things which, at the moment, people do better' (Rich and Knight, 1991). Neural networks process information in a similar way the human brain does. The network is composed of a large number of highly interconnected processing elements (neurones) working in parallel to solve a specific problem. For example, in the human brain, a typical neuron (figure 2.2) collects signals from others through a host of fine structures called dendrites. The neuron sends out spikes of electrical activity through a long, thin strand known as an axon, which splits into thousands of branches. At the end of each branch, a structure called a synapse converts the activity from the axon into electrical effects that inhibit or excite activity in the connected neurons. When a neuron receives excitatory input that is sufficiently large compared with the inhibitory input, it sends a spike of electrical activity down its axon. Learning occurs by changing the effectiveness of the synapse so that the influence of one neuron on another changes.

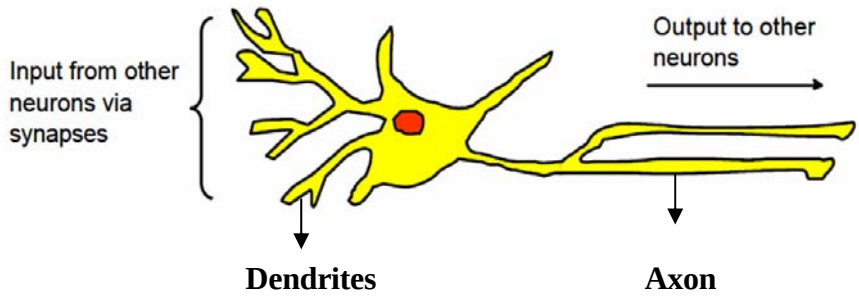

***Figure 2.2**: A simplified animal neuron*

Similarly, in an artificial neural network, inputs simulate the signals that a neuron gets, while the output simulates the response which the neuron generates. The synapse of the neuron is modelled as weights. The strength of the connection between an input and a neuron is noted by the value of the weight. The output is calculated by adding all inputs which are multiplied with their respective weights. This output of the neuron is then scaled to a number between 0 and 1 using an activation function, which controls its amplitude.

Consider a simple neuron with two inputs x_1 and x_2, with weights w_1 and w_2 and one output y as shown in figure 2.3 (a). Each neuron is composed of two units as shown in figure 2.3 (b). First unit (summing junction) adds products of weights and input signals and the adder output signal e is given by,

$$e = w_1 x_1 + w_2 x_2 \tag{2.3}$$

The second unit (neuron activation function) controls the amplitude of the output of the neuron and normally scales it to a number between 0 and 1 (it is also called squashing function). The output signal, y, of neuron can be given by,

$$y = f(e) \tag{2.4}$$

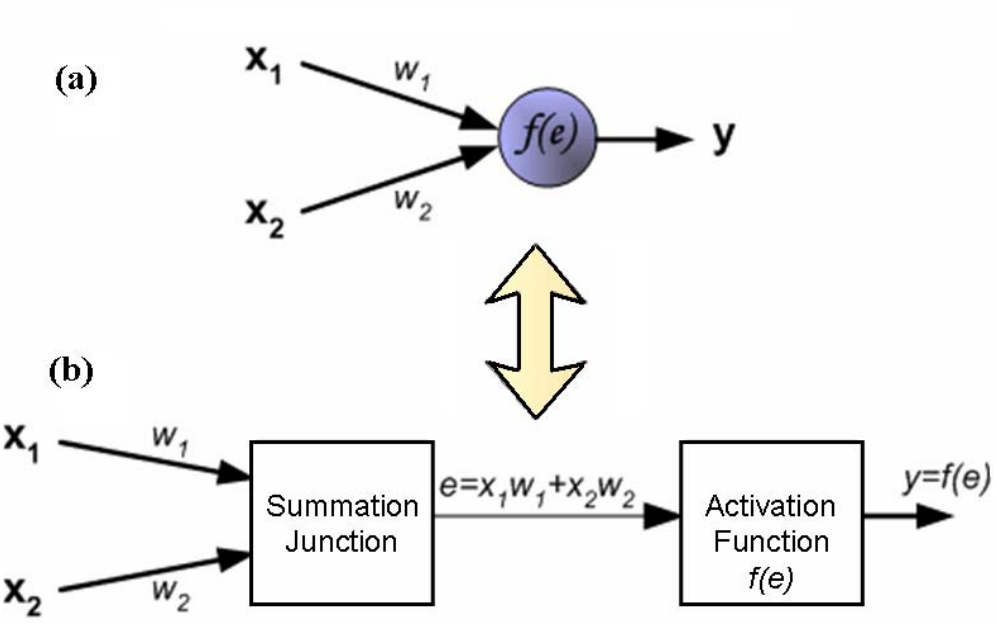

***Figure 2.3**: Figure explaining the activity within the neuron; the summation junction adds products of input signals and their respective weights and activation function controls the amplitude of the neuron output.*

The generally used activation functions are step, sign or sigmoid functions which are shown in figure 2.4 and are defined mathematically in table 2.2,

$$Step\,(x) = 1 if\ x \geq t, else\ 0$$

$$Sign\,(x) = {}^{+}1 if\ x \geq 0, else\ 0$$

$$Sigmoid\,(x) = \frac{1}{1+e^{-a\,x}}$$

where, *a* is a constant and is usually chosen between 0.5 and 2.

***Table 2.2**: Mathematical definition of various activation functions*

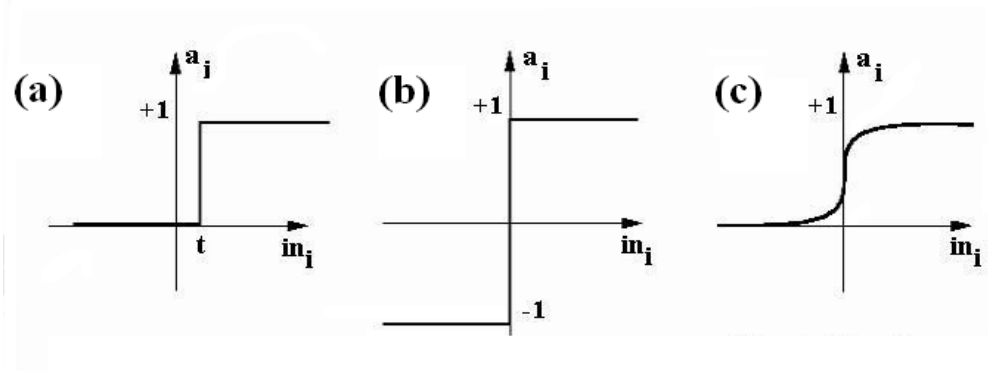

***Figure 2.4**: Common activation functions used in neural network (a) Step function, (b) Sign function, and (c) Sigmoid function*

A neural network is a group of neurons connected together. Connecting neurons to form a neural network can be done in various ways. In this study a forward connection neural network (shown in figure 2.5) has been used. There exist a number of literatures that describe the basic theory of neural networks. Gurney (1997) provides a useful conceptual introduction to the topic; Bishop (1996) provides an overview of neural networks from a statistical and pattern-recognition perspective; and Masters (1993) provides an account of how to successfully implement various algorithms.

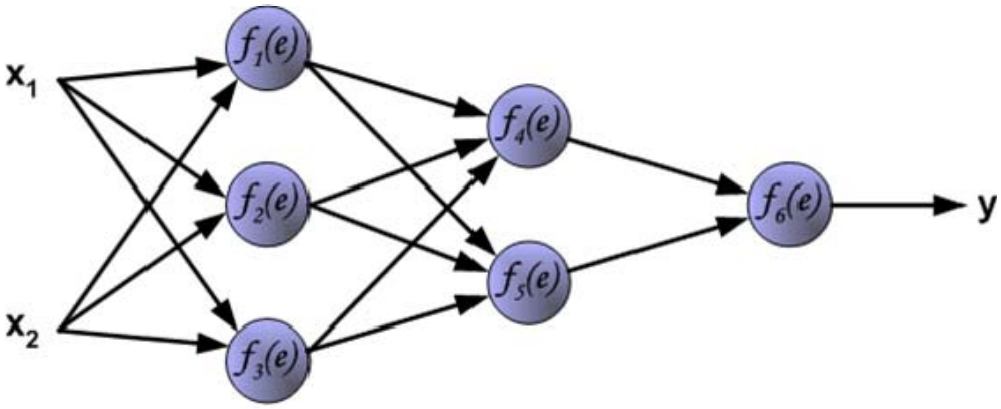

***Figure 2.5**: An example of a neural network*

The neural network package Easynn (http://www.easynn.com) is used in this study to classify lithofacies from well logs. This program implements the 'backpropagation algorithm' with a sigmoid squashing function. The backpropagation algorithm is the most researched, and therefore the most widely understood in neural network studies (Rojas, 1996). This is a supervised neural network, that is, a set of inputs ($x_{i;}$ *i=1,2,3,..,number of inputs*) are presented to the neural network with their corresponding desired output (z). The network learns the relationship between the input and output based on this given training data set, which is an iterative process. In each iteration an error is composed from the difference between the desired response (z) and the system output *(y)*. This error information is fed back to the system and adjusts the weights of each neuron in a systematic fashion. This process is repeated until the performance is acceptable, which is defined either when the error is very minimum or below a defined threshold or when the defined number of iterations finishes (learning fails in that case). Thus, a backpropagation algorithm would perform well when the combination of weights minimises the error function. This is achieved using a sigmoid activation function, explained earlier in this section. A detailed explanation of the backpropagation algorithm can be found in Mitchell (1997).

In this study the inputs to the neural network are the features extracted from the image log and the conventional geophysical logs. A trained and tested Neural Network, in principle, is applicable for automated lithofacies identification from borehole at depth intervals outside the training interval and also on data from similar geological settings.

2.3 METHODOLOGY 2

AN OVERVIEW OF OBJECT BASED IMAGE ANALYSIS

Image analysis is the extraction of meaningful information from digital images. An Object-Based Image Analysis (OBIA) means partitioning imagery into meaningful image-objects, assessing their characteristics through spatial, spectral and temporal scale and classifying them into appropriate classes based on their similarity. This is one of the most advanced commonly used image interpretation methodologies in remote sensing and medical imaging.

The main steps involved in this process include

- Image segmentation
- Knowledge-base design
- Image classification

Once the parameters that influence each of these steps are finalised through experimentation on the images given for the intended purpose (presented in coming chapters), all of it can be coded into a protocol so that it can be used for automated image classification of any other similar images.

Each of these individual steps is described in detail, below.

2.3.1 Image Segmentation

This is a process of partitioning an image into non-overlapping regions (Schiewe, 2002) A multi-resolution segmentation algorithm developed by Baatz and Schape (2000) is used for image segmentation, which is a region-merging technique that starts with single-pixel objects. In subsequent iterative steps, adjacent pixels are merged into larger objects, based on the

predefined spectral, and shape parameters, such that it defines the smallest growth in heterogeneity within each object (Gamanya et al., 2007).

Spectral parameter, $h_{Spectral}$ is a measure of the change in object heterogeneity resulting from the potential merge of two adjacent objects, and is defined by the standard deviations of spectral values, σ. When a possible merge of a pair of image objects, say *Obj1* and *Obj2,* is considered, then their σ, σ_{Obj1} *and* $\sigma_{Obj2,}$ are weighted by the object sizes, n_{Obj1} and n_{Obj2}. Hence the resultant $h_{Spectral}$ after the merge of *Obj1* and *Obj2*:

$$h_{Spectral} = n_{Merge} \cdot \sigma_{Merge} - (n_{Obj1} \cdot \sigma_{Obj1} - n_{Obj2} . \sigma_{Obj2}) \qquad (2.5)$$

where, n_{Merge} is the size and σ_{Merge} is the standard deviation of spectral values of the new object formed.

Shape parameter, h_{Shape} is the heterogeneity change due to the change in object shape before and after the merge and is described by two factors, compactness and smoothness:

$$h_{Shape} = w_{compact} . h_{compact} + (1 - w_{compact}) . h_{smooth} \qquad (2.6)$$

where, w is a weighting parameter, $0 \leq w \leq 1$. Compactness is a function of object perimeter, *l,* and the number of pixels, *n,* within the object, whereas smoothness is a function of object perimeter and the perimeter of the object's bounding box, *b*.

$$h_{smooth} = n_{Merge} \cdot \left(\frac{l_{Merge}}{b_{Merge}} \right) - \left[n_{Obj1} \cdot \left(\frac{l_{Obj1}}{b_{Obj1}} \right) + n_{Obj2} \cdot \left(\frac{l_{Obj2}}{b_{Obj2}} \right) \right] \qquad (2.7)$$

$$h_{compact} = n_{Merge} \cdot \left(\frac{l_{Merge}}{\sqrt{n_{Merge}}} \right) - \left[n_{Obj1} \cdot \left(\frac{l_{Obj1}}{\sqrt{n_{Obj1}}} \right) + n_{Obj2} \cdot \left(\frac{l_{Obj2}}{\sqrt{n_{Obj2}}} \right) \right] \quad (2.8)$$

The $h_{Spectral}$ and h_{Shape} can be reduced to a single value, called 'fusion' values, f, which is indicative of the overall heterogeneity change (Zhang and Maxwell, 2006) and is defined by

$$f = (1-w)h_{Spectral} + w \cdot h_{Shape} \quad (2.9)$$

Here w is a weighting parameter, $0 \leq w \leq 1$, used to define the relative importance of $h_{Spectral}$ and h_{Shape}. This merging of image objects stops when f exceeds a predefined threshold called the scale parameter, S (Ursula C. Benz, 2003) – the maximum allowed change in heterogeneity that may occur when merging objects (Darwish et al., 2003). A schematic representation of the image segmentation concept is given in figure2.6. Appropriate values for S, and weights for $h_{Spectral}$ and h_{Shape} are selected by an interactive process until parameters are obtained that best delineate the image objects according to the view of a geologist.

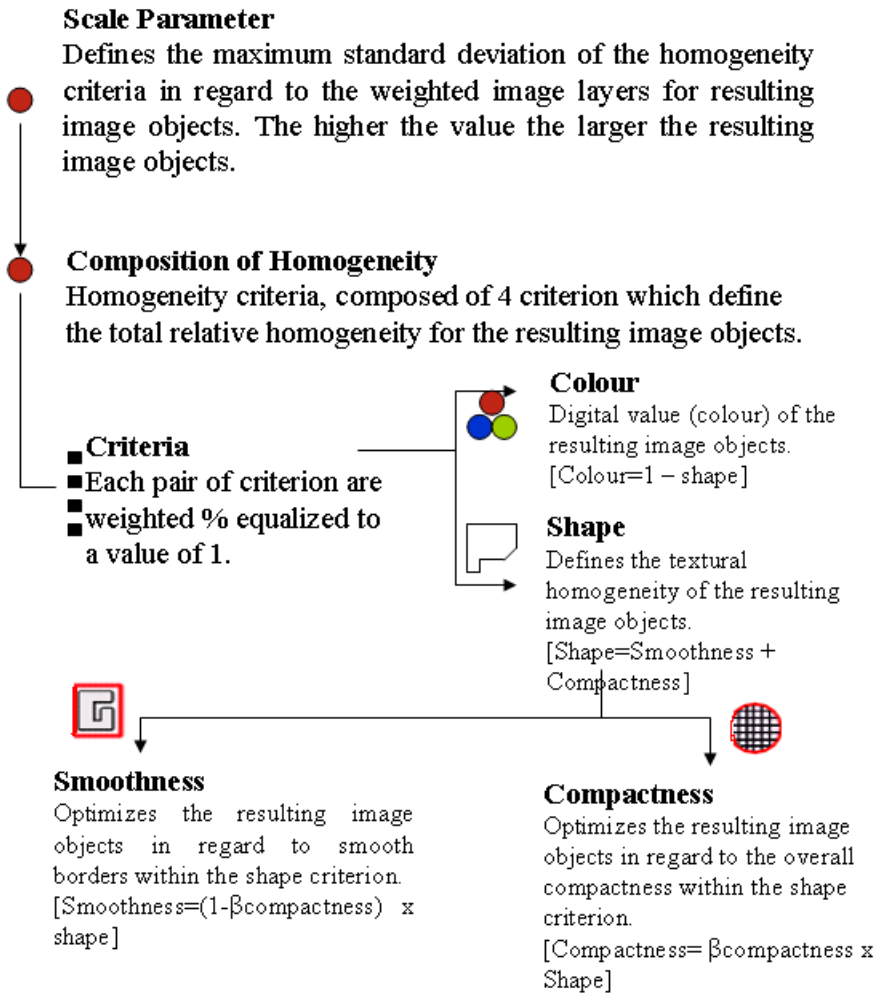

***Figure 2.6**: Image segmentation concept flow diagram*

2.3.2 Knowledge-Based Design

The object-based image analysis incorporates both the power of computers and human knowledge to classify an image. A knowledge-based scheme involving human interaction is used to define possible classes present in the image, to train a suitable classifier by selecting representative objects for each

class, and to define features that could distinguish objects that belong to different classes. Later this trained classifier is used for automated classification of other similar images. The main steps in the knowledge-base design are detailed below

(a) Defining Class Hierarchy

A priori counting and naming of the classes is done based on examining core, core data, core photographs, image log characteristics, and other geophysical logs. Based on this knowledge, a class hierarchy, which contains all classes in the desired classification scheme, is developed.

(b) Feature Extraction

Features are calculated for each image object, for example, mean of spectral values of all pixels forming each object, their standard deviation, and maxima of the spectral value of each image object, or Haralick textural features (defined earlier in this chapter). These features are not calculated for each window compromising the spatial property or for pixel pairs resulting in unrealistic results, rather are done on image-objects which are formed by grouping identical neighboring pixels together, which incorporates their original spatial characteristics. Image objects sharing similar feature ranges are then classified into respective classes using fuzzy classifiers.

(c) Selection and Training of Classifier

The classification of the image objects is performed by supervised classification, based on fuzzy logic (Benz et al., 2003). Fuzzy logic is a multi-valued logic quantifying uncertain statements. The basic idea is to replace the two Boolean logical statements “true” and “false” by the continuous range of

[0,…,1], where 0 means “false” and 1 means “true” and all values between 0 and 1 represent a transition between true and false. Avoiding arbitrary sharp thresholds, fuzzy logic is able to approximate the real world in its complexity much better than the simplifying Boolean systems do. Fuzzy logic can model imprecise human thinking and can represent linguistic rules. Hence, fuzzy logic appear to be ideal for interpreting lithofacies as training data are based on interpretation by a geologist

Fuzzy classification is beside neural networks (Gopal and Woodcock, 1996) and probabilistic approaches (Curlander and Kober, 1992) and is a very powerful (Benz et al., 2003) and an expert system for classification (Tsatsulis, 1993). Fuzzy classification consists of an n-dimensional tuple of membership degrees, which describes the degree of class assignment μ of the considered object *obj* to the *n* considered classes.

$$f_{class,obj} = [\mu_{class\_1}(obj), \mu_{class\_2}(obj), \ldots \mu_{class\_n}(obj)] \qquad (2.10)$$

Instead of information about which membership degree is the highest, this fuzzy classification scheme contains all information about the overall reliability, stability and class mixture.

Hence in this classification, all objects in the image are given a value between 0 and 1, which represents the likelihood of their being a member of the different classes in the class hierarchy. The classification is done either by using nearest neighbor classifiers or by membership functions, or both. Both Nearest Neighbour and Membership Function act as class descriptors. The Nearest Neighbour classifier describes the classes based on typical representative samples selected for each class which defines the feature range of each feature that are used to classify the image. A feature space, a cross

plot, is constructed based on the calculated features that could distinguish the classes defined in the class hierarchy. The basic assumption for image classification is that a specific part of the feature space corresponds to a specific class. If more than two features are required to distinguish objects that belong to various classes effectively, then a multidimensional feature space is created.

A Membership Function classifier on the other hand, describes classes based on predefined rules to formulate knowledge about the image content. For example, rules may be based on the spectral intensity of pixels grouped together as objects. In such a case, a spectral intensity histogram profile of the image objects can be created. Then, an appropriate threshold is defined, above which it is one class and below is another class. In case of more than two classes, several spectral intensity thresholds can be defined to classify image objects into appropriate classes; an example is shown in figure 2.7.

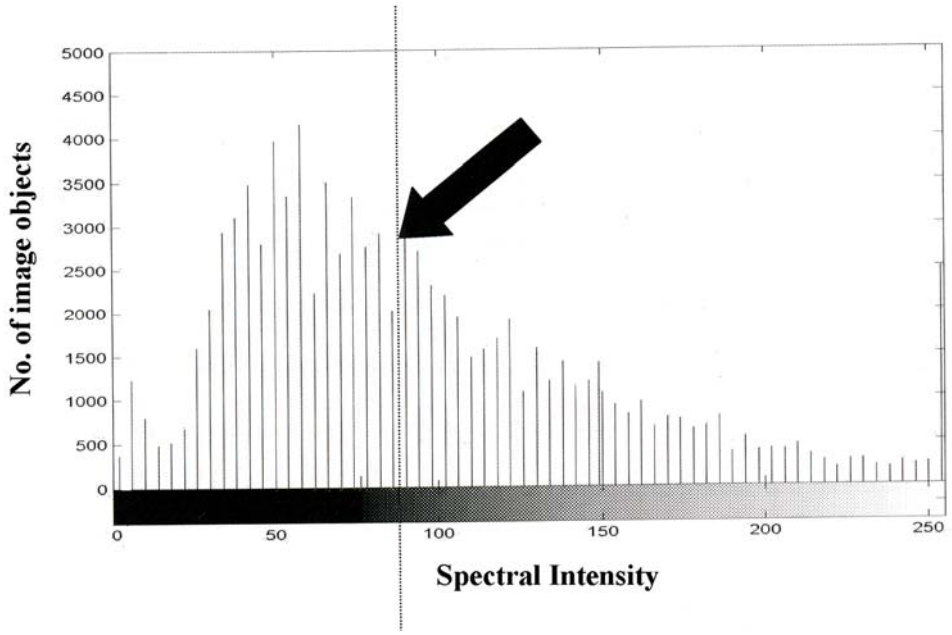

Figure 2.7*: An example of threshold defined on a spectral intensity histogram of the image-objects. This defined threshold could distinguish image-objects into two*

classes, objects with spectral intensity above 85 to one class and below to another class

Selection of classifier is dependant on number of features of the image-objects that need to be used for a successful image classification. In some cases, the classes to be identified (eg: sand shale sequence) from image logs could be easily done based on a single feature such as spectral property (Hurley and Zhang, 2009a). However, in most other cases we may need to use one or more textural features (Hua et al., 2009) along with or without spectral properties for image classification. If a class can be separated from other classes by one or very few features the application of Membership Function is recommended, otherwise the Nearest Neighbour approach is preferred which can operate on a multidimensional feature space. The fuzzy approach of Nearest Neighbour translates feature values of arbitrary range into fuzzy values between 0 and 1, indicating the degree of membership to a specific class. By translating features into fuzzy values, fuzzy classification standardizes the features and allows the combination of features, even if they are of very different range and dimension. A combination of both the classifiers could also be used in case of complicated class hierarchy as discussed in chapter 7.

2.3.3 Image Classification

Classification is a process of assigning each segmented object into appropriate classes (for example, to different lithologies in this study on image logs). The principle of image classification is that each object is assigned to a class based on its characteristic features, by comparing it to the predefined feature ranges in the feature space. Doing so for all image objects results in the image classification. The feature ranges for each class are predefined by assigning a representative set of sample objects to each class. Hence, when an unknown sample is given, the classification algorithm searches for the closest sample

object and the classifier assigns it to the appropriate class based on the classifier training. Figure 2.8 shows an example. The figure shows samples of two classes, class *red* and class *blue*. When an unknown image object, *A,* is given, it will be assigned to class *blue* as its closest sample object *B* belongs to class *blue*. The distance measure that defines what is meant by 'close' is,

$$d = \sqrt{\sum_f \left(\frac{v_f^{(s)} - v_f^{(o)}}{\sigma_f} \right)^2} \tag{2.11}$$

where *d* is the distance between sample object *s* and image object *o,* $v_f^{(s)}$ is the feature value of the sample object for feature *f,* $v_f^{(o)}$ is the feature value of the image object for feature *f, and* σ_f is the standard deviation of the feature values for feature *f* within that class. The distance between a sample object and the image object to be classified is thus normalized by the standard deviation of all feature values within that class. Hence, a distance value $d = 1$ means that the average distance equals the standard deviation of all features defining a particular class.

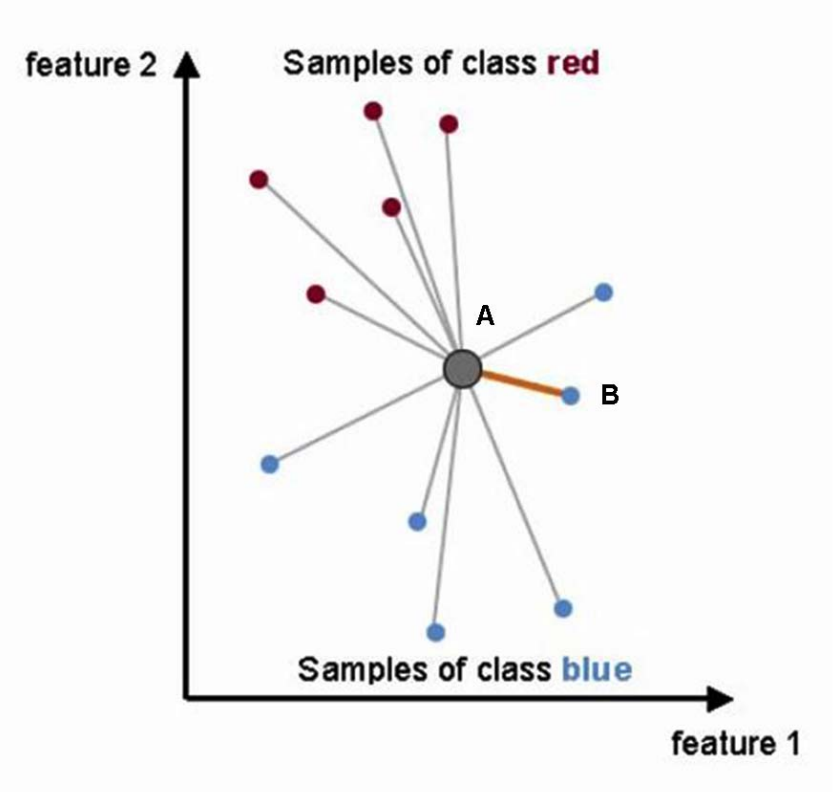

***Figure 2.8**: Principle of Nearest Neighbor classification (redrawn from eCognition user manual)*

2.3.4 Protocol Development

Protocols in human verbal communication are separate rules about appearance, speaking, listening and understanding. They work together to help people successfully communicate. Similarly, a protocol in object-based image analysis is a set of rules and controlling parameters, arranged in a sequential order and working together to automate image classification. A well trained classifier can be used on image logs from the same geological setting with minimum effort. Hence, all parameters that best classify the image, defined based on the experiments, are coded as a protocol. This developed protocol can be adapted to images from other geological areas with appropriate

modifications to suit each area. A schematic diagram of the various steps recorded in the protocol for automated lithology extraction from an image is shown in figure 2.9.

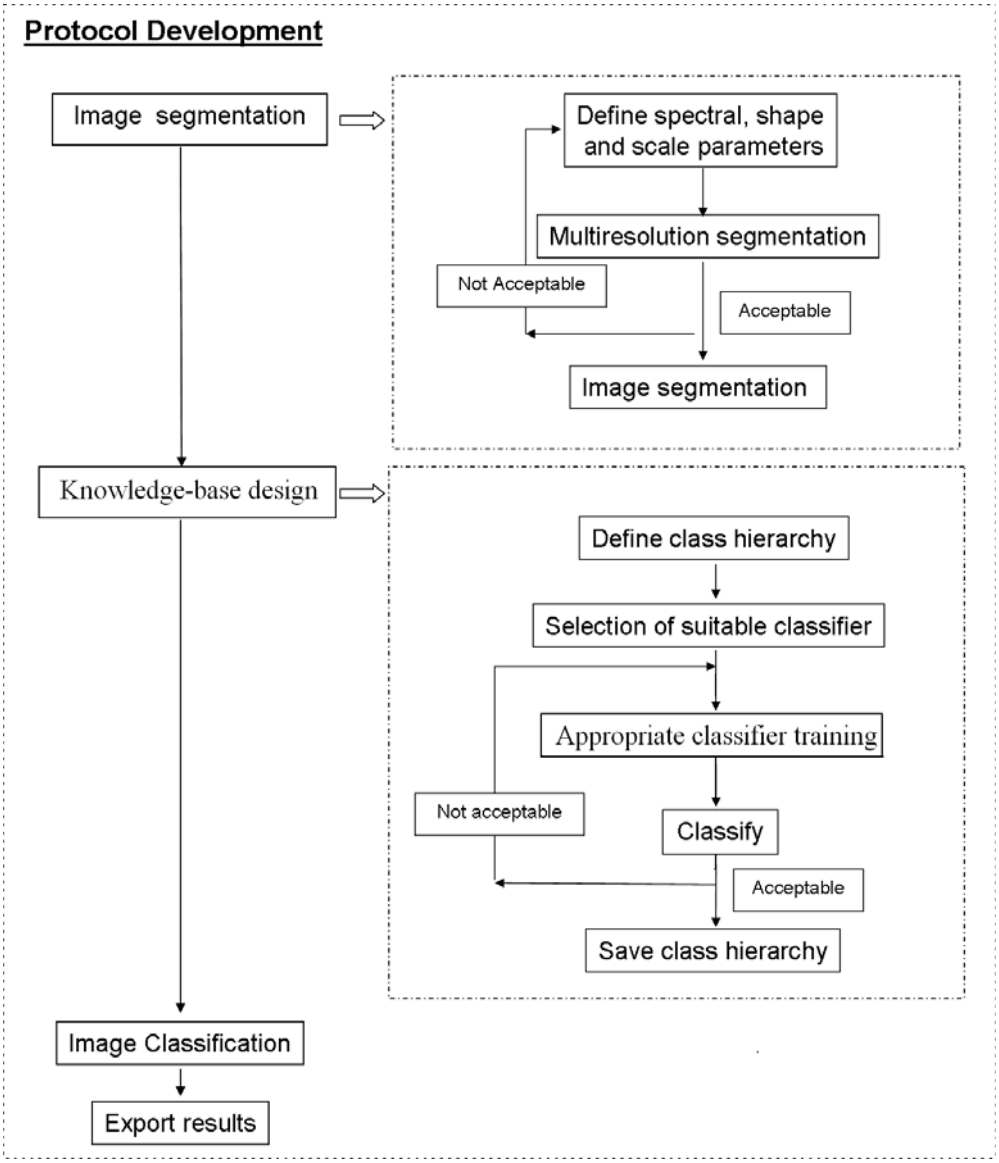

Figure 2.9*: Schematic representation of various steps recorded in the protocol for automated lithology extraction from core photograph is shown in the left hand side*

and the experiments involved in finalizing each of these steps is shown in to the right hand side of the figure

In this study, object-based image analysis software called 'eCognition' (Benz et al., 2004; Userguide_eCognition, 2003) is used to develop a routine method for automated geological images' classification.

2.4 ACCURACY ASSESSMENT OF THE CLASSIFICATION

An accuracy assessment of the automated classification is done by comparing it to the ground truth which, in this study, is the independent geologist's interpretation entirely based on core photographs. This is done by comparing both the results at each depth point or in a moving window of any pre-defined size. An overall accuracy is expressed as the percentage of the total number of correctly classified data from automated classification *(A)* to the total number of reference data which is the geologist's interpretation *(B)*. The overall accuracy *(O)* is given by

$$O = \frac{\sum A}{\sum B} * 100 \qquad (2.12)$$

2.5 CONCLUSIONS

Two methodologies have been introduced for the automated classification of lithofacies from image logs. The first method involves extracting textural features from image log at pixel level and then using them along with conventional geophysical logs to train a neural network. The second method involves grouping similar neighboring pixels to form image-objects. Then the spectral, spatial and textural features of the image-objects are related to various lithofacies. The information is used in a fuzzy set classifier for the lithofacies classification. The application of the first method is presented in

chapter 3 and the application of second method on core photos, outcrop photos and image logs from two different fields is presented in chapters 4, 5, 6 and 7 respectively.

Chapter 3

AUTOMATED LITHOFACIES IDENTIFICATION FROM IMAGE LOGS – A NEURAL NETWORK APPROACH

Summary: Automated lithofacies identification from image logs along with conventional geophysical logs using a neural network approach is presented in this chapter. Image log is analyzed in detail at pixel level and quantitative textural information is extracted. These features along with interpolated standard logs are related to ground truth (geologist interpretation based on core photograph) and is used to train a back propagation feed forward neural network. An introduction of the data set used in this study is given in section 3.2 followed by the application of the methodology in section 3.3. Section 3.4 shows the result of the method leading to the discussion and conclusions at sections 3.5 and 3.6 respectively.

3.1 INTRODUCTION

The image log provides a detailed description of the borehole wall in terms of its resistivity response. The resistivity response is being mapped in colour or grey scale images. Hence, the classification of these image logs is usually based on visual descriptors like colour intensities and/or texture. A good review of various texture analysis methods was given by Haralick (1979), Van Gool et. et al., (1985) and Reed, Hans du Buf (1993), Zhang and Tan (2002), and Xie (2008). Among all, the gray-level co-occurrence matrix method (Haralick et al., 1973) is very effective for texture analysis (Hua et al., 2009; Zhang, 2005). Hence, similar to the works by Harris et al., (1993), Hall et al., (1996), and Linek et al., (2007); the textural features from image logs are quantified using this method.

Usually, the shape of the log curves is extensively used by the geologist to draw correlation lines to identify rock types (Rabiller and Schulbaum, 2001). Similarly, the curve signatures of image-derived textural features are related to the core-derived lithofacies. The works by Hall et al., (1996), and Linek et al., (2007) rely only on the textural information extracted from the image logs for lithofacies classification. In this study the conventional geophysical logs are integrated with the image-derived textural features (the importance of using standard logs along with image log is discussed in chapter 1) for lithofacies classification. The standard logs were interpolated to match the image log depth intervals so as to retain the high resolution information of the borehole surveyed by the imaging tool.

Hall, et. al., (1996) used Self-Organising Map (Kohonen, 1984), which is an unsupervised classification method, to group similar textural features into various rock classes and hence, excluded the expertise of a geologist. Linek et al., (2007) used discriminant function analysis (Doveton, 1994), which is a supervised classification method and hence, incorporated local geological knowledge and expertise of a geologist for assigning characteristic texture features to different rock classes. However, when using discriminant function analysis, it is common to model the distribution of the populations with a normal distribution (Doveton, 1994). Though the real distribution can be incorporated, it is often computationally intensive and many programs lack universal capabilities. Also, in this methodology, the log signatures of particular facies must enable it to be distinguished from other defined facies and that no other facies are expected to be encountered. Therefore, this technique is very specific which can only be used for a particular field or sedimentary environment. The dimension reductions technique used in this

method could result in parameters that appear far removed from the original input data, making the outcome sometimes ambiguous to interpret.

According to Mitchell (1997) neural networks offer a powerful classification method for learning relationships between attributes when presented with examples. Masters (1993) states that 'neural networks are most likely to be superior to other methods when the data on which conclusions are based is 'fuzzy', for instance the input data are 'human opinions''. They claim to be robust in the presence of noisy data, have the ability to generalise, and can handle data that exists in many dimension (e.g. many logs). Therefore, neural networks offer an alternative to the above methods and appear to be a good choice for interpreting lithofacies where training data are based on interpretation by a geologist (Martin, 2004).

Hence, a set of log responses of the quantified textural properties from image logs and the interpolated standard logs are assigned to corresponding core-derived lithofacies information. This is used to train a supervised feed forward back propagation Neural Network. This trained classifier is then verified by testing on the same data interval which was used for the Neural Network training. The verified classifier, in principle, is applicable for automated lithofacies identification from borehole at depth intervals outside the training interval and also on data from similar geological settings.

3.2 STUDY AREA - THE OSEBERG SOUTH FIELD

3.2.1 Introduction

The data used in this study is from Oseberg South area, the Northern North Sea. Oseberg is an offshore oil field with a gas cap in the North Sea and is located 140 km northwest of the city of Bergen on the south west coast of

Norway (Erlandsen, 2000). The field is 25 km long by 7 km wide (Sognesand, 1997), and was discovered in 1979. The operator is Statoil, in partnership with Petoro, Total, ExxonMobil and ConocoPhillips (Norwegian_Petroleum_ Directorate). The development of this field is known to be one of the significant milestones in emergence of Norway's independent oil and gas industry (Fagerberg et al., 2009; Norwegian_Petroleum_Directorate).

The image log data is from well 14 of the block 30/9 (Well 30/9-14). It is located in the western part of the block, on the Southern Oseberg complex as shown in figure 3.1.

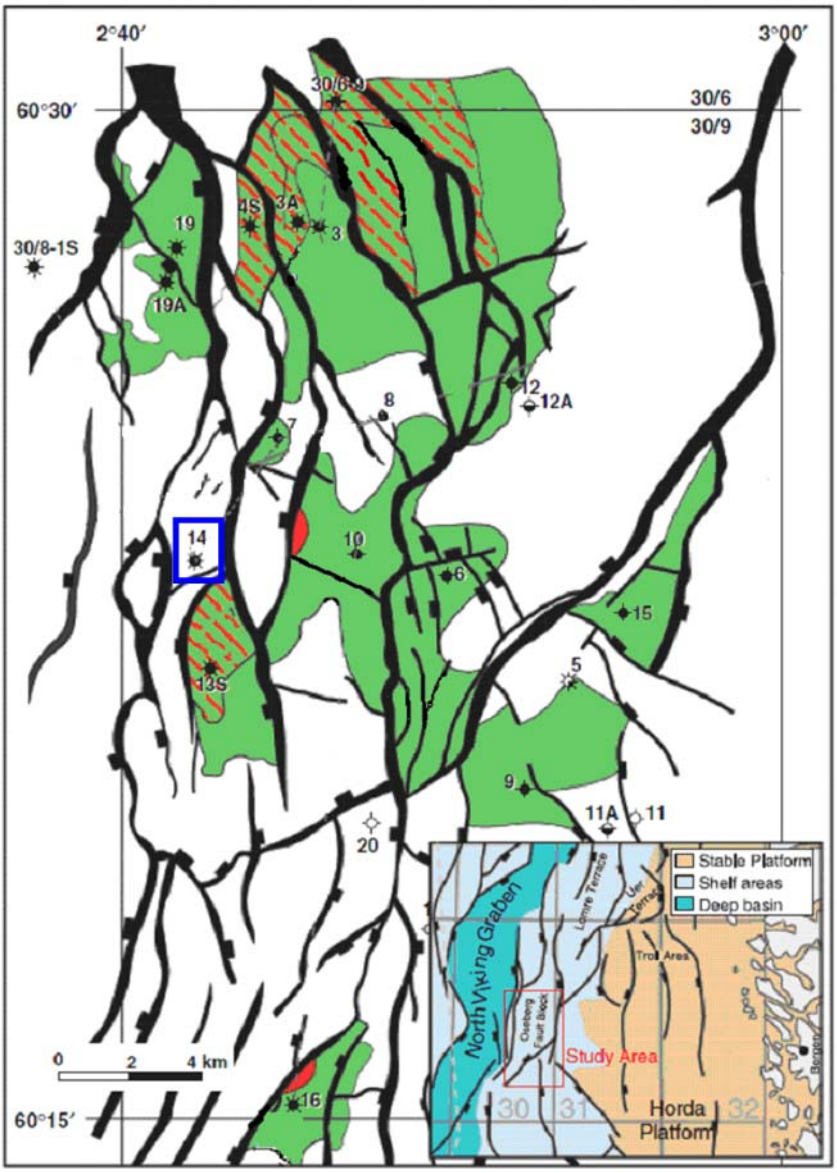

Figure 3. 1 *: Map of the study area showing key wells (Redrawn from Loseth et al.,(2009)). The data used in this study is from well 14. (Figure shows that the region is heavily faulted and most of the faults (in the enlarged region shown in the figure) strike N-S and NNW-SSE, A detailed explanation of the regional geology can be found in Loseth et.al, here, the figure is used to show the location of well 14 in the Horda platform)*

3.2.2 Geological Setting and Stratigraphy

The Oseberg field consists of a series of hydrocarbon accumulations within the Viking Graben. The field consists of several sandstone reservoirs in the Middle Jurassic Brent group. The stratigraphy of the Brent group is discussed in various literatures (Graue et al., 1987; Johannessen and Nottvedt, 2008). Previous studies of the Brent Group emphasize the wave and storm dominated nature of the shoreline (Cannon et al., 1992; Helland-Hansen et al., 1992) resulting in a wave generated hummocky and swaley types of cross-stratification (Scott, 1992). A schematic representation of the facies relationships in the Brent delta is given in figure 3.2. The cored depth interval used in the study is from the Tarbert Formation, Middle Jurassic. This is a shallow marine sand interval containing parallel, hummocky, cross bedded and bioturbated sand.

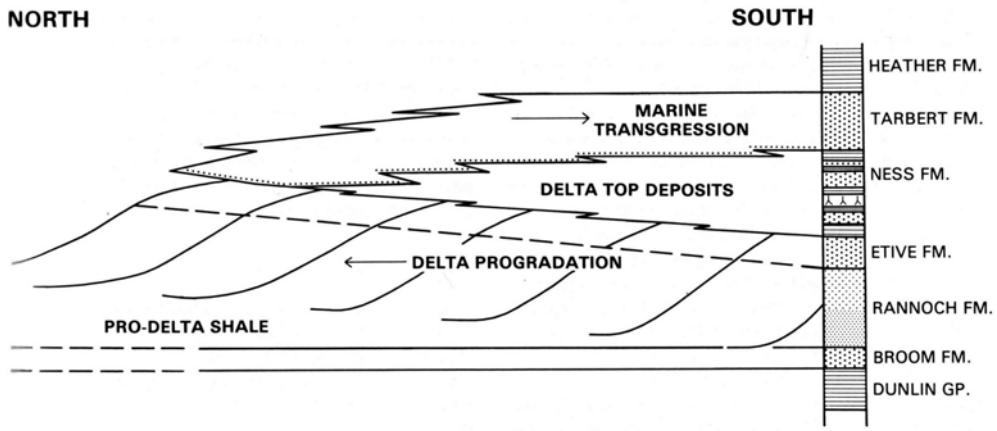

Figure 3. 2*: Facies relationships in the Brent Delta. The data from the cored depth interval in the Tarbert Formation, Middle Jurassic is used in this study (taken from Brown (1984)).*

3.3 METHODOLOGY

3.3.1 Image log processing

Three processing steps are involved prior to the texture analysis of image logs, they are, image pre-processing, depth matching and image splicing

3.3.1.1 Image pre-processing: The image log is pre-processed to enhance the image quality and to account for any possible mis-calibration or malfunctioning of the imaging tool. The image processing carried out on the image log used in this study are button equalization, pad/flap normalization and accelerometer correction. A brief explanation of each of the processing steps is given below.

a. ***Pad/flap correlation:*** A correction based on comparison of the data at the edge of any pad or flap. In theory, the data at the edge of a pad should record approximately the same value as the attached flap as they are adjacent to each other. The pad/flap correction correlates all four pad/flap boundaries and weights any offsets accordingly so that adjacent data has approximately similar values. The difference in the image log before and after the application of pad/flap correction is shown in figure 3.3 (a)
b. ***Button equalisation:*** When recording data, button responses can vary considerably due to uneven pad contact or mud smear across particular buttons. This processing step attempts to remove this variable response by computing the data distribution of each button over a specific moving window, as well as the distribution of all button data over the entire window. A transform is then applied so that the data distribution of each button is similar to the overall distribution, preserving the textural elements within the image. Figure 3.3 (b) shows image log before and after button equalisation.

c. ***Accelerometer correction:*** The buttons on pads and flaps are at different depth levels and hence they measure resistivity at same depth at different times. If the tool travels at a constant velocity, the time for the next row of button to reach a particular depth at which the measurement was taken by the first row of buttons would be known. However the actual velocity of the tool does not always equate to the velocity of the cable at the surface since the tool cable can stretch especially when the tool gets stuck (Logs are generally recorded as a function of cable depth). Correction can be done using the recorded acceleration of the tool via an accelerometer that is located in the tool itself. Image log before and after to the application of accelerometer correction is shown figure 3.3 (c).

Other corrections that may be required are Emex correction and Compensation for dead buttons, which are also explained below.

d. ***Emex (Emmiteur d'exitation) correction:*** The frequency of the signal from the tool may be varied during measurement by the tool operator since this can help the high frequency return of the FMI pad resistivity, improving resolution over very high or very low resistivity zones (Martin, 2004). For this reason the actual readings may not be comparable from one zone to another. This is also one of the reasons why this type of resistivity measurement cannot be used to calculate a shallow water saturation curve. Using the Emex curve that indicates the applied voltage against depth, the image log can be compensated.

e. ***Compensation for dead buttons:*** Individual buttons that record the data and make up the image sometimes fail, due to the tool electronics. This failure can be permanent or intermittent. In order to account for this, button values that fall below a specified threshold (in many cases they will represent ‘null’ values) are replaced by values that are linearly interpolated from adjacent button values at either end of the dead button section on the same pad or flap. If a whole row of dead buttons exists then interpolation is taken from the next line of buttons. A limitation occurs if a

whole area of dead buttons exists. In general, because of the high quality of the data this step may not appear to make significant differences to the images.

The data processing has been done using the petrophysical software – TerraStation. Further information on the processing steps can be found in the TerraStation manual (TerraSciences 2002).

3.3.1.2 Depth Matching: The processed image log is correlated with core and standard logs and a detailed image-log-core depth matching is performed. This can be done either qualitatively by an interpreter, or can be done quantitatively, and probabilistically using semi-automated methods (Price et al., 2008). In this study, a qualitative depth matching is performed using the petrophysical software –TerraStation.

3.3.1.3 Image Splicing: Most electrical borehole-imaging tools are pad type devices with fixed arrays of electrodes, which commonly have gaps of missing information between the pads (as shown in chapter 1, figure 1.1). The non-imaged parts of the borehole appear as blank (white) strips between the pads (see image log in figure 3.4). There are methods to fill these gaps as suggested by Hurley and Zhang (2009b) using realistic statistical models. In this study we have processed the image log to filter these blank strips and the data has been spliced. Figure 3.4 shows the spliced image log derived from a dynamic normalized image log.

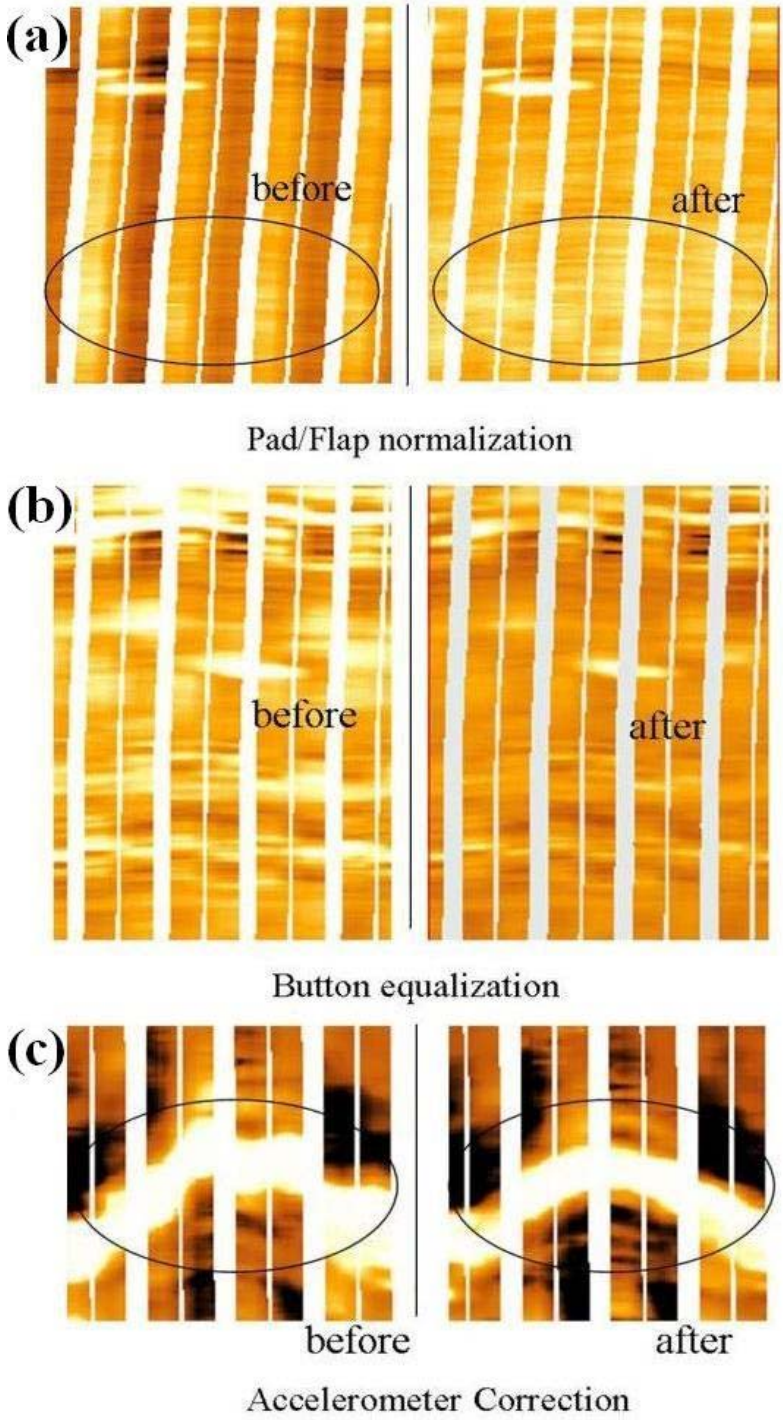

Figure 3. 3*: Image log before and after (a) Pad/flap correlation, (b) Button equalisation, and (c) Accelerometer correction*

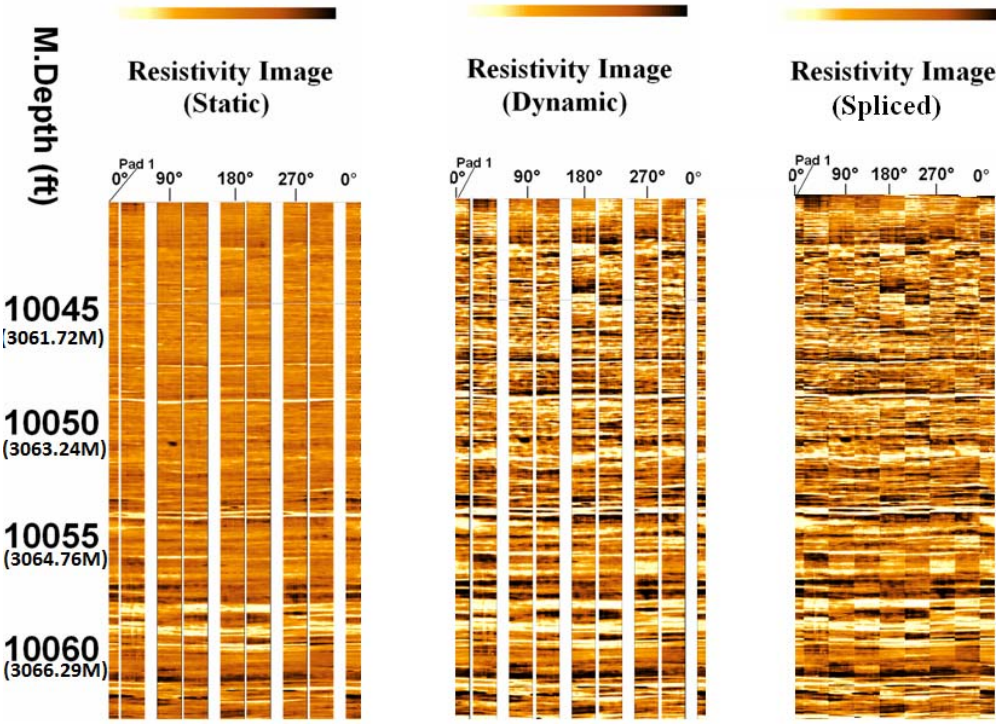

Figure 3. 4*: From left to right, column 1, depth; column 2 static normalize image; Column 3, dynamic normalized image; column 4, spliced image from dynamic normalized image log.. Note the white strips in the static and dynamic normalized Image logs, representing the non-imaged parts of the borehole which is removed in the spliced image.*

3.3.2 Textural feature extraction

The texture of a rock is an important geological characteristic as it reflects the depositional mechanisms and fluid flow, which control the reservoir architecture and recovery factor respectively (Ye et al., 1998). Image logs and core are good sources of data to study the texture of rocks in the reservoir. In image logs, texture can be defined as a function of the spatial variation in grey level intensities (Tuceryan and Jain, 1998) which indirectly reflects the spatial relationship of geological objects observed in the borehole (Ye et al., 1998), as explained in chapter 1.

In this study a pattern recognition technique (Duda et al., 2001) was applied to image logs to extract quantitative textural information. A grey scale image log is used where the current intensities measured by each electrode are translated into a variable intensity of grey-level images and each grey level corresponds to a distinct current intensity for the entire image. A sliding window is designed to take all resistivity values around the borehole wall for 5 consecutive pixel depth points at a time from the grey coded electrical borehole wall image. For each window, the occurrence of pixel pairs are calculated in four directions, (horizontal, vertical and two diagonal) and tabulated to form the grey level co-occurrence matrix (GLCM) as explained in chapter 2.

A second order statistical analysis is then applied on each of these computed grey level co-occurrence matrices and the so-called Haralick features (Haralick et al., 1973) such as contrast, entropy, dissimilarity, homogeneity and correlation are calculated. The calculated Haralick features are then assigned to the central pixel of the window and depth related to the original image. The window is then shifted one depth point down and the process is repeated to get a GLCM for the new window. Haralick features are then extracted from the new GLCM and the features values are depth related. This process is continued until the whole image is covered. Figure 3.5 shows an example of textural features derived from the image log in the vertical direction, along with the image log used for this purpose.

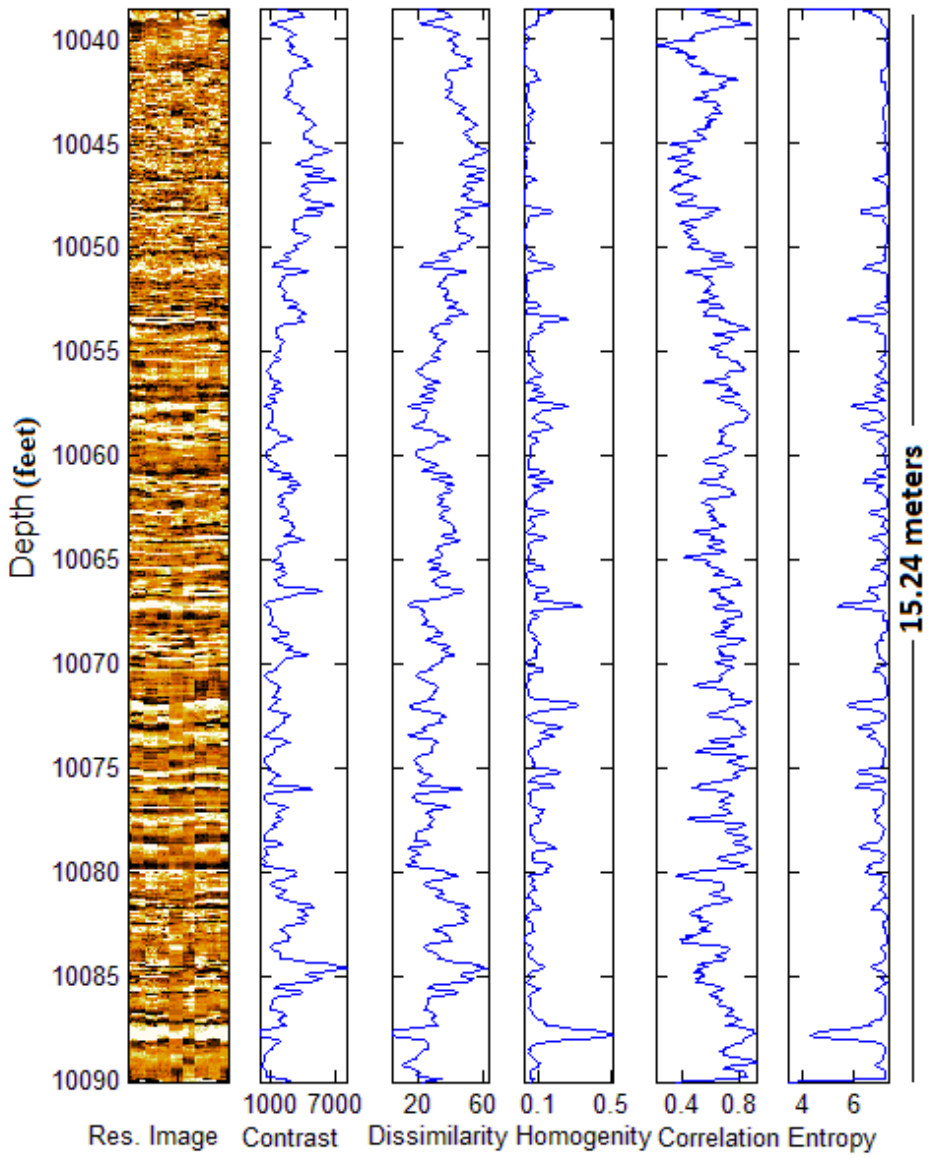

Figure 3.5*: Haralick textural features, contrast, dissimilarity, homogeneity, correlation and entropy, calculated from the resistivity image (column two) in the vertical direction.*

3.3.3 Input Selection for Neural Network Training

Haralick features are calculated in the horizontal, vertical and two diagonal directions (0^o, 90^o, 45^o, and 135^o). The features are then averaged for each depth point to make them rotation invariant (Linek et al, (2007) and were used to train the neural network for the lithofacies identification. The Haralick features in four directions and their average are shown in figure 3.6.

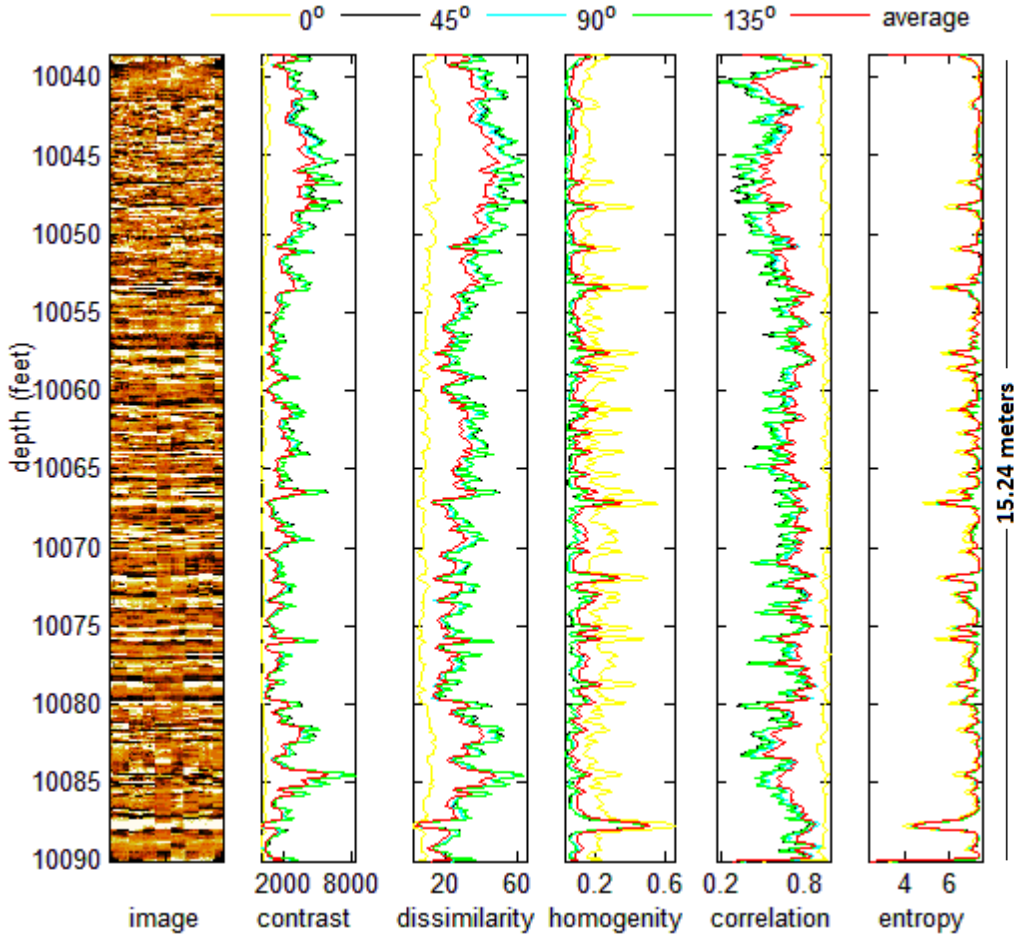

Figure 3.6: *The Haralick features calculated from the image log in all four directions and their average at each depth point*

Geologists compare image log properties with standard log signatures when they interpret the image log qualitatively. In doing so, both data sets

complement each other for a successful evaluation of lithofacies present in the subsurface. Similarly, unlike the study by Linek et al (2007), who used only image log derived textural features for rock classification, both image derived textural features and standard logs are used in this study for lithofacies classification. To account for the difference in resolution of the two data types, the standard logs are linearly interpolated in such a way that the data exist at the same increments as the image log.

Selection of inputs is important in any data driven techniques, such as artificial neural networks and fuzzy systems, because the final result is heavily dependent on the input variables. Though we could extract any number of quantitative features from image logs, all of them will not lead into a geologically meaningful classification. Hence, selection of extracted quantitative features needs to be done very carefully so that it can replicate the ground truth. For example if the image log under consideration is mainly a sand shale sequence, it represents a geology that could be resolved based on features related to spectral properties (resistive and conductive beds; enclosed fluid is not taken into consideration in this case). Similarly, distinguishing lithofacies within a particular lithology is possible based on textural properties; for example the two sand types, parallel laminated sandstones and conglomerates, have different textural properties in the image since the parallel laminated sandstone is relatively homogeneous compared to the conglomerate. Hence, a thorough study of geology and features which can be used to distinguish them from an image log needs to be investigated.

In this study, a comparison between textural features extracted from image logs and its relation to the lithofacies classes present in the study area were done qualitatively. Then, a careful selection of textural features that could

distinguish the lithofacies were done before using them in the classification scheme. Number of features used in classification was initially reduced giving good generalization within the inputs. For example, the two features, homogeneity and entropy classify the same textural features within the data, one measures the homogeneity while the other measures the randomness or in other words heterogeneity in the image. From figure 3.5, it can be seen that both curves – homogeneity and entropy are mirror images at every depth intervals. Similarly, contrast and dissimilarity are similar at every depth. All such features that could be correlated with another feature and hence, bear no further information were removed. Hence from contrast and dissimilarity, only dissimilarity is used and from homogeneity and entropy, homogeneity is used.

Other factors to be considered while choosing input variables are features those are unable to discriminate between different rock classes. These features are redundant and useless and may reduce the accuracy and stability of the classification process (Duda et al 2001). Therefore, we first identify the texture features those discriminate the lithofacies from image logs best. The correct choice of model inputs is also important for improving computational efficiency of the classification techniques (Linek et al., (2007).

Masters (1993) put forward two conditions for the data to be a useful discriminator. They are, 1) the variance of inputs should be approximately the same, and 2) the data distribution should be approximately symmetrical. Hence, a linear normalization has been applied to all input variables and scaled them between 0 and 1 which brings all the inputs into the same range equaling the importance of all variables before learning takes place in neural network.

3.3.4 Neural Network Training

The ground truth obtained by the geologist based on the core photograph shows that the sandy interval chosen for the study is dominated by three types of lithofacies – bioturbation, horizontal stratification, and cross bedding and hummocky types of cross stratification (as no differences could be seen on image logs between cross bedding and hummocky cross stratification, it is very difficult to tell them apart from this data alone. Hence, these two classes were grouped together in this study as cross stratification). The potential inputs were correlated with these lithofacies based on ground truth from the core photograph. An example of the image log and their corresponding core photographs showing these three types of lithofacies is shown in figure 3.7.

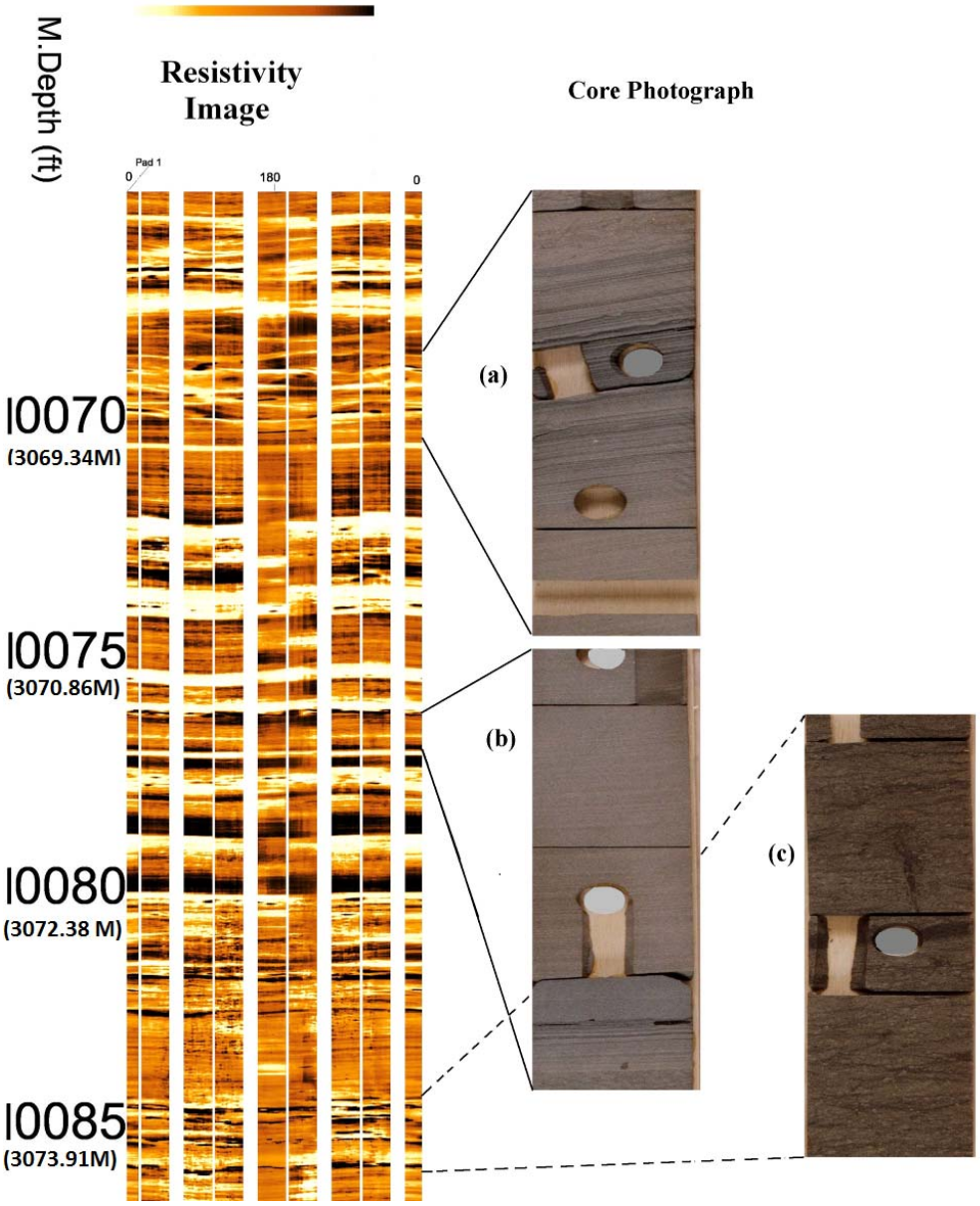

Figure 3.7*: Image log and their corresponding core photographs showing (a) cross stratification, (b) horizontal stratification, and (c) bioturbation*

A continuous 2026 sampling points were chosen for the neural network study. Out of these 582 sampling points were used to train the neural network for an

automated lithofacies classification. Neural network is sensitive to the abundance of training data (Masters, 1993). That is, neural network models may find it difficult to discriminate lithofacies that make up minor sections of the training data. Hence, these 582 sampling points were taken interactively giving equal importance to all three lithofacies (that is 194 each).

The trained neural network is tested on the same data set that was used to train the neural network. The testing result showed that 194 out of the 194 sampling points belonging to the bioturbated zone were correctly identified. 133 sampling points belonging to the cross stratification were correctly identified while the remaining 61 sampling points were classified as horizontal stratification. Thus out of the total 582 sampling points 521 points were classified correctly yielding an accuracy of 89.52 %.

3.4 RESULTS

The trained neural network is applied on the entire depth interval for an automated lithofacies classification. The interval contained 2026 sampling points, including the 582 sampling points used in training the neural network. The classification result obtained from the neural network along with a geologist's interpretation based entirely on core photograph is shown in figure 3.8.

A one-to-one comparison of the automated classification with the geologist's interpretation show similar results at 10041-10050 feet/3060.50-3063.24 meters (bioturbation), 10055-10058 feet/3064.76-3065.68 meters (cross stratification followed by horizontal stratification), 10059-10060 feet/3065.98-3066.28 meters (cross stratification), 10063-10065 feet/3067.20-3067.81 meters (bioturbation followed by cross stratification), 10067-10068.5

feet/3068.42-3068.88 meters, (horizontal stratification), 10072-10073 feet/3069.95-3070.25 meters (cross stratification followed by horizontal stratification), 10074-10076 feet/3070.56-3071.16 meters (horizontal stratification), 10077-10081 feet/ 3071.47-3072.69 meters (cross stratification followed by horizontal stratification), 10084-10084.5 feet/ 3073.60-3073.76 meters (bioturbation), and 10085-10086 feet/3073.91-3074.21 meters and 10088-10089 feet/3074.82-3075.13 meters (horizontal stratification). An accuracy assessment of the automated classification result is done by comparing it to the ground truth obtained independently by a geologist based entirely on core photographs.

Since the geologist interpretation is based on the core photographs, regions where core was absent or was taken for core analysis, and hence core photographs was not available for interpretation, were excluded in this study. Also, regions where core photograph was unclear and hence, geologist interpretation was not possible or interpretation which was not 100% confident were excluded from the result comparison. Thus, out of the total 2026 sampling points, 632 points were removed. Though these points were not considered in accuracy assessment, the classification result shown in figure 3.10 includes all these points. In the figure (column 4), regions where the geologist interpretation was uncertain are white and regions where core was absent are marked by an 'X'.

Out of the remaining 1394 sampling points, the geologist classified 501 as bioturbation, 435 as cross stratification and 458 as horizontal stratification. The automated method classified 423 samples as bioturbation out of which 409 were correctly classified (compared to the ground truth), 262 samples as cross stratification out of which 214 were correctly classified and 652 samples as horizontal stratification out of which 413 were correctly classified. 57

samples were unclassified and the assessment yielded an overall accuracy of 77.49%. The result is summarized in table 3.1 and 3.2.

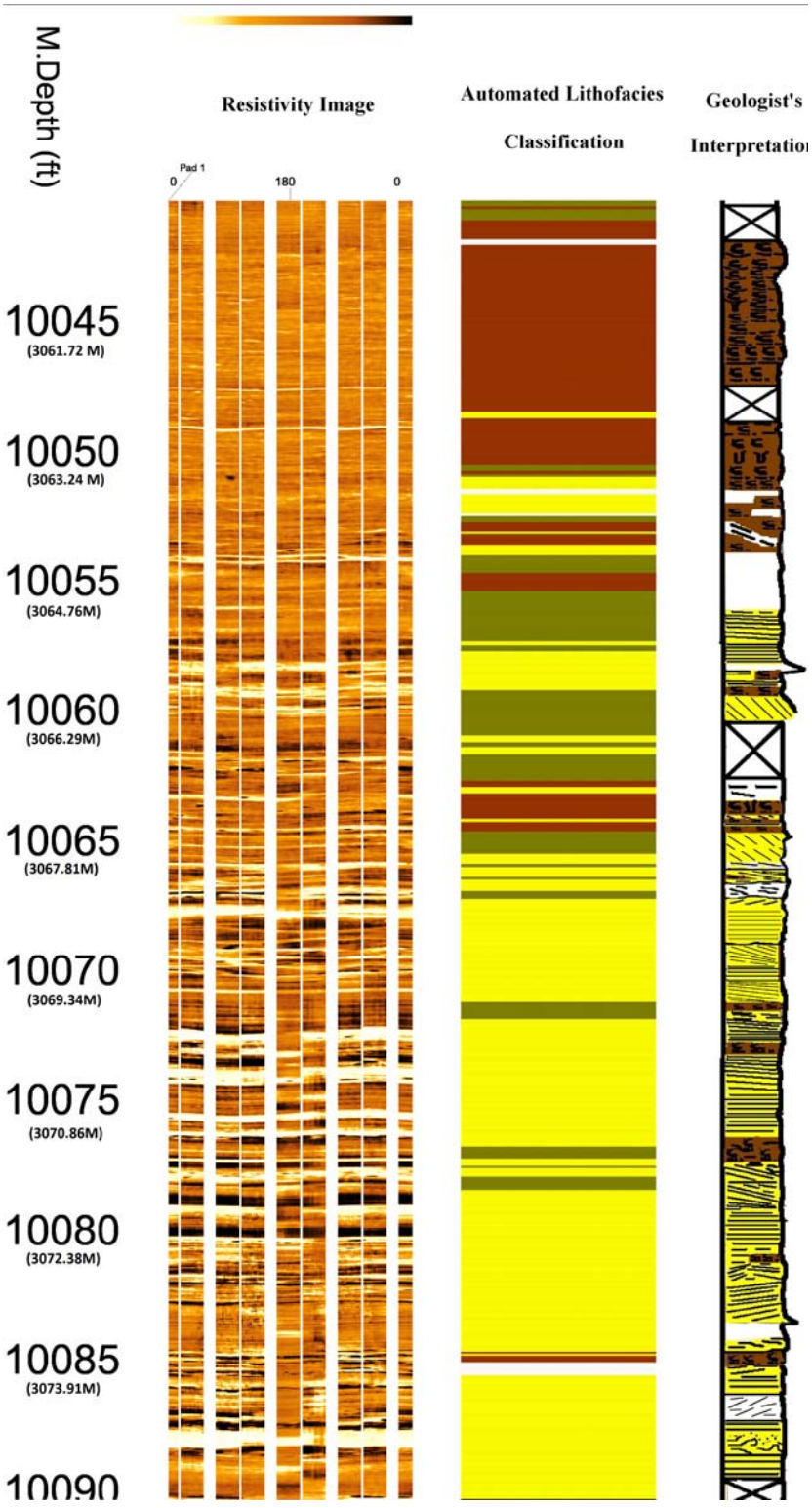

Figure 3.8*: Automated lithofacies classification from image log. From left to right:*

depth, image log used for the study, lithofacies predicted using neural network (brown-bioturbation, dark green-cross stratification, yellow-horizontal stratification, and white-uncertain regions), and geologist's interpretation based on core photograph (brown-bioturbation, yellow with straight line- horizontal stratification, and yellow with slanting lines-cross stratification. White regions with 'X' are intervals where core was absent and white regions are uncertain regions due to vague core photograph)

Automated Classification \ Geologist's Interpretation	Bioturbation	Cross bed	Planar Lamination	Unclassified
Bioturbation	409	11	3	-
Cross Bed	26	214	22	-
Planar Lamination	47	192	413	-
Unclassified	19	18	20	0

Table3.1*: Accuracy assessment of the automated lithofacies classification compared to the geologist's lithofacies interpretation at each sampling points.*

3.5 DISCUSSION

Image logs are considered to be an important source of information about the reservoir due to its borehole coverage and high resolution. The higher resolution compared to conventional logs may allow us to delineate thin beds in the reservoir. Therefore, this study did not make any attempts to remove the thin layers unlike Linek et al. (2006) who replaced the classes by the dominant class identified within a fixed depth interval or window. Though their approach could yield better accuracy by removing layers of very small thickness – represented by only one or a few depth points, it could also remove some valuable information about the geological heterogeneity.

Automated classification	Geologist's interpretation			
		Bioturbation	Cross Bed	Planar Lamination
	Total	501	435	458
	Correct	409	214	413
	Incorrect	92	221	45

Table3.2*: Accuracy assessment for each lithofacies; Comparison between automated classification and geologist's interpretation at each sampling points.*

A qualitative visual comparison of the automated image log classification to the geologist's interpretation from core photographs shows a reasonably good match even though the accuracy assessment result is only 77.49% accuracy. One of the major factors that affected the accuracy is the depth mismatch as seen in the automated lithofacies classification compared to the ground truth (figure 3.8). The depth mismatch in the interpretation may arise due to the reduction of two dimensional image logs into one dimensional textural feature logs. In textural feature extraction, a single value is calculated by averaging the spatial characteristics for a given depth and this single value may fail in drawing a horizontal bed boundary when used in neural network for lithofacies prediction. Another reason behind minor depth mismatch could be the averaged single feature value calculated from a sliding window as the textural property belongs to the window rather that a depth point.

When feature extraction is done at pixel level, it is highly possible that neighbouring pixels fall in the same class as the pixel under consideration, if they are not too distinct in their spectral intensity and this leads to miss classifications. The classification result in figure 3.8 shows that most of the cross stratifications and bioturbation predicted by the automated method are accurate compared to the ground truth. However, the method predicted some of the cross stratifications as horizontal stratifications. This is because; pixels belonging to both these classes do not differ much in their calculated texture values. Hence, these kinds of pattern or textural property which are irregular in shape will go unrecognized in this method as the spatial characteristics are averaged. The extracted averaged property over each depth may not be a true representative of the real geological heterogeneity.

This study utilized a simple neural network. Larger networks could possibly make better predictions as shown by Bhatt and Helle (2002) and Martin (2004) (theoretically both networks should produce the same result, but the division of the problem into smaller tasks allows the network to find the true relationships more easily). But the results will still be based on the texture and spectral properties in the image at pixel level. For a realistic lithofacies classification, it is really important to incorporate the spatial nature of the image properties. Therefore, this study did not concentrate on improving the accuracy of the classification result by trying various image enhancement methods or by approaching various advancements in neural network. Prime importance is given to a meaningful extraction of image property preserving its spatial nature and hence the following work is focused in this direction.

3.6 CONCLUSIONS

Automated lithofacies identification from image logs along with conventional geophysical logs using a neural network approach has been performed. Image log is analyzed in detail at pixel level and quantitative textural information is extracted. These features along with interpolated standard logs are related to a geologist's interpretation based on core photographs and this is used to train a back propagation feed forward neural network. The tested and verified network, in principle, is applicable for automated lithofacies identification in a borehole at depth intervals outside the training interval and also on data from similar geological settings. However, the study showed that image textural information at pixel level is not enough to extract the high density information encoded in image logs and hence a more efficient methodology is presented in the following chapters.

Chapter 4

AN INTRODUCTION TO OBJECT BASED IMAGE ANALYSIS: OUTCROP PHOTOGRAPH ANALYSIS

Summary: An Object-Based Image Analysis (OBIA) methodology is proposed in this chapter for an effective classification of outcrop photographs. This method works analogously to the interpretation of the same by human eyes. The chapter gives a brief introduction to the outcrop data used in this study in section 4.2, followed by an introduction to the advantages of object-based image analysis over pixel-based image analysis in section 4.3. A brief step by step application of the method is given in section 4.4, leading to the discussion of outcrop classification by the method in section 4.5. Details of the method are given in chapter 2.

4.1 INTRODUCTION

Outcrop study is one of the best ways to begin any geological interpretation as it provides visual records of relative changes in the geological strata. Outcrops allow direct observation of the bedrock *in situ*, and one can touch, smell or even taste different rock types in place. Outcrop photographs make some of the outcrop information portable and more accessible. An object-based image analysis methodology is proposed in this chapter for an automated outcrop classification from these photographs which could result in a fast, simplified interpretation method to compliment the qualitative outcrop photograph analysis methods.

4.2 DATA

Compared to core photographs and image logs, it is easier to ground truth the classified outcrop photographs as the outcrop itself can be visually examined. For this reason of least uncertainty in evaluation, the object-based image analysis is first applied on outcrop photographs.

The outcrop study has been carried out in Thorntonloch (Figure 4.1 (a)). Thorntonloch is a beach situated 5 miles east of the coastal fishing town of Dunbar, in southeast Scotland. The beach is skirted by long rocky outcrops, which are surrounded by deep channels and gullies. Some photographs of the field visit are given in figure 4.1. This region can be interpreted as a progradation of higher energy, unidirectional flowing sand body into finer-grained marine environment (possibly a small mouth bar system, or prograding crevasse system into an interdistributary bay). Digital photographs of the outcrops are collected in order to perform the object based image analysis and to automatically classify the outcrop photograph.


(a)


(b)

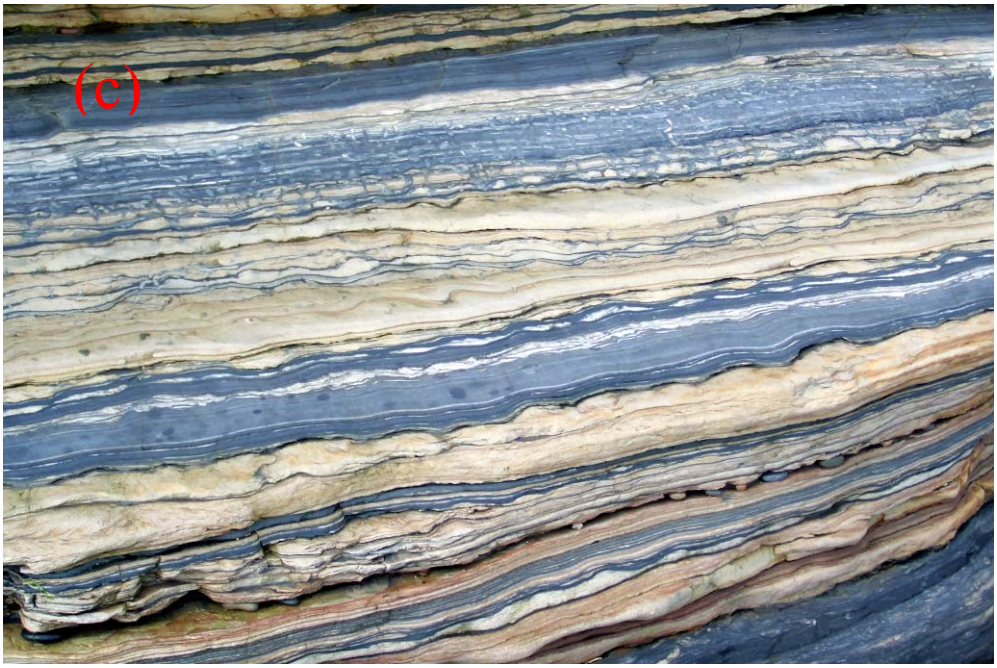

Figure 4. 1: *A few photographs from the field area: (a) A panoramic view of study area (Thorntonloch), (b) myself capturing the outcrop photos (the stratigraphy shows thickening and coarsening upward succession, with thin bedded mudstone or siltstone alterations with burrows and isolated ripple laminations at the bottom, (c) one of the photographs used in this study to evaluate the classification results against a geologist's qualitative visual interpretation.*

4.3 METHODOLOGY

A pixel-based image analysis has been discussed in the previous chapter (chapter 3) to extract textural properties from image logs. However, pixel-based analysis and the extraction of any number of 'single' image properties (for example, textural features in chapter 3) at a given depth do not fully utilize the information recorded in these datasets as it does not preserve the spatial information in the image. For example, in high resolution images it is extremely likely that neighboring pixels belong to the same class as the pixel under consideration which could result in misclassification especially when

the textural properties are spatially irregular and varying in shape (Blaschke and Strobl, 2001).

In the outcrop photograph shown in figure 4.2 (a), the dark colored regions belong to shale and the light colored regions belong to sand. Here, the qualitative visual interpretation of the photograph is carried out mainly based on its spectral variation. However, if we quantify this spectral property for each depth, it would result in an average spectral value which is not the true measure of the spectral feature at a particular depth since the beds are dipping. Usually, in image interpretation methods as discussed in chapter 3, an averaged image property is extracted for each depth, and the image classification is carried out based on the signatures of these extracted properties. For example, the mean of grey scale intensity of the outcrop photograph as a function of depth is shown in figure 4.2 (b). The quantified spectral information can now be interpreted based on the curve signature. For instance, the interval where the mean spectral value is below 110 can be classified as shale, above 180 as sand and in between as sand-shale inter-bedded regions. However, it is seen that the quantified spectral information is an averaged image property at each depth and hence, is not revealing the real geology. This may lead to misclassification as seen in the shale interval and the sand interval followed by it in the middle part of the outcrop photograph. In this case, both regions are classified as sand-shale inter-bedded regions due to the averaging of the pixel intensity values. Further, the interpretation of the quantified averaged image property at each depth leads also to discrepancies in bed boundaries, as shown in figure 4.2 (c), and possibly result in the wrong estimation of the bed thickness. Hence, in order to fully exploit the information content of these geological images, methodologies is required which go beyond the traditional pixel-based statistical analysis and feature

extraction and should include the spatial characteristics for a meaningful and realistic geological interpretation.

Interestingly, many biological and natural objects tend to be irregular and variable in shape. This lead to the study on how image interpretation is done in remote sensing and medical imaging. In remote sensing, large aerial photos and satellite pictures are interpreted to distinguish roads, water bodies, houses, forest, and agricultural lands and in medical imaging, complex medical images are interpreted for tumor cells. Powerful signal processing methods are developed to explore information from high resolution remote sensing imagery of a large variety of space-borne and air-borne sensors which provide a large amount of data about the earth's surface for global and detailed analysis (Coulde and Pottier, 1996; Curlander and Kober, 1992; Haverkamp and Tsatsoulis, 1992; Pierce et al., 1994; Serpico and Roli, 1995; Tsatsoulis, 1993).

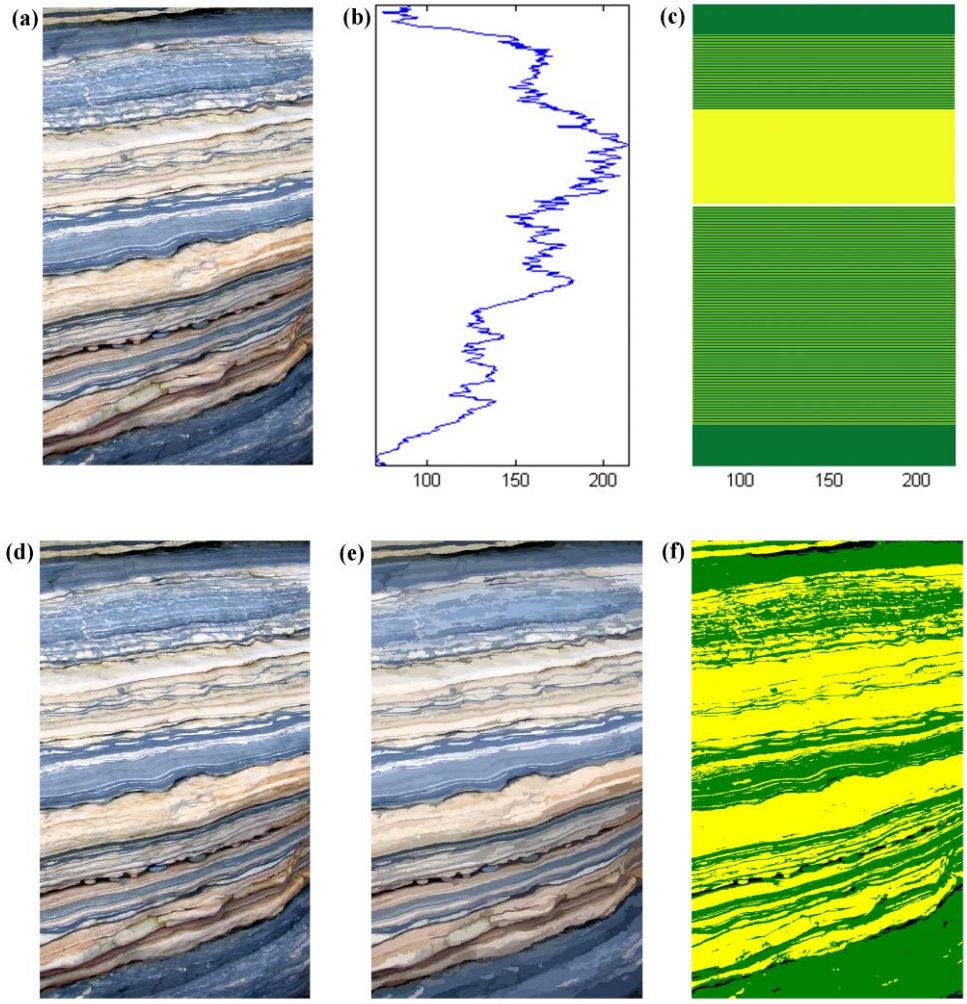

Figure 4. 2: *: A comparison of pixel-based and object-based outcrop photograph analysis; (a) outcrop photograph, (b) image property (mean of grey scale spectral intensity) calculated from outcrop photograph using pixel-based image analysis, (c) a possible lithology classification based on the quantified image property resulting in a single definite or probable class at each depth (yellow-sand, dark green- shale and light green –sand shale interbeds), (d) outcrop photograph, (e) outcrop photo segmented into image-objects, (f) outcrop photograph classified by grouping image-objects into lithology classes (yellow-sand, green-shale) based on spectral property. Note the identification of thin shale beds and exact bed boundaries in object based methodology.*

Consequently, an advanced image analysis methodology which groups neighboring homogeneous pixels together into an object (image-object)

(Blaschke and Strobl, 2001; Hay et al., 2001a; Hay et al., 2001b; Schiewe, 2002) is applied on the core photograph. Figure 4.2(d) shows the original outcrop photograph and figure 4.2(e) shows the photograph in terms of image-objects. Similar 'image-objects' based on their spatial, spectral and textural properties (Hay et al., 1997; Hay et al., 1996), can be related and assigned into appropriate lithology classes (figure 4.2 (f)). This is an extended signal processing approach for image analysis for the extraction of meaningful information from images. This advanced image analysis method is now being used widely in remote sensing (Benz et al., 2003, 2004) and medical imaging (Baatz et al., 2006) for effective image classification and is called "object based image analysis".

The methodology is detailed in chapter 2. This study is an attempt to give a flavor of object-based image analysis versus pixel-based image analysis for successful lithofacies or lithology identification. Hence, this chapter focuses on the classification results and does not explain the methodology in detail. A detailed explanation of the step by step execution of the methodology will be given in the following study (chapter 5). There are three major steps involved in object-based image analysis; (1) image segmentation, (2) knowledge-base design, and (3) classification of the image.

The outcrop photograph is first segmented, which results in grouping of similar neighboring pixels together to form image-objects as shown earlier in this chapter (figure 4.2 (b)). The parameters chosen for this image segmentation may vary according to the image interpreter's need. For example, to extract fine details such as thin beds, one may need to choose a smaller scale parameter (chapter 2) and to extract bulk properties one may need to a use large scale parameter. However too small a scale value will

result in too many small objects and hence, may not result in a meaningful classification (as in pixel-based image analysis). Similarly too large a scale parameter may result in inappropriate few image objects in the entire image which again is not useful for a meaningful image classification. Hence defining the segmentation parameters is entirely dependent on the interpretation requirements and image type. An example of this will be discussed in the results and discussion section of this chapter.

Once the outcrop photograph is segmented, a class hierarchy is defined which is entirely dependant on the local geological heterogeneity. Thus, we incorporate the ground truth, and the expertise of the geologist for a meaningful image classification. The features of the segmented image-objects are calculated. In the outcrop photograph shown in figure 4.2 (c), the sand and shale interval can be clearly distinguished based on their spectral property. Hence, the mean of spectral value of all pixels in the image-objects, can give a meaningful image classification. However, the silty-sand region in the figure is distinguishable from the rest based on the encoded textural property in the image (in qualitative visual interpretation, the silty-sand towards the top of the figure is identified based on the inter layering or intrusion of the sand layers in the shale intervals. Here, the textural property of the image is used in distinguishing heterogeneous silty-sand region from the rest homogeneous regions). Thus, training the classifier based on the human logic and interpretation skills (chapter 2) can result in a successful image classification analogous to that obtained by an interactive qualitative interpretation.

4.4 RESULTS

The classification of the outcrop photograph is performed to distinguish sand and shale regions. Figure 4.3 shows the original outcrop photograph (a) used in this study along with its classification (b). The classification clearly distinguishes every sand region from shale, including thin beds. The figure also shows how effectively the spatial information has been utilized resulting in a classification that closely matches with the qualitative visual interpretation of the same by a geologist. This outcrop photograph simplified in terms of the lithology is now understandable to a non-geologist too.

The black colored regions in the classified outcrop photograph belong to unclassified regions. These are image-objects which do not share or belong to the feature range defined for the classes in the class hierarchy, sand and shale in this case. A close observation of the classification result reveals that the top unclassified region is the resultant of shadow in the original outcrop photograph. The unclassified region at the bottom belongs to a layer of soft sediment deeply eroded and hence is not visible in the photograph.

It is not always true that image-objects that belong to shadow regions will remain unclassified. It happens only when the regions have a distinct feature range as in the example given in figure 4.3. Presence of shadow can lead to misclassifications as well; an example is given in figure 4.4. In this figure the image-objects in the top, marked as (c), have spectral values different from the defined spectral range for sand and shale and hence are unclassified. However, the shadow at (d) and (e) lead to misclassification of sand as shale since the shadowed sand shared the spectral value with that of shale.

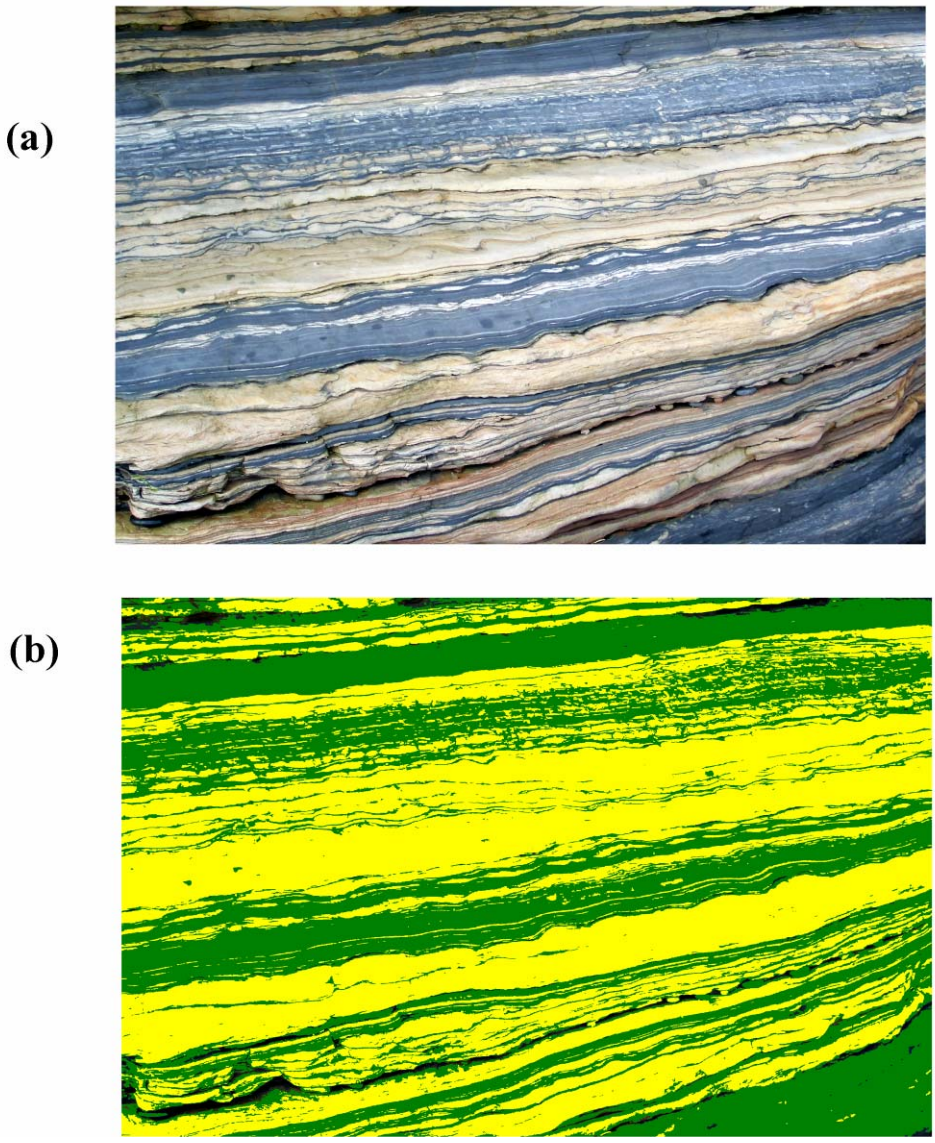

Figure 4. 3: *Automated classification of outcrop photograph: (a) original outcrop photograph used in this study (in terms of simplified image analysis, dark colored regions belong to shale and light colored regions belong to sandstone) (b) classified outcrop photograph which clearly distinguishes every sand (yellow) and shale (green) regions. The black colored regions in the classified outcrop photograph are unclassified regions.*

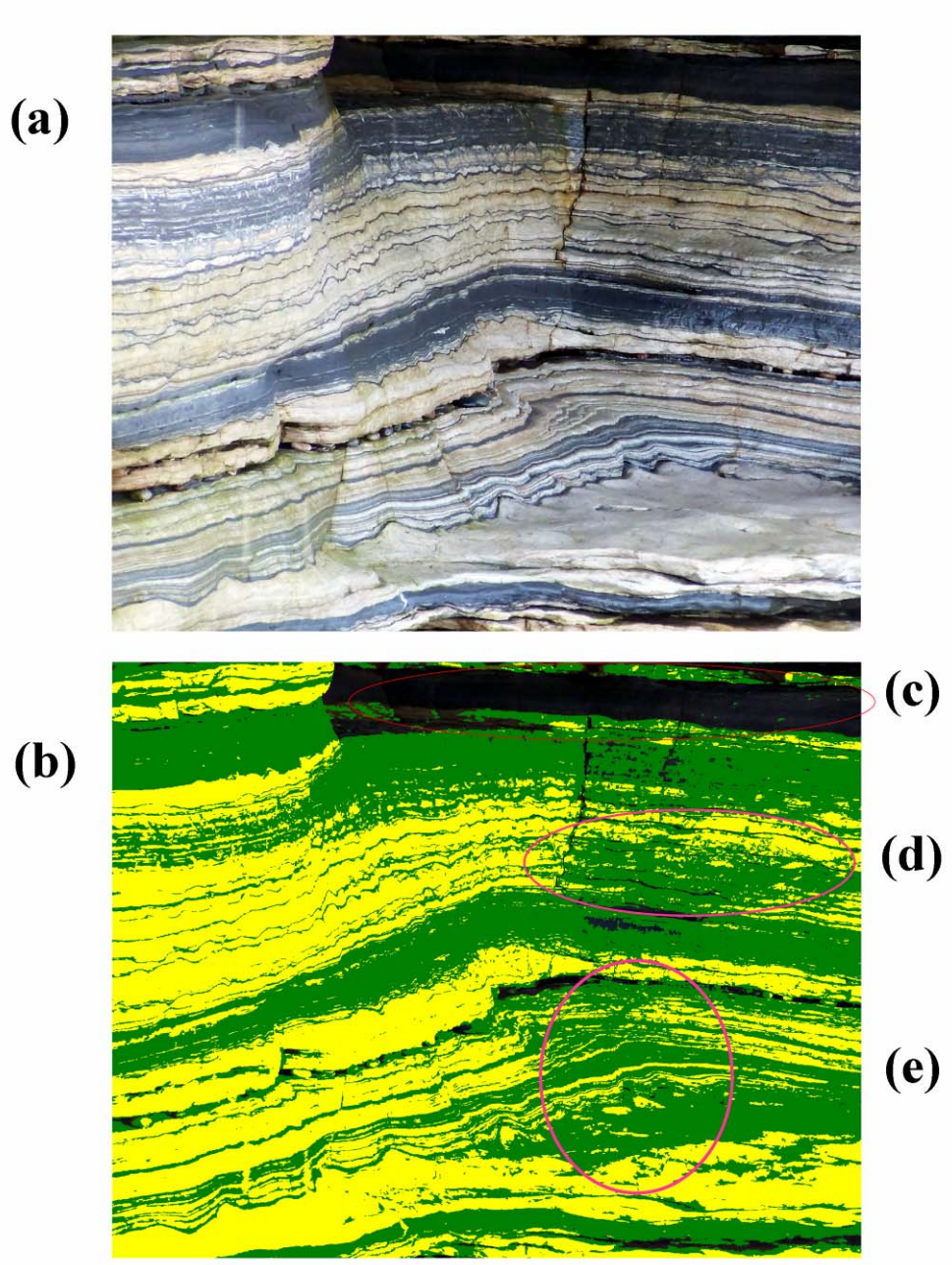

Figure 4. 4: *Effect of shadow in automated classification result: (a) original outcrop photograph used in this study (b) classified outcrop photograph. Figure key is same as that in figure 4.3. The black shaded region marked as (c) belongs to*

unclassified region due to shadow. Note the misclassified regions due to shadow at (d) and (e).

4.5 DISCUSSION

The important point that stands out is that we are using a supervised classification methodology with the user interactive platform. The user interactive knowledge-base design - defining the class hierarchy, feature selection and feature range definition of each class based on which the classification is performed - offers an excellent platform to refine the classification result at any stage. Thus one could define the unclassified region as shadow and thus obtain an accurate outcrop photograph classification of the figure shown in figure 4.3. However, the misclassifications of the outcrop photograph shown in figure 4.4 at (d) and (e) were the outcome of image-objects having the same feature value due to the shadow. This is clear from figure 4.5 which shows the segmented image-objects of the outcrop photograph in terms of their spectral feature (mean of spectral value of pixels in each image-object). Although these types of misclassifications can be eliminated by taking photographs in proper lighting so that the images used for study contain characteristics of the real geology, in most of cases a combination of both spectral and textural property included in classification may lead to a successful geological classification.

An example of the outcrop photograph classified based on both textural and spectral property is shown in figure 4.6. The sand-shale inter-bedded region has been distinguished from the sand cross-stratification based on the image textural properties (homogeneity and mean spectral value (chapter 2 and 3)). Note that, the shadow in the image has not affected the classification as the classes under consideration were clearly distinct in their textural properties.

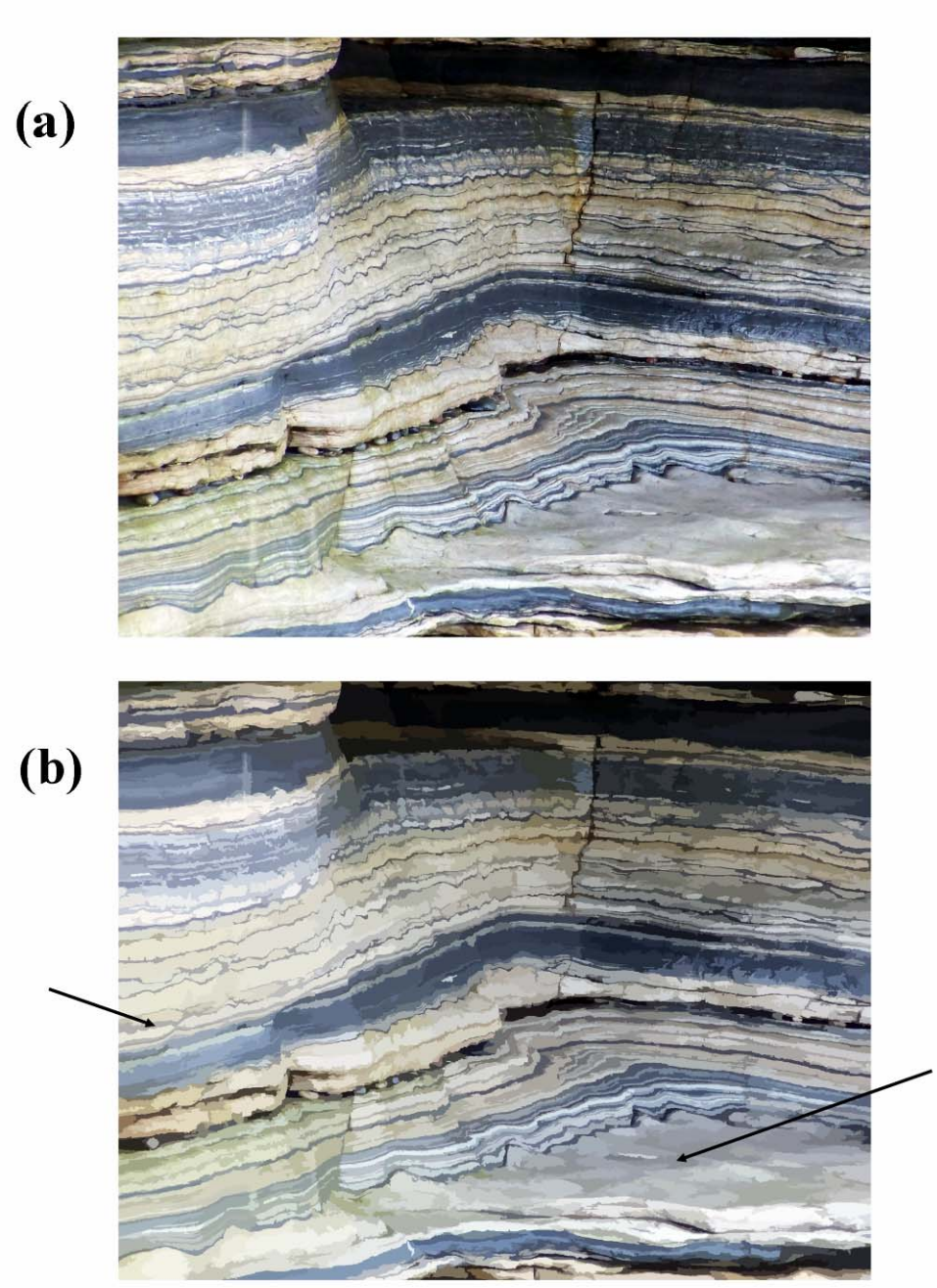

Figure 4. 5: *(a) Outcrop photograph, (b) segmented outcrop photograph. Note that the image-objects pointed by the arrows have same spectral property but, belongs to two different rock types, shale (right) and sand (left).*

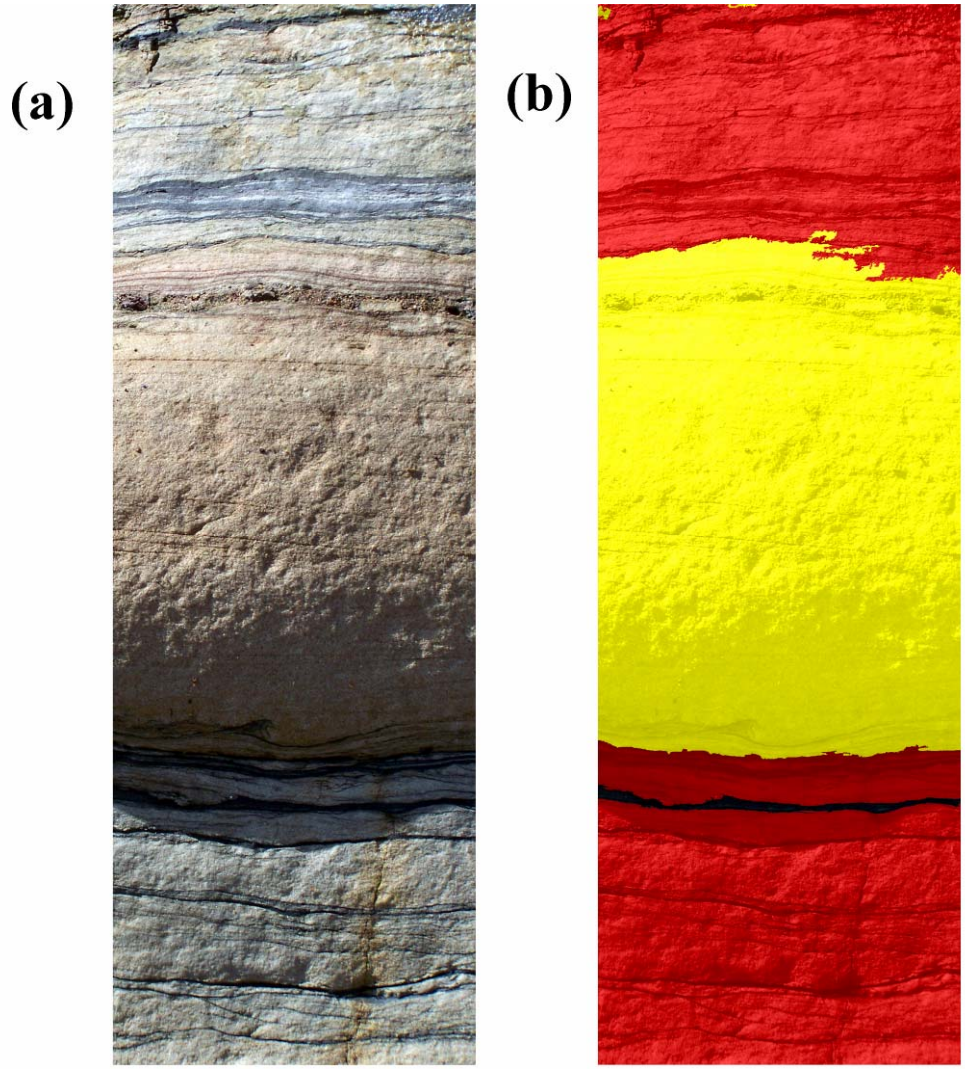

Figure 4.6: *(a) outcrop photograph used in the study, (b) classified image: sand-shale inter-bedded region (red) has been distinguished from the sand cross-stratification (yellow). Note that the shadow in the image has not affected the classification as the classes under consideration were clearly distinct in their textural (homogeneity) properties.*

Thus, this methodology offers the flexibility to use one or more features for an appropriate image classification as explained in the methodology section in

chapter 2, resulting in a realistic image classification taking into account the spectral, textural and spatial characteristics.

Compared to the segmentation parameters used in outcrop classification shown in figure 4.3 and 4.4, which aimed at distinction of even fine shale layers, the segmentation parameters used in the second photograph shown in figure 4.6 were larger resulting in grouping of more pixels together. This resulted in a successful textural and spectral property evaluation and hence, a classifications close to the ground truth. Thus the inclusion of human logic and reasoning helps in adapting the methodology to suit any classification requirements which make it an ideal tool for geological image interpretations.

4.6 CONCLUSIONS

The properties in geological images such as outcrop photographs, core photographs and image logs, can be irregular and variable in texture, shape and size. The properties may vary from field to field, within a field and even with depth in a single well. Hence, to deal with each unique data type and field, a methodology is required where the expertise of an image interpreter can be incorporated within the classification method both to define classes present in the selected field, and to define each class by assigning representative samples to train the classifier along with the computational power of the computers. We have proposed an apt methodology and illustrated its effectiveness in classifying an outcrop photograph in this chapter. The methodology will be extended for an automated core photograph classification in the coming chapter along with the development of a protocol which will be applicable on any number of similar data sets from identical geological settings.

Chapter 5

AUTOMATED LITHOLOGY EXTRACTION FROM CORE PHOTOGRAPHS

Summary: Chapter 4 discussed how an Object-Based Image Analysis (OBIA) methodology can be used for an effective outcrop photograph classification analogous to the interpretation of the same by human eyes. Following this outcrop photograph classification, this chapter will focus on whether the same methodology can be extended for an effective automated classification of core photographs. Once an optimum classification of the given core photograph is achieved, attempts will be made (section 5.2) to code all optimized classification steps, as detailed in chapter 2 and 4, into a protocol which can run on any intervals of data for an automated lithology classification from core photographs. The coded protocol, in principal, should be applicable on any core photograph from similar fields, giving an automated classification to simplify labor-intensive visual interpretation of core photographs. Section 5.3 shows the testing and verification of the developed protocol on two core photograph intervals. The accuracy of the automated classification is assessed by comparing it to a geologist's interpretation (section 5.4) leading to the conclusion of the chapter, section 5.5.

5.1 INTRODUCTION

Lithologies or rock types within any reservoir formation can be inferred from a combination of surface geophysical and well log data. However the ground truth is reflected in extracted core which must be examined manually by an expert geologist for lithological classification. This is a highly laborious and time consuming process. Also, large sections of core are not easily portable, and cannot be distributed in their entirety to more than one place at once.

The core also inevitably deteriorates with age either naturally or by excessive handling and sampling (Blackbourn, 1990). Cores are usually stored in some remote core store where warehousing is cheap, and visits are therefore made only in cases of special need.

As a result 3D x-ray core scanning and core slab photographing are becoming more and more commonplace leading to the availability of high quality digital data of the core. This information about the subsurface is mobile, can be distributed freely, and does not deteriorate with age. These digital data can be copied and are accessible at any time according to demand.

Lithological classification can also now be carried out based on the colour and texture patterns of these high quality digital images. However, this approach requires dealing with a large amount of raw, digital data. Therefore automated classification, which can complement the skills of reservoir characterization professionals engaged in interpreting core photographs will be a significant advance. An object-based image analysis (OBIA) methodology is proposed in this chapter for automated lithology extraction from core photographs.

5.2 STUDY AREA - THE SOUTH BATRA FIELD

5.2.1 Introduction

The data used in this study is from South Batra field located in El Mansoura Concession, Nile Delta, Egypt. South Batra is an onshore gas field discovered in 2003 and operated by Mansoura Petroleum Company a government joint venture company with Melrose holding a 50% interest. The field is located to the North of Cairo, west of the Damietta branch of the Nile and south of East Delta Field.

Core and well log data used in this study are from the well South Batra-20, the location of which is shown in figure 5.1. The well has a 20° deviation over the cored section and was drilled to a depth of 10,408 feet/3172.36 meters. The well helped in clarifying the areal extent of the South Batra field towards the South (www.oilegypt.com). The reservoir sands are Late Miocene (Messinian) in age and are part of the Abu Madi Formation termed Level III.

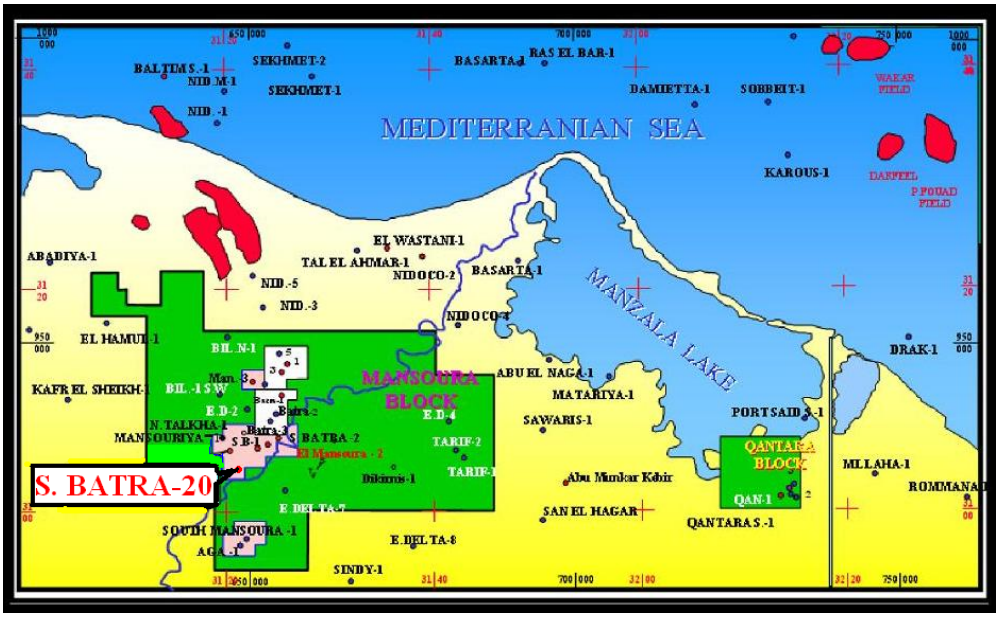

Figure 5.1 *: Map of the study area showing key wells (taken from Melrose_Resources). Data from well 20 is used in this study.*

5.2.2 Geological Setting and Stratigraphy

Fall in sea level during the Late Miocene resulted in major erosion on the Nile Delta and deep incised valleys being cut. The Abu Madi incised valley trends north through El Mansoura Concession forming an important Play Fairway with fluvial and estuarine sands of the Abu Madi Formation forming the

reservoir target. A string of discovered fields, such as East Delta to Abu Madi to the offshore Baltim fields, lie within the Messinian incised valley. A geological depositional model for the Abu Madi reservoir is shown in figure 5.2. The cored depth interval used in the study is fluvial/estuarine sand and shale. It has rippled, cross bedded and massive sands and laminates silts/shales.

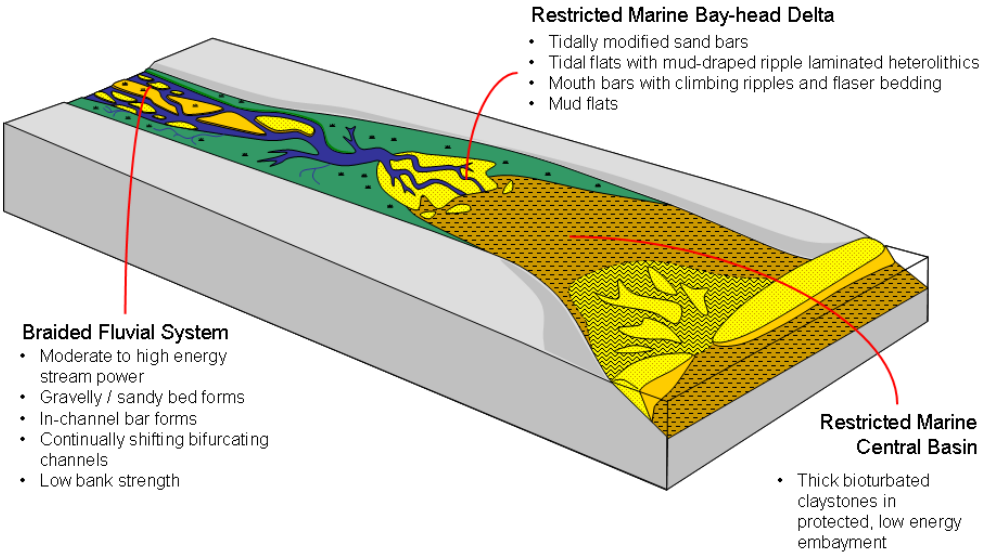

***Figure 5.2**: Geological depositional model for Abu Madi reservoir (Taken from Melrose Resources Plc).*

5.3 METHODOLOGY

The methodology is detailed in chapter 2 and its application to an outcrop photograph is shown in chapter 3. The main steps in OBIA are

- Image segmentation
- Knowledge-base design
- Image classification

The parameters and rules that influence each of these steps are image dependent and should be changed according to the image type, and the output requirements. Hence, they are determined by experiments on the given data set. These parameters and the rules that influence each of the individual steps in this methodology can be coded into a protocol so that it can be used on other similar images for automated classification. A protocol, in this context, can be defined as a set of rules and controlling parameters that are arranged in sequential order and work together to automate image classification. The so developed protocol can perform automated image classification on any amount of data, and also in similar types of images from similar fields, or on different fields with appropriate modifications to suit the new field. This chapter deals with the development of an automated lithology extraction protocol and its application to a core photograph.

5.3.1 Data selection

The aim is to facilitate rapid automated classification of core photographs of the entire well using the protocol. Since developing the protocol by classifying the entire core photograph is a time consuming and tedious task, a small representative interval of the core photograph is taken and a classifier is trained to distinguish different lithology classes based on their textural and spectral characteristics.

The trained and tested classifier can be used to obtain an automated classification of the rest of the core photograph and other similar core photographs. Hence, data selected for initial classifier training should be representative of the entire well, and chosen carefully so that they contain all the potential classes that need to be identified. Failure to adequately represent all classes will lead to misclassification of the core photograph.

Figure 5.3 shows an interval of the core photograph used for the protocol development. It consists of the following lithology classes: carbonate cemented sandstone (9924-9925 feet (3024.83-3025.14 meters), 9928.5-9929 feet (3026.21-3026.36 meters)), shale (9933-9934 feet (3027.58-3027.88 meters), 9936-9938 feet (3028.49-3029.10 meters)), and sandstone (9925-9927 feet (3025.14-3025.75 meters)). There is also a fourth class which we call "no-core", and are regions where either core was missing during coring, or pieces were taken for core analysis and labeled as preserved sample. Each lithology, in this case, varies by its spectral properties based on which our eyes could easily distinguish them.

This study is an approach to train the classifier to classify core photographs in a way analogous to how it is carried out using our eyes; hence these distinguishing spectral properties are used to train the classifier to perform an automated lithology extraction. For example, in figure 5.3, the dark regions represent shale, light colored regions represent carbonate cemented sandstone, intermediate colored regions represent sandy regions and the white background intervals represent the no-core regions in the core photograph.

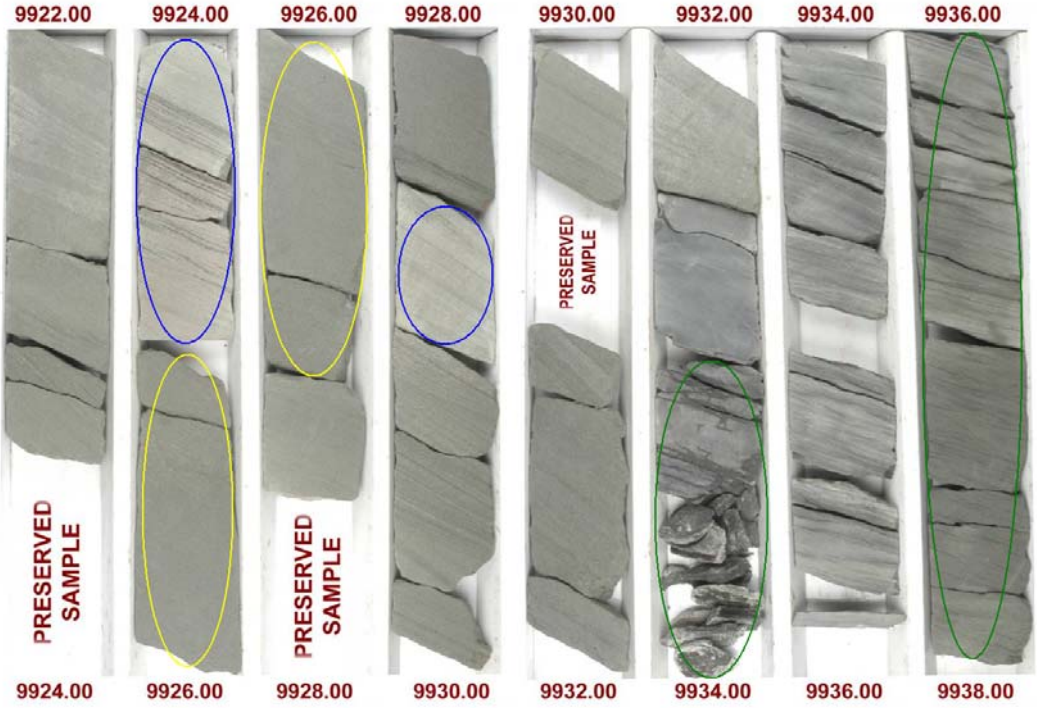

Figure 5.3: *Core photograph used to develop the protocol for the automated lithology identification: We start with a simple lithology consisting of carbonate cement (eg: blue circled regions), shale (green), and sandstone (yellow). The white regions in the core photograph are regions where either core was missing during coring or taken for core analysis and labeled as preserved sample;, we add another class called 'no-core' for these regions in the core photograph classification (depth given is in feet).*

5.3.2 Protocol Development

Since a well trained classifier can be used on other similar core photographs and possibly on core photographs from other wells and fields with minimum effort, all parameters that best classify the core photograph, defined based on the experiments on the core photograph used in this study, are coded as a protocol. A schematic representation of the various steps recorded in this protocol and the experiments involved in finalizing each of these individual

steps are detailed in chapter 2 (figure 2.9) and are detailed in the following section.

5.3.2.1 Image Segmentation

The first step in OBIA is image segmentation. As explained in Chapter 2, the core photograph was segmented into objects by combining similar, neighboring pixels together. Our results show that the best lithology extraction from core photographs was obtained when S, weights for $h_{spectral}$, and h_{shape} (*compactness* and *smoothness*) were given values of 10, 0.9, and 0.1 (0.5, and 0.5) respectively (chosen interactively based on qualitative evaluation of the image segmentation results of the core photograph), but these values may vary depending on the specific field and lithologies or rock types considered as explained in chapter 4. Definitions of these parameters were given in Chapter 2.

5.3.2.2 Knowledge-Base Design

Object-based image analysis incorporates both the power of computers and human knowledge to classify an image. A knowledge-based scheme (which includes human interaction) is used for defining possible classes present in the core photograph, training a suitable classifier by selecting representative objects for each class, and defining features that could distinguish objects belonging to various classes. The main steps in the knowledge-base design are detailed below.

Defining class hierarchy: *A priori* counting and naming of the classes is done based on examining core, core data, core photographs and other geophysical logs. Based on this knowledge, a class hierarchy, which contains all classes in the desired classification scheme, is developed. The defined class-hierarchy includes sand, shale, carbonate cements and no-core regions. The no-core class

represents core intervals that are either missing or taken as preserved samples for core analysis.

Defining appropriate image-object features: Segmented objects can be grouped into various classes based on their characteristic features. Hence, various features which can distinguish the segmented objects that belong to different lithology classes are calculated. For example, the mean of spectral values of all pixels forming each object, their standard deviation, and maxima of the spectral value of each image object are all used in this case. Figure 5.4 shows a cross plot (feature space) of these calculated features showing a clear separation of objects that belong to various lithology classes defined in the class hierarchy.

As explained in chapter 3, not all features related to spectral property will lead to a successful classification, for example, figure 5.5. From figure 5.4 and 5.5, it is clear that though mean of spectral value leads to a successful distinction of the class, mean spectral value difference to the brighter objects or to the neighboring objects is not showing distinction between objects belonging to the three different classes. Hence, as explained in chapter 3, a detailed study on features has been done, in this case by cross plotting and qualitatively analyzing features that shows a good distinction between the objects belonging to different classes.

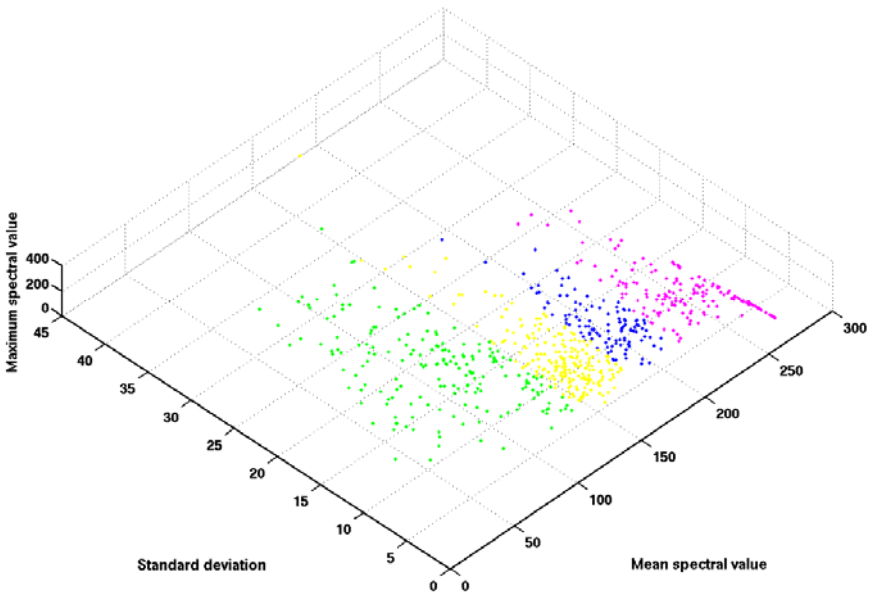

Figure 5.4*: A cross plot of different spectral features of the image objects, showing a clear separation of image objects belonging to various classes; carbonate cements (blue), sand (yellow) and shale (green), and no-core (purple) in the class hierarchy.*

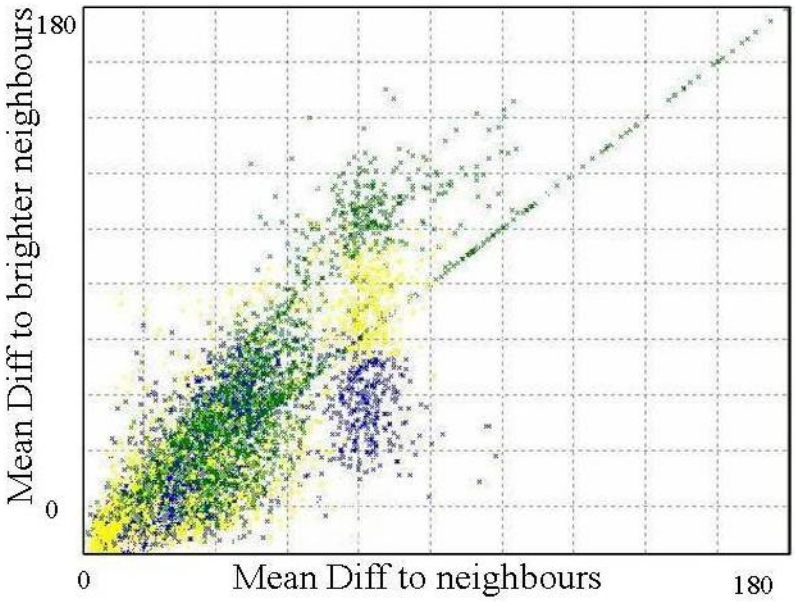

Figure 5.5*: A cross plot of different spectral features of the image objects, showing a non clear separation (a chaotic distribution) of image objects belonging to various classes; carbonate cements (blue), sand (yellow) and shale (green) in the class hierarchy.*

Selecting appropriate classifier: As more than two features were used to distinguish the individual classes present in the core photographs (figure 5.4), using a Nearest-Neighbor classifier would be ideal (explained in Chapter 2).

Training classifier with appropriate sample objects: In Nearest-Neighbor classification, the feature range that would represent each class is defined by appropriate sample selection. These samples are selected to represent the entire feature range for each class, summarizing all different heterogeneous appearances in one class. The feature ranges defined by these selected samples are used to train the classifier for further classification.

5.3.2.3 Image Classification

Classification is a process of assigning each segmented object to appropriate classes (lithology in this case). The nearest-neighbor classifier is trained based on the developed knowledge-base and the trained classifier is used for the lithology classification of the entire core photograph.

The principle of image classification is that each object is assigned to a class based on its characteristic features, by comparing it to the predefined feature ranges in the feature space. Doing so for all the image objects result in image classification. Hence, once the classes have been defined in the feature space, each image object is compared to the defined feature range of each class and assigned to the corresponding class (Chapter 2). Figure 5.6 shows the classification of the core photograph shown in figure 5.3, obtained using this methodology.

The classification result is then compared with the visual interpretation of the core photograph, and is further revised, if need be. Wrongly classified objects, if any, are moved to the correct class either by adding or removing a few sample objects to the training sample sets, to attain the desired classification. Hence, by examining the classification result, the objects selected to train the classifier are further refined and thus we optimize the (interpreter-derived) knowledge-base that is used for automated core photograph analysis.

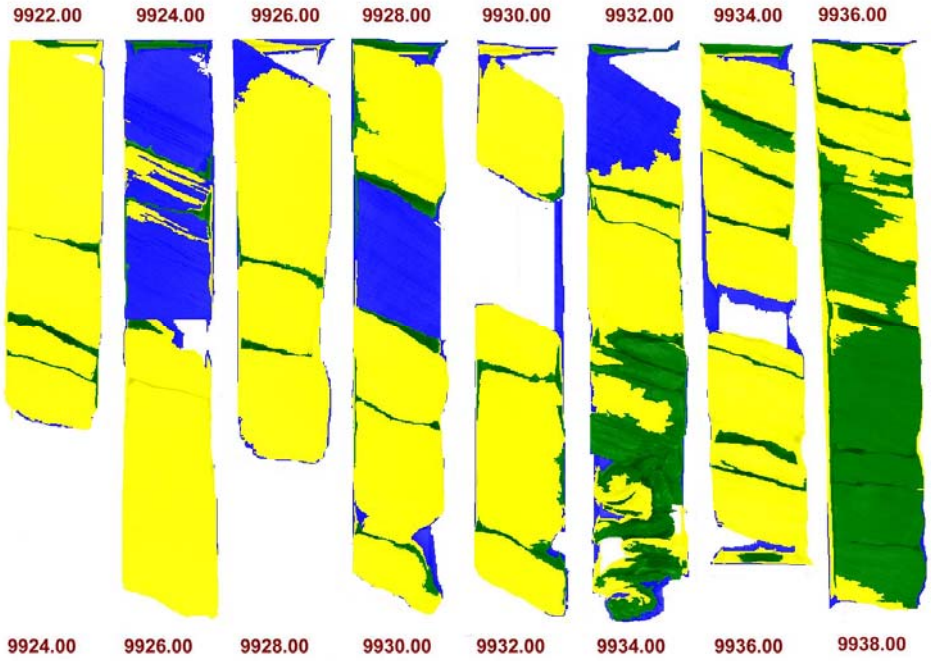

Figure 5.6: *Classified Core photograph (sand-yellow, shale –green, carbonate cements-blue, no-core or preserved sample regions–white. The core photograph used for this classification is shown in Figure 5.3.*

The classifier training is refined using the knowledge-base incorporating the expertise of an image interpreter, and is saved as a class hierarchy "mask", which acts as a library of defined features and distinguishing feature ranges for each class in the class hierarchy, defined and finalized by the above interactive sample selection for each class. The same saved class hierarchy mask can be used to classify similar core photographs. By calling up this class hierarchy mask, the protocol incorporates the knowledge derived from the training areas using the predefined feature space, and thus all segmented objects are compared to these feature ranges in the feature space and are classified accordingly, and automatically. However, this can only be used on similar

core photographs as the classes at this point are pre-defined and hence the features and feature ranges could distinguish these classes only.

The protocol can be adapted in two ways when classifying core photographs from different geological settings:

1) Run the protocol step by step while editing the class hierarchy mask manually to suit the new field.

2) Update the class hierarchy to suit to the new field before running the protocol, and then run the protocol for an automated classification.

In either case the existing class hierarchy can be used as a reference for class arrangement, feature selection, and classifier selection. The rest of the protocol, mainly the segmentation parameters used to generate the image objects by combining adjacent similar pixels together, should work for any field as this part of the process has been optimized by testing on a large number of core photographs (though it could of course be refined further depending on the specific field and lithologies or rock types to be considered).

5.4 RESULTS AND DISCUSSION

5.4.1 Testing of the Protocol

As a first test of the protocol, the same interval of the core photograph that was used for training the classifier is classified automatically using the protocol. The core photograph has been interactively spliced vertically with depth so that it can be easily compared with other geophysical logs and has been depth matched with reference to the image log.

Figure 5.7 shows the classified core photograph using the protocol plotted against depth. The classified core photograph is shown in the right hand side of the figure, where the yellow color is sand, green is shale, blue is carbonate cementation, and white regions are where either core was absent or taken as a preserved sample for further core analysis. The grey image left of the classified core photograph is the original core photograph used for the automated classification. Left of the core photograph are the neutron and density logs where yellow shades indicate presence of sand and wide green regions indicate shale. The presence of carbonate cements is not clear from the standard logs while the resistivity image, to the left of the caliper and gamma logs, shows fine details of the borehole. The white regions running left to right in the resistivity image logs indicate carbonate cement, which correspond well to our core photograph interpretation.

5.4.2 Verification of the Protocol

The successfully tested protocol is then applied over another interval of the core photograph which was not used for the initial protocol development. Figure 5.8 shows the classification result on the new interval of the core photograph plotted against depth, along with the original core photograph, resistivity image, and caliper, gamma, neutron, and density logs; the figure key is similar to that of figure 5.7.

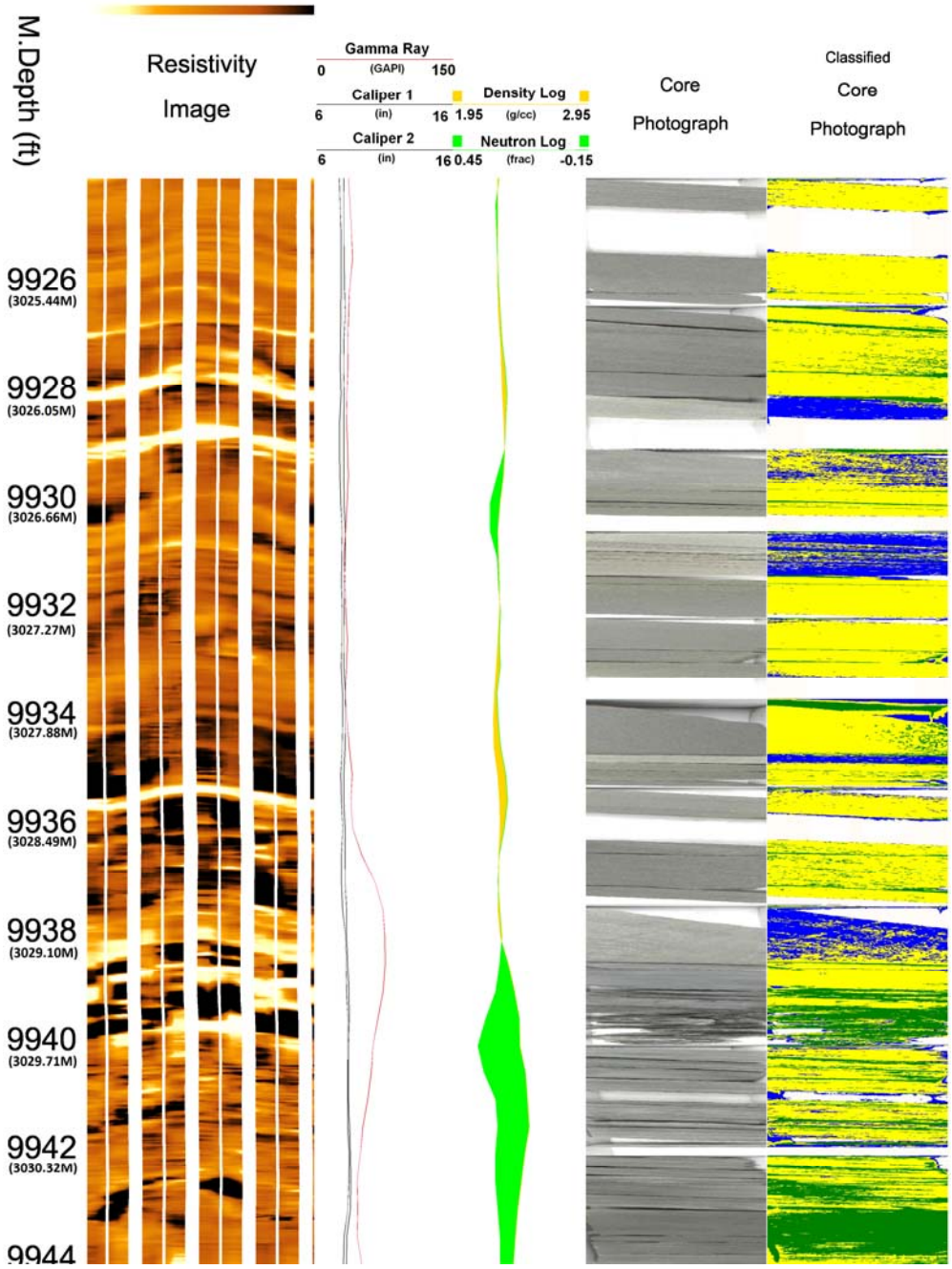

Figure 5.7*: The core photograph classification result: The figure shows, from left to right, the depth interval, image log, gamma log and caliper logs, neutron and density logs (most of the yellow shaded region indicates sand and green region shale), core photograph used for this study and classified core photograph using the Object-Based image analysis. In the core classification, the yellow regions indicate sand, green shows presence of shale, blue indicates carbonate cement, and white the no-core regions.*

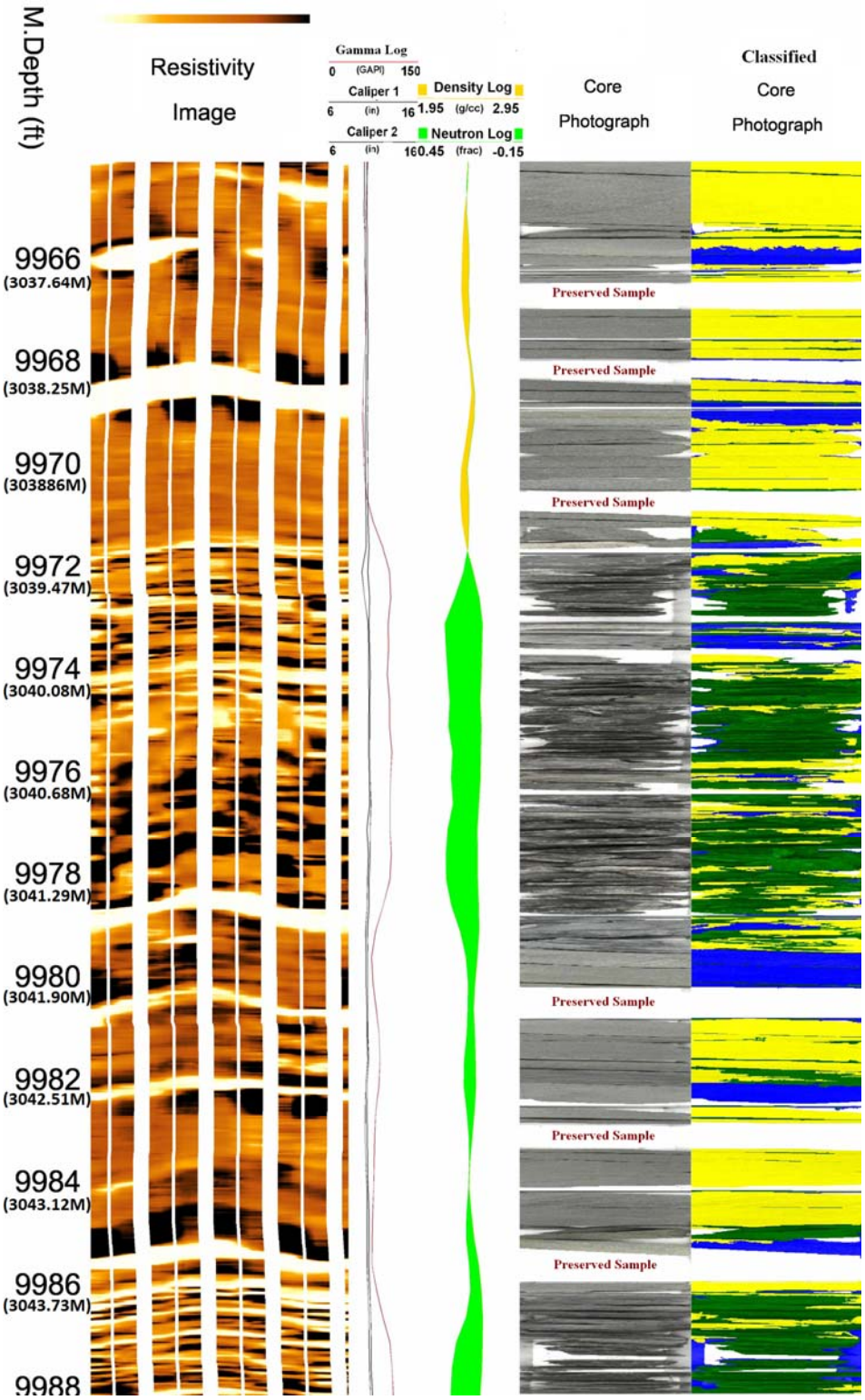

Figure 5.8*: testing of the classification protocol: the figure key and color key are similar to figure 5.7*

5.5 ACCURACY ASSESSMENT OF THE RESULT

The classification result is then compared with a qualitative, independent geologist's interpretation based directly on core photographs, which is taken as the ground truth. An accuracy assessment of the automated classification is done by manually selecting samples of each class entirely based on the geologist's interpretation, and comparing them to the automated classification where the objects are assigned automatically into various classes based on the classifier training.

Figure 5.9 shows the feature space of two features (maximum spectral value of the image objects formed during image segmentation along the x-axis, and the standard deviation of the spectral value of image objects along the y axis). The segmented objects belonging to different classes are plotted based on the geologist's interpretation (big circles), and based on the lithology classes automatically assigned by classifier (small dots).

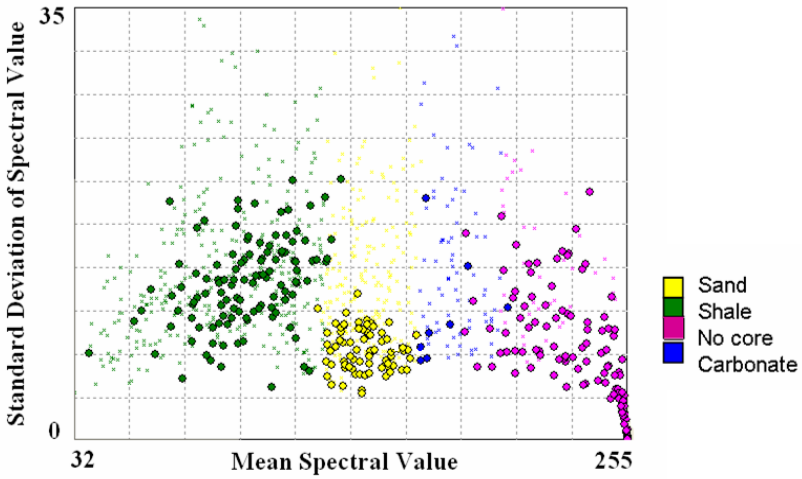

Figure 5.9*: Feature space distribution of the object samples – sand (yellow), shale (green), carbonate-cements (blue), and no-core regions (purple). Big dots indicate sample objects based on a geologist's interpretation and small dots represent object classes defined in the protocol based on the sample selection to mark each class.*

A one-to-one comparison of the results is shown in Table 5.1. Out of the 315 objects 297 classifications are correct in this case, giving an overall accuracy of 94.29%.

	Classification based on samples selected according to geologist's interpretation				
Classification based on automated method		**Sand**	**Shale**	**Carbonate**	**No core**
	Sand	76	5	0	0
	Shale	1	110	0	0
	Carbonate	0	0	8	12
	No core	0	0	0	103

Table 5.1*: Accuracy assessment of the classification obtained using the protocol by comparing the automated classification result with the geologist's interpretation. Table shows that out of the 315 objects, 297 classifications were correct, giving an overall accuracy of 94.29%.*

Automated Classification \ **Geologist's interpretation**	**Sand**	**Shale**	**Carbonate**	**No Core**
Total	**77**	**115**	**8**	**115**
Correct	**76**	**110**	**8**	**103**
Incorrect	**1**	**5**	**0**	**12**

Table 5.2*: A one to one comparison of the classification result of each class obtained using the automated classification method and the geologist's interpretation.*

Note that in particular, there were misclassifications in the regions where a core photograph was absent or had a shadow cast from the existing core pieces. Out of 115 objects assigned into the no-core class based on the geologist's interpretation, a total of 103 were correctly classified (table 5.1 and table 5.2) into the no-core class by this automated classification, while

12 objects were assigned into carbonate-cement class (table 5.1). From the classification result in figure 5.7, it is clear that these no-core region misclassifications were due to the shadows cast from the existing core (this can be seen on the classified core photograph at depth interval 9968 feet/3038.25meter) and some are due to the improper lighting (this can be seen at right and left sides of the classified core photograph intervals 9971-9978feet/3039.16-3041.29meters and 9987-9988 feet/3044.04-3044.34 meters). This is because some of these no-core regions with shadow shared the same spectral values as the carbonate. However this will not confuse the interpretation of the core photo obtained using this developed protocol, as the human eye can easily distinguish such cases. Ideally, such misclassifications can be removed if the core photographs could be taken against a background of completely different colour to the core, and the lighting was arranged to be directly behind the camera. If this form of misclassification was thus corrected, the overall accuracy would rise to 98.10%.

Interestingly, the fine variation in lithology at the interval, 9972-9978 feet/3039.47-3041.29 meters, has been clearly picked up by this automated classification. Qualitative interpretation of these kinds of fine details can be highly laborious and time consuming and can be performed only at a very small scale.

5.6 CONCLUSIONS

An automated method for lithology classification from core photographs using object-based image analysis technology is developed. This method combines both the power of computers, and human geological knowledge. A knowledge-based scheme involving human interaction is used to define possible lithology classes present in the core photograph, and to select

appropriate samples (objects) which belong to each lithology class. Later a classifier (used for automated classification) is trained to assign all unknown objects into appropriate classes based on this knowledge base. The methodology can be quickly adapted to core photographs from other geologic areas, with adjustments to the knowledge base used to train the classifier. The automated classification is then calibrated to a geologist's interpretation to ensure the accuracy of the new methodology and the good match between the two gives confidence in this new methodology. This work shows how the object-based image analysis method simplifies the labor intensive visual interpretation of core photographs. Object-based image analysis techniques offers a feasible, robust, and repeatable quantitative extraction of lithology information from core photographs, and offer an efficient and reliable approach to process large amounts of data. In addition, the methodology is applicable to several kinds of borehole images, for example wireline electrical borehole images or LWD images.

Chapter 6

AUTOMATED LITHOFACIES IDENTIFICATION FROM IMAGE LOGS

Summary: This chapter describes how the Object-Based Image Analysis methodology is used to develop automated lithofacies discrimination from image logs. Section 6.1 gives a small introduction to the chapter followed by the introduction of research question in section 6.2. Section 6.3, methodology, outlines a step by step tackling of the research problem with results of each experiment and necessary discussion of the preliminary result. Section 6.4 details the result followed by a discussion in section 6.5. Discussion includes both a one to one comparison of the automated lithofacies classification result with ground truth, the core based lithofacies interpretation made by a geologist and a comparison of the automated lithofacies predicted from image logs using image analysis at pixel level (chapter 3) and at object level (this chapter).

6.1 INTRODUCTION

The aim of this research is to develop automated lithofacies identification from image logs. So far an advanced image analysis methodology, the Object-Based Image Analysis (OBIA), has been used on outcrop (chapter 4) and core photographs (chapter 5). This methodology has been found to be useful in extracting information from these kinds of pictures, analogous to the qualitative interpretation done by an expert geologist. This chapter deals with work done to interpret image logs to discriminate lithofacies using the same methodology.

Image logs are digital images representing resistivity measurements of the formation acquired by special logging tools within a borehole (chapter 1).

Image logs contain detailed information on the structural, lithological, textural and petrophysical properties of the explored formation in the borehole as explained in chapters 1 and 3. These give a core-like picture of the borehole, but in terms of its resistivity responses. Hence, one need to study these resistivity responses recorded in the image logs and relate the spectral difference and patterns recorded in this pictorial representation of resistivity response of the borehole wall, and also combine information from conventional logs and core to successfully discriminate lithofacies.

6.2 RESEARCH QUESTION

The data used in this study is the same as in chapter 3 for pixel-based image analysis. The data analysis for the previous study showed that the sandy interval of core chosen is dominated by three types of lithofacies – horizontal stratification, cross stratification (in this example, the dominant type is hummocky cross stratification and there were only thin intervals of classic cross stratification. As image log analysis cannot differentiate these two from image logs alone, both were grouped together as cross stratification), and bioturbation (mostly silty sand and sandy shale). To begin with, the first two classes (horizontal stratification and cross stratification) were grouped into a single class as stratified sandstone or stratification, and the initial focus is on whether the image log used in this study distinguishes this class from the bioturbation. If yes, what are the main features based on which our eyes recognizes these two classes from image logs? Is it possible to obtain an automated image log classification analogous to manual interpretation by using those features that aided in a qualitative visual image interpretation? In the next step, attempts were made to subdivide the stratification into corresponding classes – horizontal stratification and cross stratification.

6.3 METHODOLOGY

The image log is pre-processed (chapter 3) and is correlated with cores and other geophysical logs to summarise the borehole image features of all lithofacies present in the formation. Initially, two intervals of the image log which marked a good distinction between bioturbated zone and stratified zone were joined together. Figure 6.1 shows the two intervals taken, depth 10042-10046 which is a bioturbated zone and depth 10068-10072, a stratified zone. In qualitative visual image log inspection, the interpreter could easily distinguish these two zones based on the embedded textural properties.

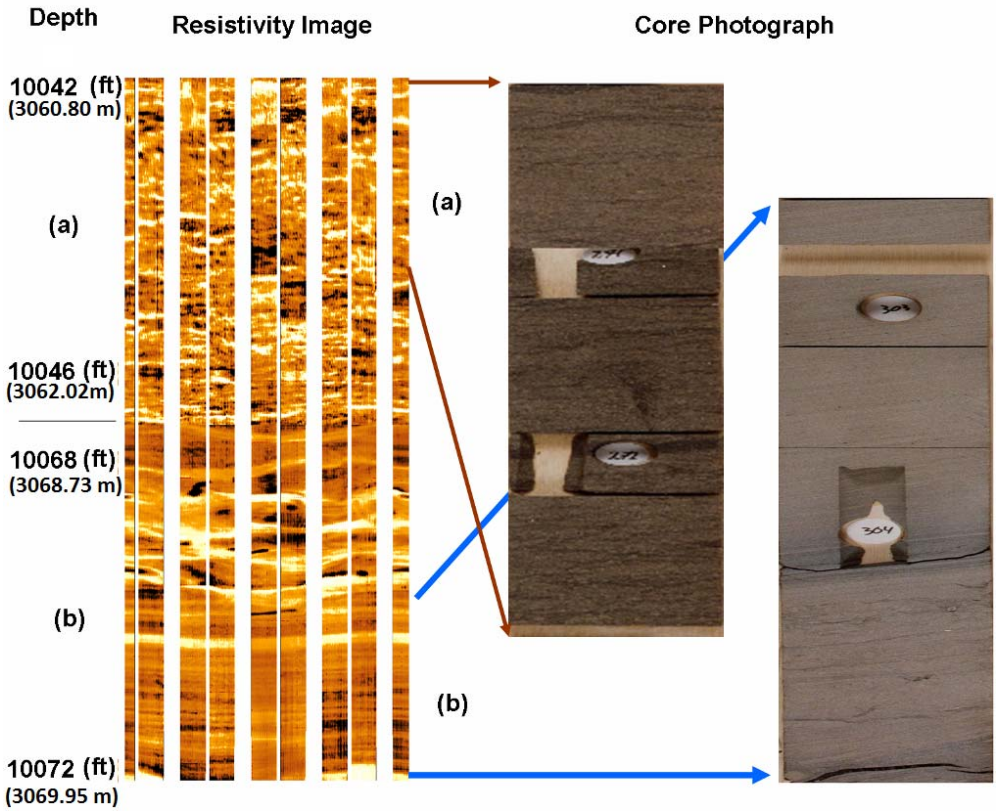

Figure 6. 1*: Image log showing two different lithofacies (a) depth interval 10042-10046 feet (3060.80-3062.02meters) shows a bioturbation (silty sand), and (b) depth interval 10068-10072 feet (3068.73-3069.95 meters) shows cross*

stratification and horizontal stratification region which we initially group into one class. Corresponding core photograph is shown to the right of the figure.

The same methodology that was used to classify outcrop and core photograph were followed on the processed image log with modifications to suit the new data set. The image log was segmented to create image objects and various spectral and textural properties of the image objects have been calculated. Among the various object features calculated, the GLCM textural features (explained in Chapter 2 and 3) were found to be appropriate to distinguish these two classes. Figure 6.2 shows a feature space, a cross plot of two textural features, homogeneity and dissimilarity, showing a clear separation of image objects belonging to the bioturbated and stratified regions. So these features have been used for further image log classification. Appropriate sample objects were taken to mark feature range belonging to each class and were used to train the Nearest Neighbor classifier (chapter 2) for an automated image log classification.

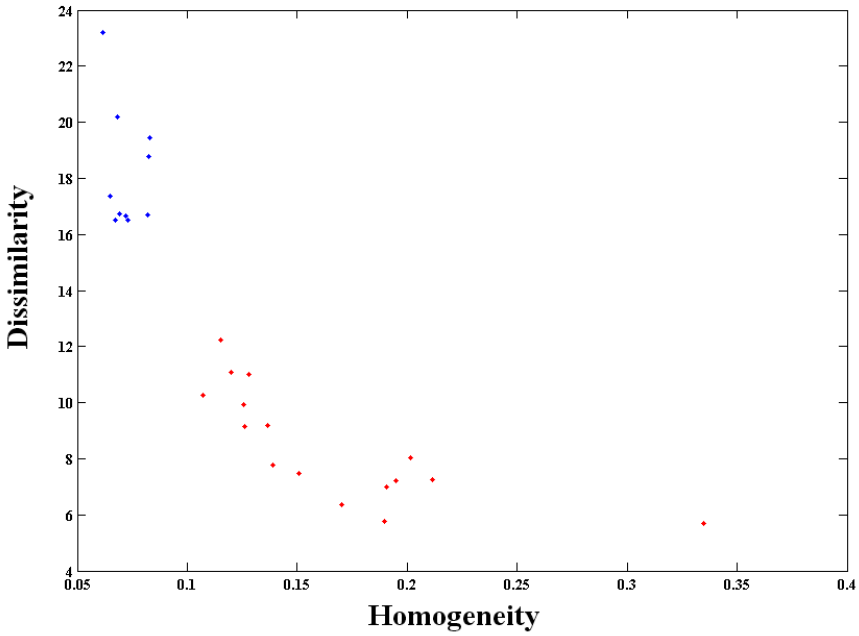

Figure 6. 2 *: cross plot of textural features - homogeneity and dissimilarity showing a clear separation of image objects belonging to bioturbated zone (blue) and stratified zone (red)*

Based on these selected samples a feature distribution is drawn and all segmented image objects that fall within each feature distribution were classified into appropriate class. The classification result along with the image log used and core photograph are shown in figure 6.3.

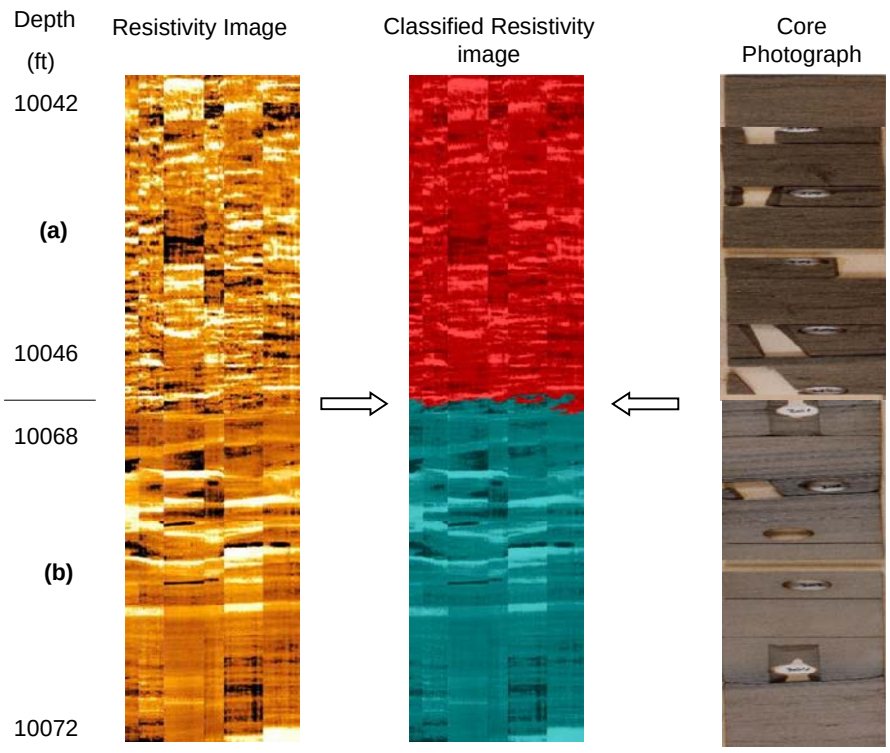

Figure 6. 3*: Classified image log into (a) bioturbated zone (red), and (b) stratified zone (blue) is given in the middle along with resistivity image log used for the classification (left) and corresponding core photograph (right).*

With this successful image log classification, the methodology is extended to a larger interval 10040-10090 feet/3060.19-3075.43 meters. The classified image log (column 6) along with standard logs – gamma and caliper logs (column 5), neutron and density logs (column 4), and the image log (static – column 2 and dynamic – column 3) are shown in figure 6.4. In order to obtain the best resolution of the fine lithofacies classes present in the field from the image log, the dynamic normalized images was preferred for the classification. This is because dynamic normalized images were found to be more useful for identifying bedding features characterized by a limited resistivity contrast. A

detailed explanation of dynamic normalized image and static normalized image is given by Rider (2004).

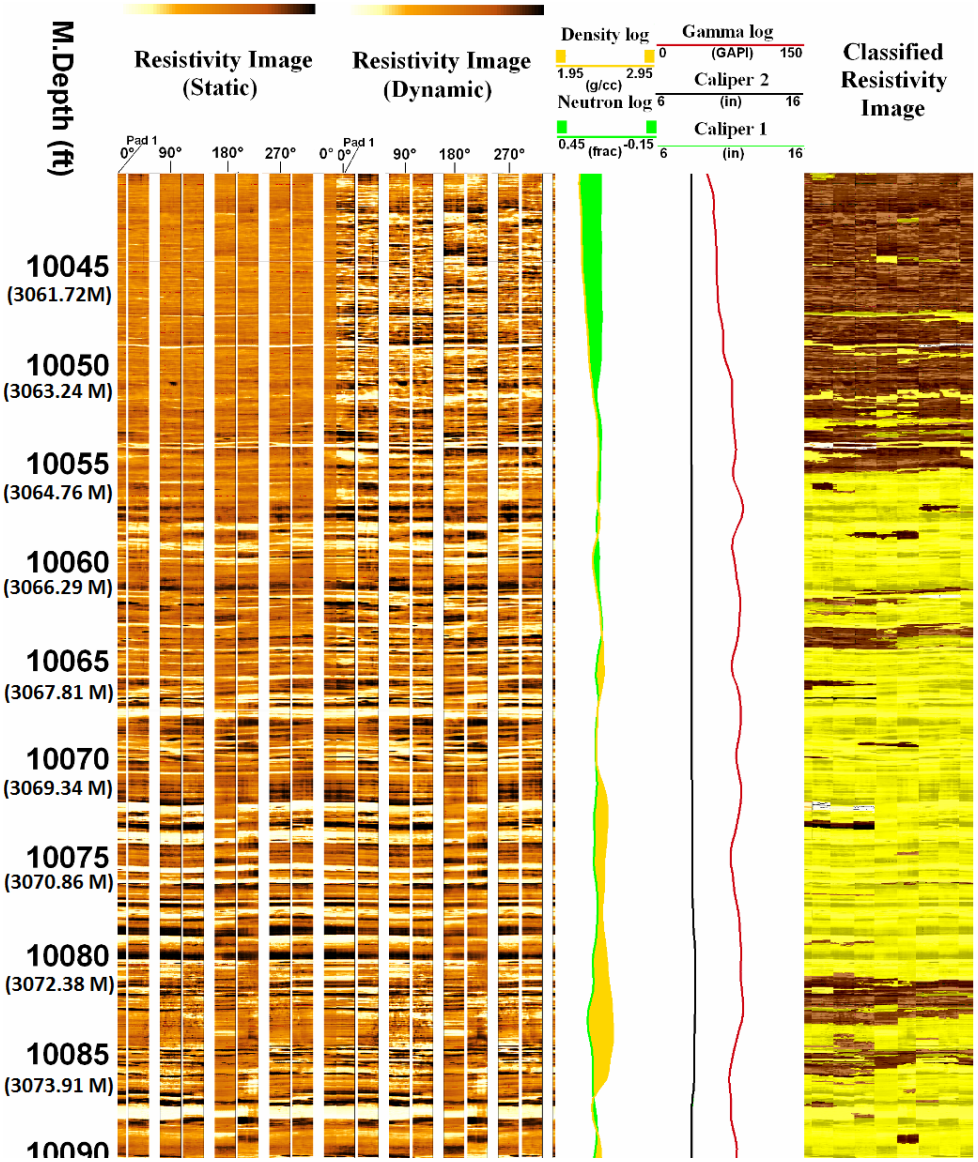

Figure 6. 4*: Image log classification result: From left to right; depth, the image log (static and dynamic images; image log used in classification is dynamic processed image), standard logs (neutron and density logs, and gamma and caliper logs) and the image log classified into bioturbated zone (brown) and stratified regions (yellow). The white regions marked in the classified image log are the unclassified image regions (explained as this study proceeds in the coming sections in this chapter). (Scale 1:60)*

The histogram plot of all objects created from the image log during image segmentation that were assigned into bioturbated (green) and stratified (yellow) classes based on the textural feature homogeneity, is shown in figure 6.5. The plot shows a clear separation of image objects belonging to these two classes. In this case, the textural properties were so distinct for the two classes that no overlap of feature has occurred. If there is an overlap, the classification will be done based on which class its fuzzy value is closer to. The blue bars in figure 6.5 belong to the unclassified regions shown in figure 6.4 and will be discussed later in this chapter.

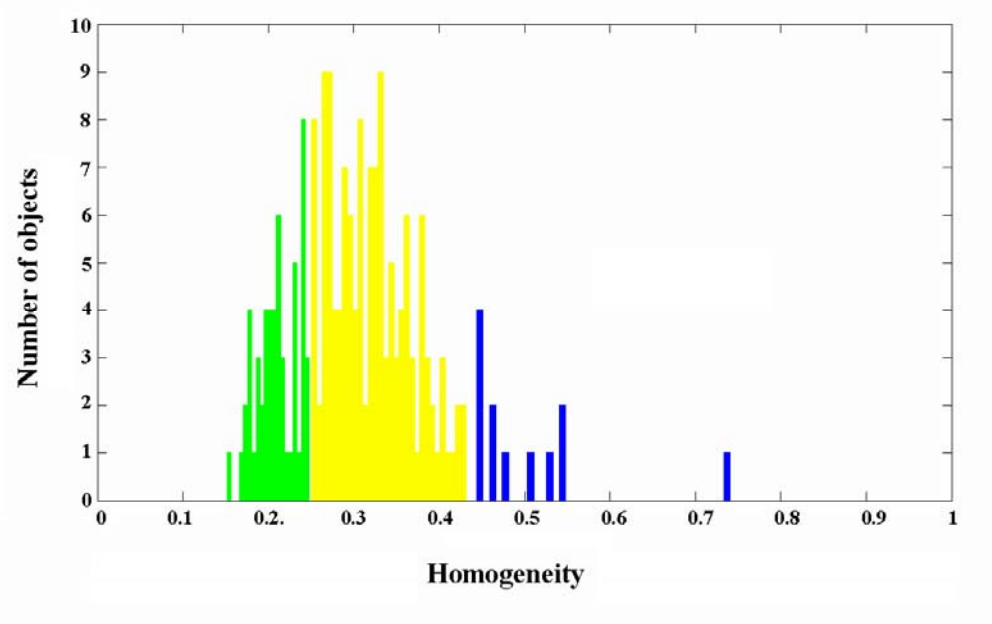

Figure 6. 5*: Histogram showing the clear separation of objects belonging to classes- bioturbated zone (green) and stratified region (yellow). The blue bars belong to unclassified objects which will be discussed later in this chapter.*

So far horizontal, and cross stratification are being grouped into the same class - stratified sandstones. The next step is an attempt to subdivide the stratified

sandstone into these two different classes based on textural information recorded in the image log. A careful examination of textural property of the image log corresponding to these two classes revealed that image objects belonging to horizontal stratification are much more homogeneous compared to that belonging to the cross stratification. Figure 6.6 shows image log parts belonging to these three classes – bioturbation, cross stratification (hummocky cross stratification) and horizontal stratification.

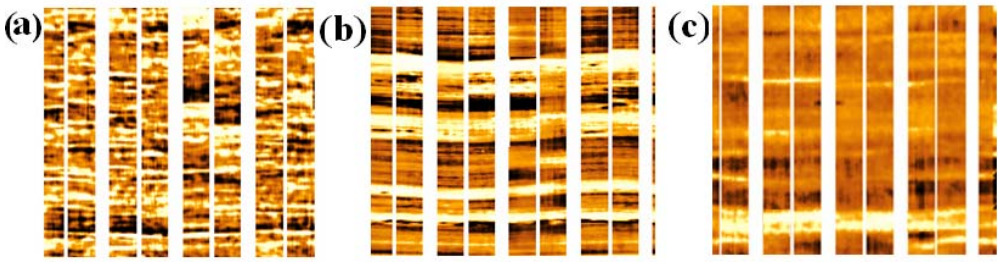

Figure 6. 6: *Image log belonging to (a) bioturbated zone (b) cross stratification (c) horizontal stratification. It is clear that image log from bioturbated zone is highly heterogeneous, while cross stratified zone more heterogeneous compared to horizontal stratification and less heterogeneous compared to that of bioturbated zone.*

The textural feature – homogeneity, calculated for the image has been evaluated for the range that distinguishes each class. Being highly heterogeneous, the homogeneity value for the bioturbated zone (figure 6.11), has been evaluated to be very low (0-0.25 in this case). The cross stratified region is found to be less heterogeneous compared to bioturbated zone but more when compared to horizontal stratification (0.25-0.32). The horizontal stratification was found to be the most homogeneous region among the three regions (0.32-0.42). This information was fed into the classifier system using a membership function (Chapter 2) to mark feature ranges for bioturbated,

horizontal stratification and cross stratification (This feature range can also be used to train a Nearest Neighbor classifier based on sample selection).

Figure 6.7 shows the classification of the image log into these three classes using this methodology. Manual/ interactive sinusoid picking were performed in the image log and from which the dips were calculated. This manual dip picking was carried out using TerraStation software (A number of software are available in the market for dip picking, and an advanced automated dip picking algorithm developed by us is detailed in next chapter) and is shown in the same figure. These dip measurements can be used as a reference to distinguish cross stratification from horizontal stratification (In this study, dip measurement below 10^{o} are considered as horizontal stratification and above 10^{o} as cross stratification).

The dip estimation from the manually picked sinusoid at depth interval 10057.5 feet/3065.53 meter indicates the presence of cross stratification which matches with the automated image log classification. The next sinusoid picking was done at 10061 feet/3066.59 meter, 10062 feet/3066.90meter and 10064-10065 feet/3067.51-3067.81 meters all of which correspond to the automated image log classification, followed by a thin horizontal stratification at 10066 feet/3068.12 meter leading to cross stratification and then to horizontal stratification. The cross stratification followed by horizontal stratification at interval 10070 feet/3069.34 meter and 10072 feet/3069.95 meter also shows a clear match. There is a mismatch in the dip estimation at 10075 feet/3070.86 meter when compared to the automated classification. However, the cross stratification identified at the central regions of the image log can be taken as a match to the dip estimation from the sinusoid fitting or can be used as a reference to reanalyze the image log. This is again followed

by a clear one to one match of the cross stratification and horizontal stratification defined by both automated image classification using OBIA and manual image log interpretation based on dip estimation by interactive sinusoid picking from the image log. Both dip estimates and automated classification showed the presence of cross stratification at intervals 10083 feet/3073.30 meter, 10085feet/3073.91 meter and 10087 feet/3074.52 meter followed by the horizontal stratification at 10088 feet/3074.82 meter. Thus we could see an acceptable match between cross stratification (angle above 10^{o}) and horizontal stratification identified by the automated method and by the manual sinusoid picking and interpretation.

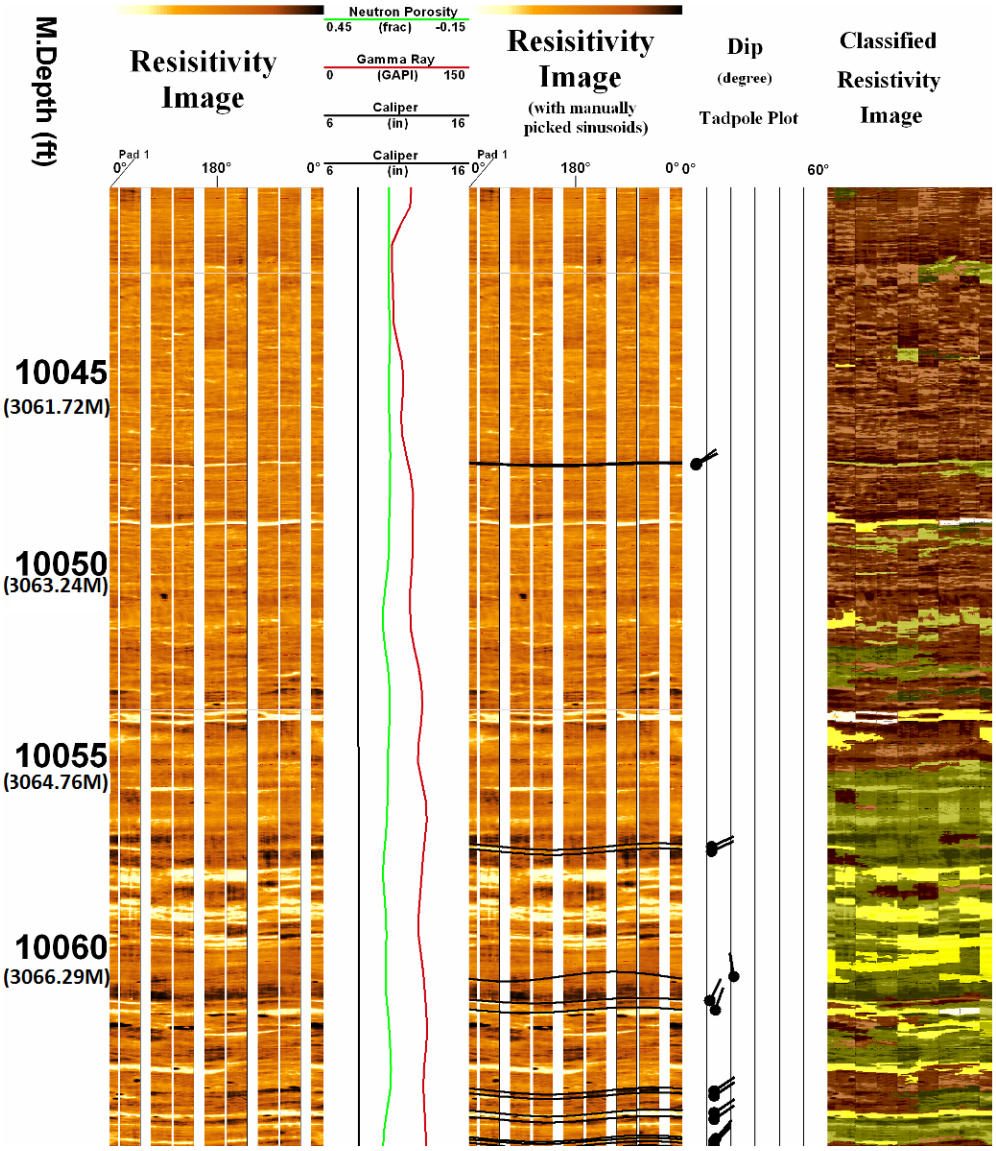

Figure 6. 7*: Automated image log classification: From left to right: depth, standard logs- caliper, gamma and neutron logs, Image log with manually picked sinusoids, dip measurements obtained from manually picked sinusoids, classified image log. Dip measurements that are below 10 are considered as horizontal stratification and above 10 as cross stratification. Image log is classified into bioturbated zone, cross stratification, horizontal stratification, and unclassified region (white). (The figure is plotted at 1:30 scale so that an easy comparison of the results can be done).*

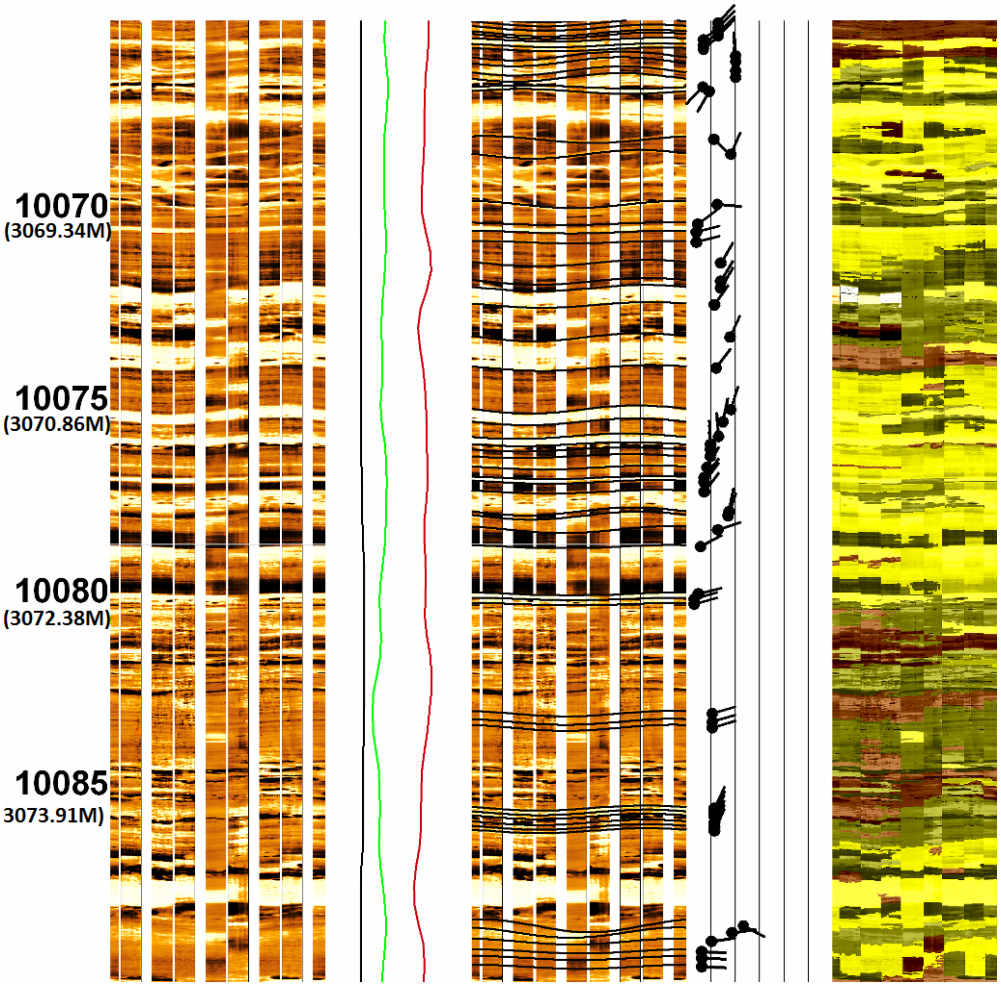

(Figure 6.7 contd. from previous page)

However figure 6.7 shows a few image objects being marked as unclassified regions (shown in white color). The main parameter used to train the classifier was the textural feature - homogeneity, and the histogram plot of homogeneity shown earlier in this chapter (figure 6.5) clearly indicates the presence of image objects that fall beyond the feature range defined for each lithofacies class that was used to train the classifier.

We know that most rocks are resistive and it is the enclosed fluids (except hydrocarbon) that make them conductive. However, carbonate cementation are relatively non-porous and non-permeable. Hence, they have high resistivity and are denoted by light and mostly white color in an image log. The unclassified regions in figure 6.7 resemble areas belonging to carbonate cementation and so they are classified as carbonate cements.

Hence, the feature range defined for the classification was refined and the new feature space created from three textural features – homogeneity at 90^{o}, 45^{o} and average contrast to classify the uncertain regions as carbonate cements is shown in figure 6.8. The feature space shows a clear separation of image objects into four classes – bioturbation, horizontal stratification, cross stratification and carbonate cements. The resultant classification based on this revised feature distribution is shown in figure 6.9.

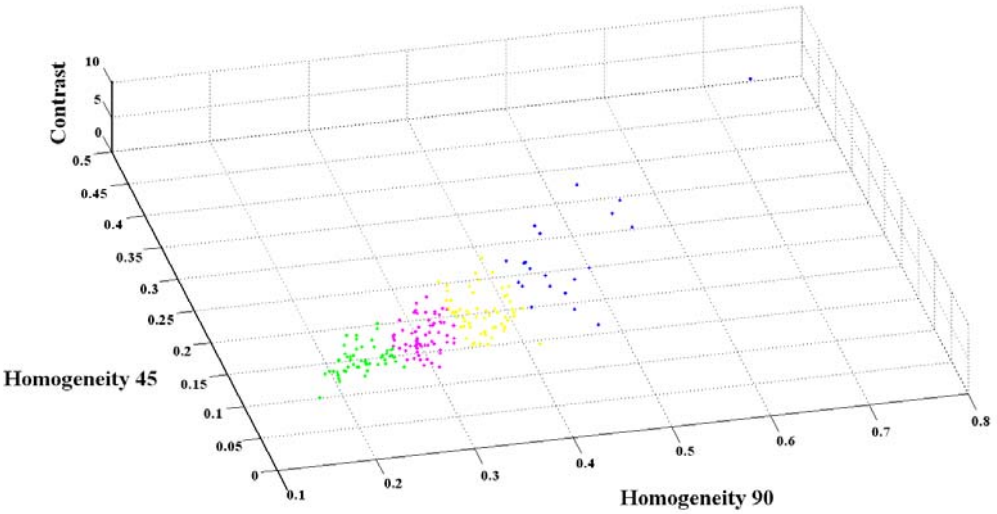

Figure 6. 8*: Cross plot of textural features showing a clear separation of image objects belonging to bioturbation (green), cross stratification (purple), horizontally stratification (yellow) and carbonate-cements (blue).*

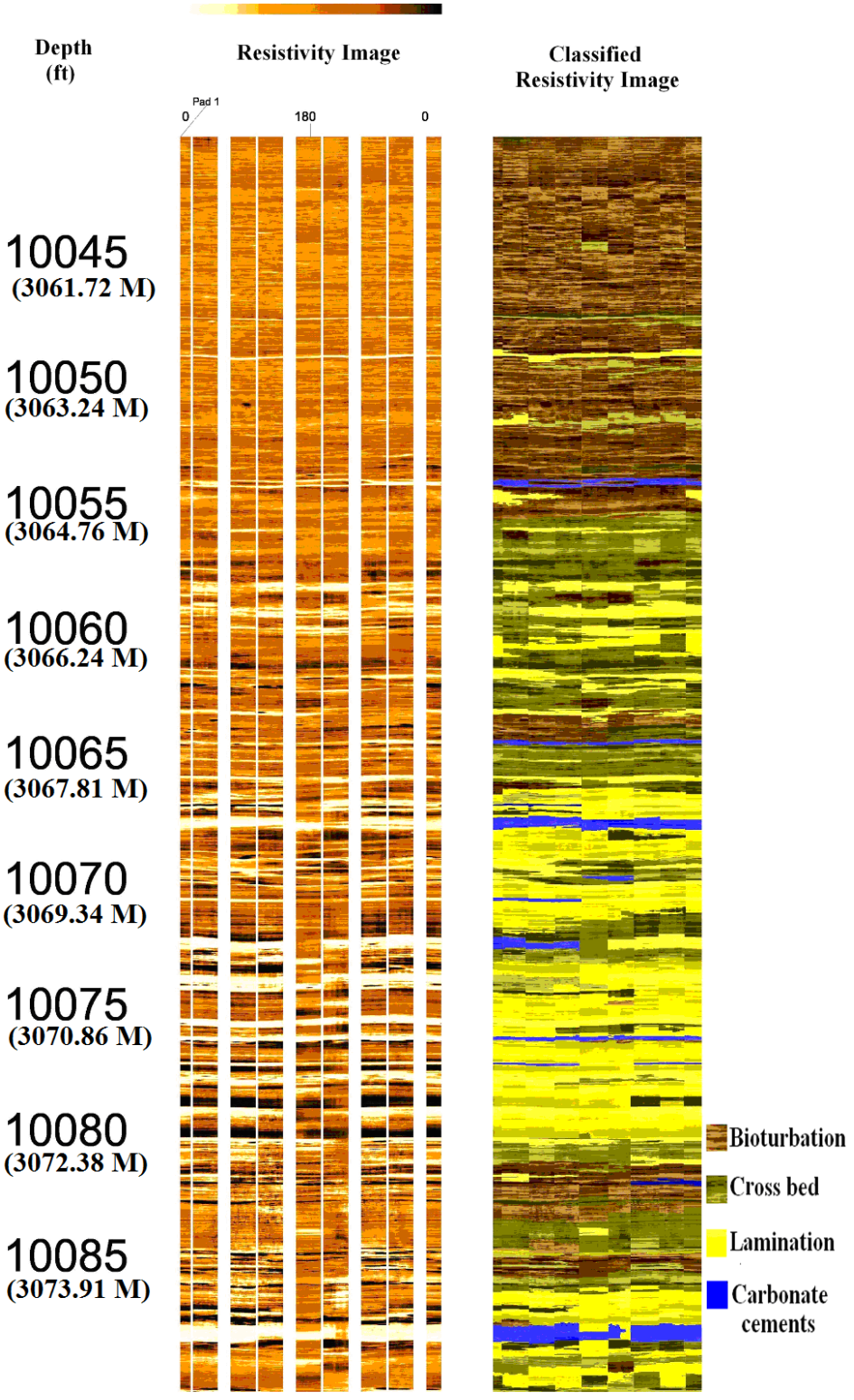

Figure 6. 9 *: Automated image log classification. From left to right: depth in feet, image log used for the study, and the classified image log. Image classification key is given to the right of the figure.*

In this study, as physical cores were not easily readily available, we have not done any core examination and the lithofacies inferences were made entirely from core photograph. A detailed examination of core photograph does not indicate the presence of any carbonate cementation in these regions. According to Prosser et al., (1999) there can be conflicts in interpretation when we calibrate lithofacies interpretation from image log with core because image logs survey a larger surface area of the borehole compared to the slabbed core surface which may result in instances where image logs provide greater insight into the presence of cementation when compared to core

An important aspect that stands out from this automated image analysis methodology is that any image regions that are beyond the defined feature range in the classification scheme will remain unclassified. It allows the interpreter to go back and reanalyze the image. Hence the classification does not totally depend on the experience and expertise of the image interpreter but is dependant on the properties encrypted on the image log. This is an added advantage offered by this classification method.

Similarly, if the image log contains artifacts; it can be classified into another class say, artifacts. Most of the artifacts appear as black colored regions in an image log. Hence, the image log regions belong to the artifacts could be easily classified based on features related to color.

6.4 RESULTS

The automated image log classification obtained using the object based image analysis is compared with the ground truth which is the geologist's interpretation based on core photograph in this study. As the core photograph did not indicate the presence of carbonate cement in the study area the

unclassified region has been retained and was not converted into carbonate-cements. The automated image log classification along with the geologist's interpretation based on core photograph and standard logs is given in figure 6.10.

Both classifications showed the presence of bioturbation (an example of the core photograph from this region is shown in figure 6.11 (a)) in the interval 10040-10053 feet/3060.19-3064.15 meters while the automated classification picked up a few thin horizontal and cross stratification in between. The core photograph was not showing a clear picture of the formation at intervals 10054-10056 feet/3064.46-3065.07 meters (an example of the core photograph from this region is shown in figure 6.11 (b)) which according to the image log classification is bioturbation followed by cross stratification. It is assumed to be true since the classification showed a close match with the following cross stratification region up to 10057 feet/3065.37 meter (core photograph is given in figure 6.11 (c)). The horizontal stratification in the next interval according to the core photograph was not identified from the image log. Bioturbation in the following interval was slightly identified, though there was a considerable mismatch in its thickness when compared to the ground truth.

In 10058 - 10059 feet/3065.68-3065.98 meters, the majority of the image objects were classified into the same class defined by the core photograph with a few thin traces of planar laminations according to the image object's textural property. The no-core region at interval 10061-10063 feet/3066.59-3067.20 meters was marked as those belonging to cross stratification.

The bioturbation at 10064 feet/3067.51 meter was clearly marked by both the classification. This is followed by a good match between both classifications up to 10071feet/3069.64 meter; horizontal stratification followed by the dipping stratification (figure 6.11 (d)) leading to horizontally stratification. The following two bioturbations at 10072.5 feet/3070.10 meter and 10073.5

feet/3070.40 meter were not classified and were marked as cross stratification from the image log. However the cross stratification in between these bioturbation intervals marked by the geologist was clearly classified from the image log. The automated classification showed a thicker bed compared to the geologist's interpretation. It happens when the textural property of the two beds are too close to classify and hence both were classified into the cross stratification which made the mismatch in bed thickness. This interval is followed by horizontal stratification identified from both classifications and the core photograph corresponding to this is shown in figure 6.11 (e).

The bioturbation at 10076-10077 feet/3071.16-3071.47 meters was not clearly detected from image log except a very thin image object being marked as the same in the middle region of the classified image. This conflict in interpretation may be due to the differences in the resolution scales of the image tool (mm-cm scale) and parameters which may be visually determined from core (mm scale) (Prosser et al., 1999).

At 10082 feet/3072.99 meter, core photograph showed the presence of bioturbation followed by totally disoriented cross stratification as shown in figure 6.11 (f). This has been identified as bioturbated zone due to the resultant less homogeneity textural feature from the image log. The qualitative visual interpretation of the image log also shows the resemblance of this region to that of a bioturbated zone.

This region is followed by cross stratification according to both the classifications. The uncertain region defined by the geologist at interval 10084 feet/3073.60 meter due to the unclear core photograph is being identified as cross stratification in the automated image log classification. This is followed by good match of the bioturbation and cross stratification by both classifications. The following uncertain region at 10087 feet/3074.52 meter which according to the geologist may belong to cross stratification (as

indicated with discontinuous dipping lines) was marked as horizontal stratification in the image classification. The conflict in the result may be due to the fact that sometimes the recovered cores are not properly oriented (Gaillot et al., 2007).

This is followed by an unclassified region in the automated method which corresponds to slump according to the core photograph interpretation. In the following depth interval horizontal stratification is identified in both classifications. But, a few image objects are grouped as cross stratification where core photo is absent and hence cannot make a one to one comparison.

Now, out of the regions defined as cross stratification, majority is hummocky cross stratification which are in fact tilted horizontal stratification formed all on a sudden due to a storm or current and cross stratification which are being deposited on a long run. Both these types of cross stratification leave sinusoidal patterns (explained in chapter 7) in an image log hence, not able to distinguish from image log alone. Hence both are classified into the same class, cross stratification, as explained in the beginning of this chapter.

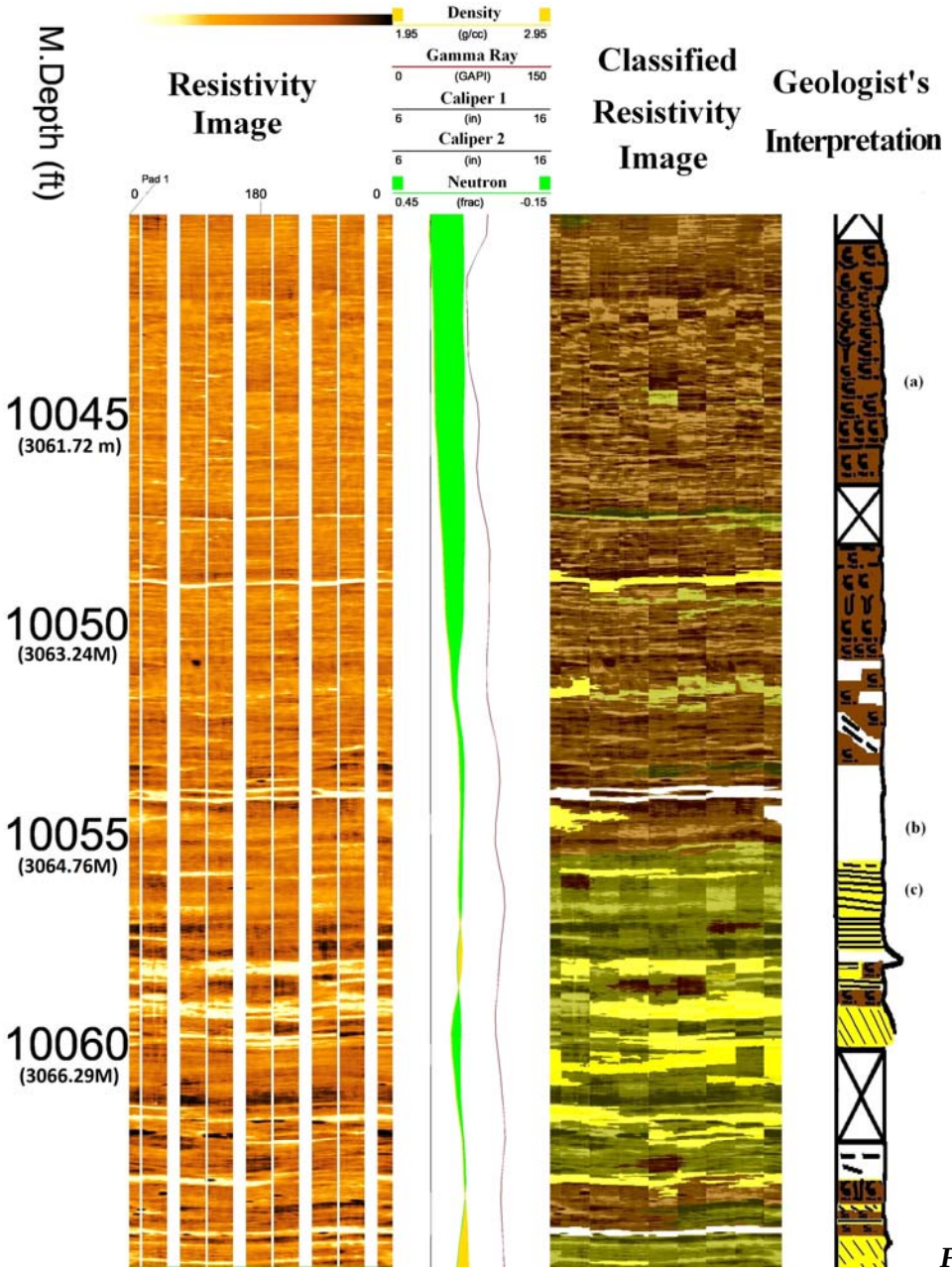

Figure 6. 10*: Automated image log classification: From left to right: depth interval, image log, standard logs- caliper, gamma, density and neutron logs, classified image log using developed methodology, and the geologist's interpretation based on core photograph. Image log classification key is same as in figure 6.10. (The figure is plotted at 1:30 scale so that an easy comparison of the results can be done). Core photographs corresponding to the marked regions (right of the figure) are shown in figure 6.11.*

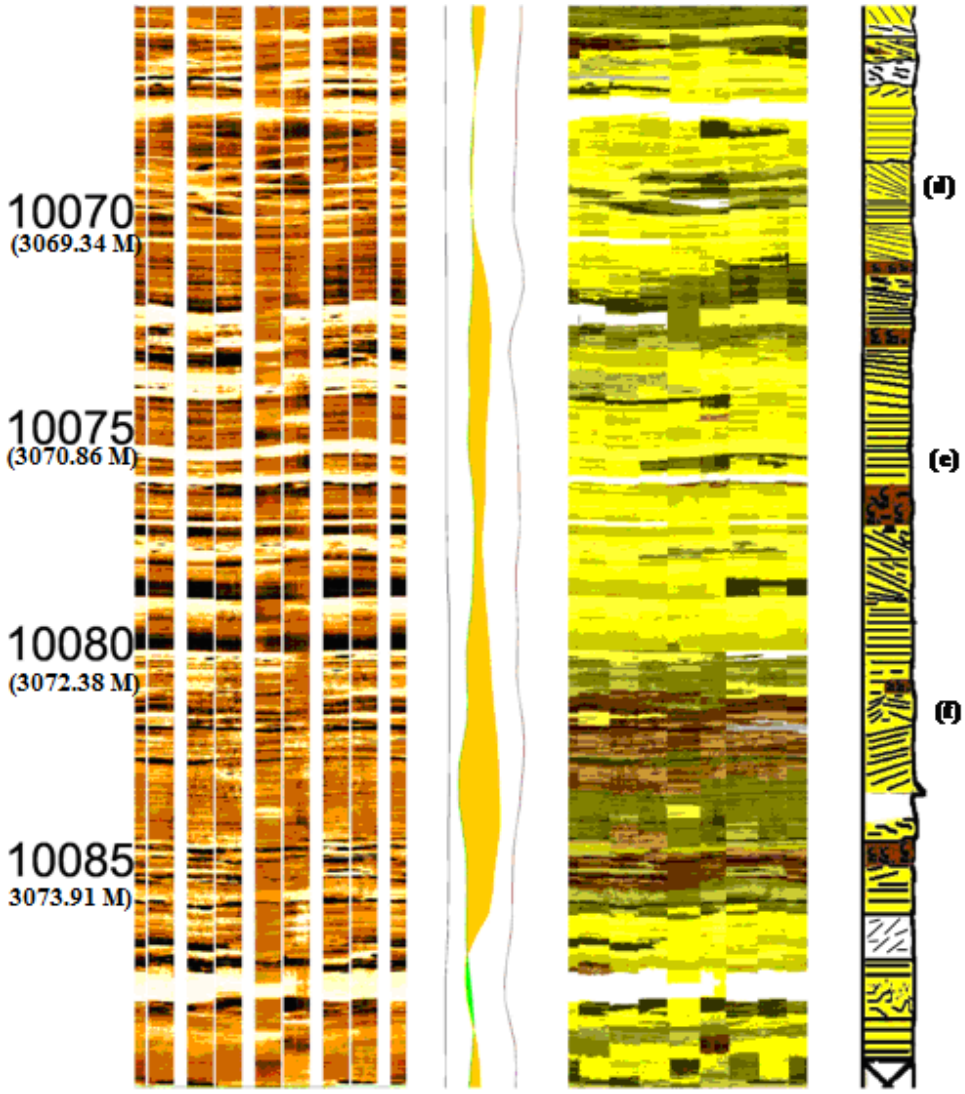

(Figure 6.10 contd. from previous page)

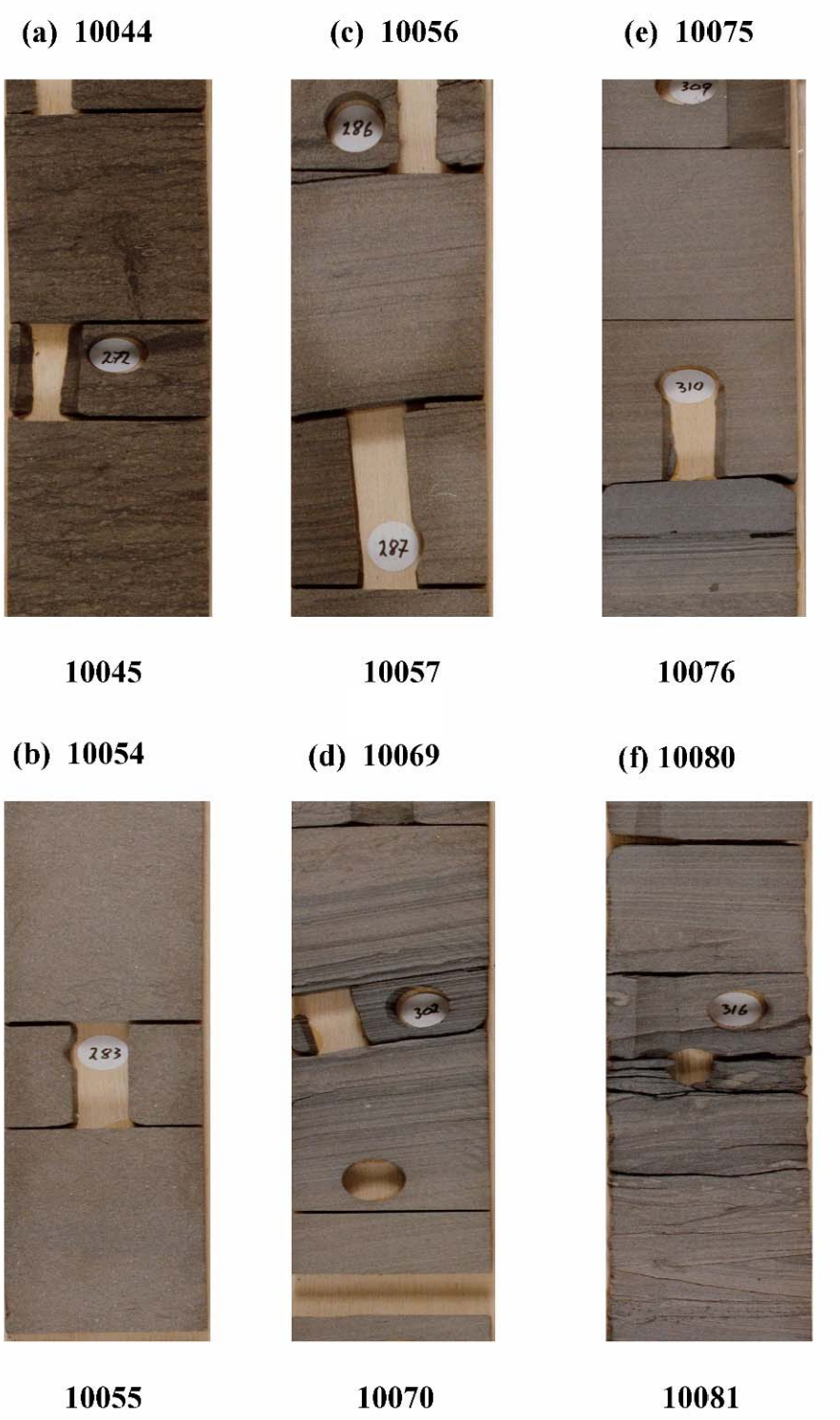

Figure 6. 11*: Core photographs corresponding to the marked regions in figure 6.10. All depths are given in feet. Core photographs correspond to (a) bioturbation (silty sand), (b) uncertain region, (c) cross stratification, (d) Hummocky cross stratification, (e) horizontal stratification, and (f) disoriented sandstone.*

6.5 DISCUSSION

6.5.1 Accuracy Assessment of the classification

An interactive one to one comparison of the result obtained by the automated method is made with the geologist's interpretation entirely based on core photograph. This is done by comparing the results in a sliding window of every 0.2 feet.

According to the automated interpretation, out of the 251 window samples in the tested interval from 10040 to 10090 feet/3060.19 to 3075.43 meter, 95 samples belonged to bioturbation; 88 samples belonged to cross stratification 60 belonged to horizontally stratification; and 8 samples belong to unclassified region. According to the geologist's interpretation of the same interval, out of the 251 samples, 77 samples belonged to bioturbation; 71 cross stratification; 43 horizontally stratification; 22 samples belonged to regions where core was absent hence the core photo was not available (non-colour coded regions which are marked with 'X' in the geologist interpretation shown in fig 6.10); 38 samples where the core photo was vague or does not show any clear feature to definitely classify into any regions, hence marked as uncertain regions (the non-colour coded regions other than that belonged to no-core regions in figure 6.10, the dashed or non continuous lines in this region represent the probable classes for these regions according to the geologist). This classification result is summarised in the histogram plot shown in figure 6.12.

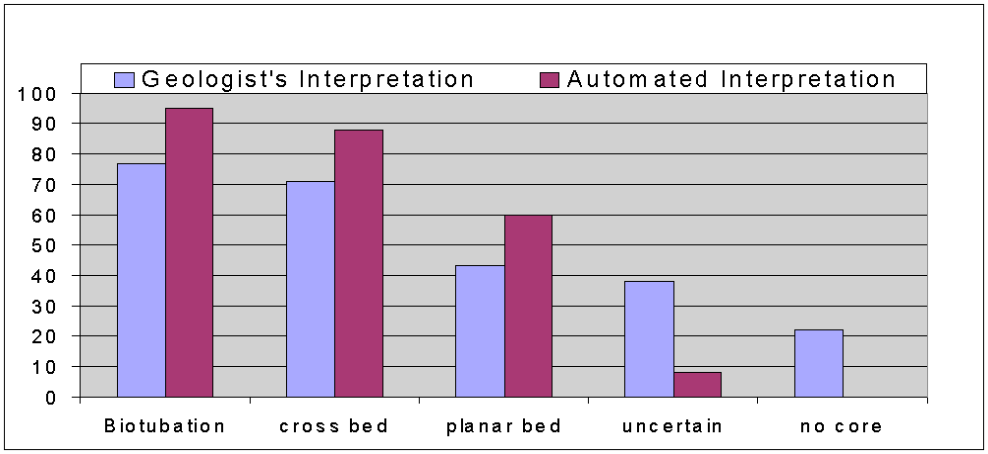

***Figure 6. 12**: Histogram comparing the classification results by a geologist based on core photographs, and the automated interpretation based on the image log.*

An accuracy assessment of the result was obtained by doing a one to one comparison of the classification result from the automated method with that of the geologist's interpretation, using the data summarised above. For this, the image log classification corresponding to the no-core regions and uncertain regions defined by geologist have been excluded. The result is summarised in table 1. The result shows that out of the remaining 191 samples, 5 were unclassified regions from the image log. Out of the other 186 samples 157 were classified correctly, giving an overall accuracy of 84.41%.

Automated Classification \ Geologist's Interpretation	Bioturbation	Cross bed	Planar Lamination	Unclassified
Bioturbation	69	6	2	-
Cross Bed	5	54	6	-
Planar Lamination	2	8	34	-
Unclassified	1	3	1	0

Table 6.1*: Accuracy assessment of the automated classification is done by comparing the classification result with geologist's interpretation.*

6.5.2 A comparison of Object-based and Pixel-based image analysis results:

Chapter 3 presented the lithofacies classification of the same image log using the pixel-based image analysis technique. A comparison of the classification achieved by both methods is given in figure 6.13 along with the geologist's interpretation based on core photograph. The object-based image analysis has not only improved the classification but also resulted in much more realistic bed boundary identification. In pixel-based image analysis, features are calculated as a one dimensional curve as a function of depth. But, evaluation of average image properties for each depth masks the real geological heterogeneity. This study demonstrates that, analyzing image properties at image-object level solves this problem as the image properties in two dimensions- as a function of borehole depth and circumference, are utilized. Hence, the spatial characteristics inherent within the image are preserved in the classification result. The pixel-based image analysis may also fail in detection of fine heterogeneities since an average image property in a defined window is calculated and depth related. For example, the thin bed of

bioturbation between 10065 and 10067 feet/3067.81 and 3068.42 meter is not identified in pixel-based method whereas it is identified accurately in object based method. Moreover the accuracy assessments show that the pixel-based method yields 76.79% accuracy, while the object based method yields a much better accuracy of 84.41%

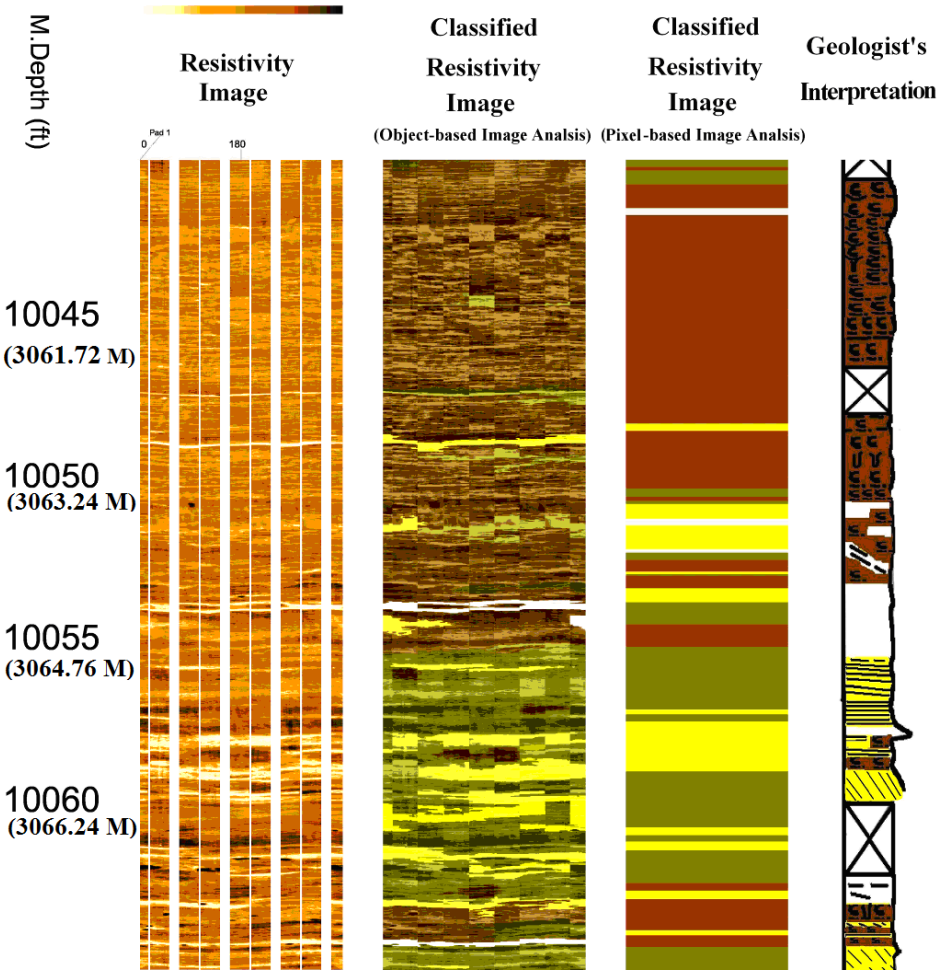

Figure 6. 13*: A comparison of automated image log classification obtained using object-based image analysis and pixel-based image analysis: From left to right: depth interval, image log, classified image log using object-based image analysis, classified image log using pixel-based image analysis, and the geologist's interpretation based on core photograph. Image log classification key is same as in figure 6.10, and for pixel-based image classification brown color indicates bioturbation, yellow horizontal stratification, and dark green cross stratification. (The figure is plotted at 1:30 scale so that an easy comparison of the results can be done).*

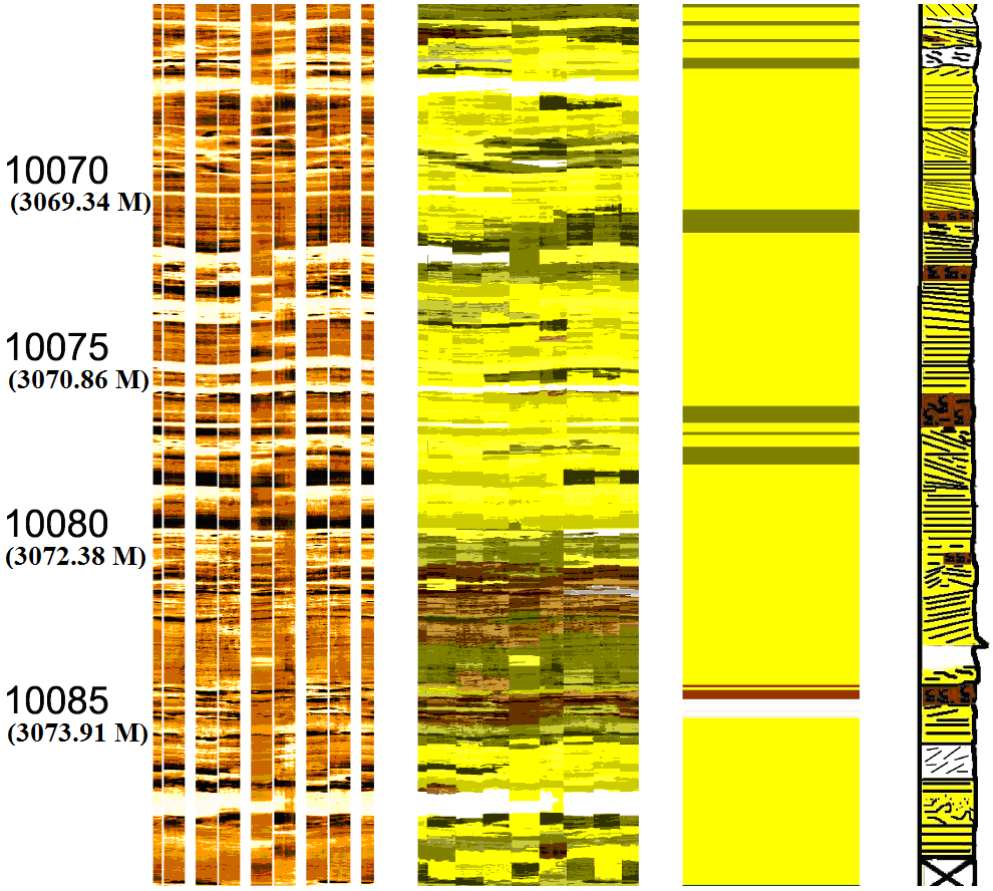

(Figure 6. 13 contd, from previous page)

6.6 CONCLUSIONS

A successful simplification of the interactive, labor intensive visual image log interpretation has been achieved using the object based image analysis methodology as shown in this chapter. The classification result when compared to interactive manual image log interpretation and with the core photograph interpretation showed a reasonably good and comparable result. Hence one can conclude that we have developed an effective automated image log interpretation methodology which can be used on any large quantity of data.

There may be times when image log is not providing enough information to stand alone. In such kind of situations all extracted data, standard log, image log, core, and core analysis compliment each other and a proper compilation of these data may lead to a successful extraction of subsurface details. This is shown in detail in the next chapter – a successful compilation of standard logs and image log derived logs with image log for a meaningful image log classification from a ‘difficult’ data set.

Chapter 7

AUTOMATED LITHOFACIES EXTRACTION FROM ELECTRICAL BOREHOLE IMAGES – AN INTERPRETATION OF 'DIFFICULT' DATA SET FROM A DEVIATED WELL

Summary: Chapter 6 discussed how an Object-based Image Analysis methodology can be used for an effective lithofacies classification from an image log. In this chapter, the methodology is applied to interpret a 'difficult' image log data from a deviated well (section 7.1). For a successful lithofacies classification from this data set, the methodology is extended (section 7.2) to incorporate the wealth of information from standard logs and image-derived logs. The lithofacies classification protocol is refined to incorporate the new developments and is tested in an image log interval (section 7.3). The good match of the automated classification result with that of geologist's qualitative interpretation based on core photograph gave the confidence to apply the protocol on another image log interval. The accuracy of the automated image log classification is assessed by performing a one to one comparison with the geologist's interpretation and the chapter is concluded in section 7.4.

7.1 INTRODUCTION

The automated lithofacies identification method from image logs proposed in chapter 6 has been extended to integrate standard logs and image-derived logs with the image logs for a successful lithofacies identification from 'difficult' data sets. Image log from a deviated well, South Batra 20 (discussed in chapter 5) has been used for this study. The data set is considered 'difficult' as the image log does not show a clear distinction between every conductive and resistive region, while the standard logs and core photographs do so. Hence the valuable information from standard logs are incorporated into the Object-based image analysis methodology along with image log to mark bed boundaries. Taking account of the well

deviation, bed orientations are calculated using automated sinusoid fitting at every pixel depth in the image log within a formal uncertainty framework, and are used with image logs to differentiate horizontally stratified beds from dipping beds. Thus, the high resolution information (in terms of borehole coverage and sampling rate) contained in the image log is used successfully in spite of the poor resolution between every conductive and resistive region. The inclusion of expertise of a geologist in this methodology as discussed in previous chapters ensures the adaptation of the methodology to suit each field and data necessities. This is necessary because each field is unique in itself and there are local factors that may affect the data in unexpected ways. The resultant lithofacies classification is then validated through the interpretation of cored intervals by a geologist. This calibration and comparison ensures the accuracy of the results obtained and gives confidence in the extrapolation of results from depths with core control to intervals with poor or no core recovery.

7. 2 METHODOLOGY

The image log is pre-processed as explained in chapter 3 and is then correlated with cores and other geophysical logs to summarise the borehole image features of all lithofacies present in the formation. A detailed image-log-core depth matching (chapter 3) is performed taking image log as the reference.

Core examination revealed the presence of four main classes in the well, cross bedded sandstone, planar laminated sandstone, carbonate cement and shale. A representative depth interval is chosen that contains all these four classes for the initial protocol (chapters 2 and 5) development and

testing (figure 7.1), and a random image interval is chosen for further testing and validation of the protocol.

Generally, image logs provide fine details of the formation (as shown in chapter 6). However, sometimes they do not give geophysical responses which are immediately diagnostic of lithofacies present in the subsurface (Rider et al., 1999). For example, in dynamically normalized images (Serra, 1989) (color ranges are limited to short vertical intervals of typically 2m-10m), the electrical response of a laminated sandstone can be very similar to the electrical response of a laminated shale and tend to be not lithologically diagnostic. In such cases the standard logs can be used to refine the image log classification.

The data used in this study (the data set is same as that used in chapter 5 for automated lithology extraction from core photograph) is an example of such case as it failed to show any prominent difference between sand and shale within some intervals. An example is given in figure 7.2 where the top image section, figure 7.2(a), clearly discriminates sand and shale while the bottom image section, figure 7.2(b), display no clear distinction between sand and shale. The lack of discrimination may lead to false bed interpretation.

The deviation of the well, in the cored depth interval used in this study, was approximately 20 degrees. Due to this deviation of the well; planar bedding also appears to be dipping in image log and core photograph. The dipping bed and planar bed classes can be categorised taking into account of the deviation of the well.

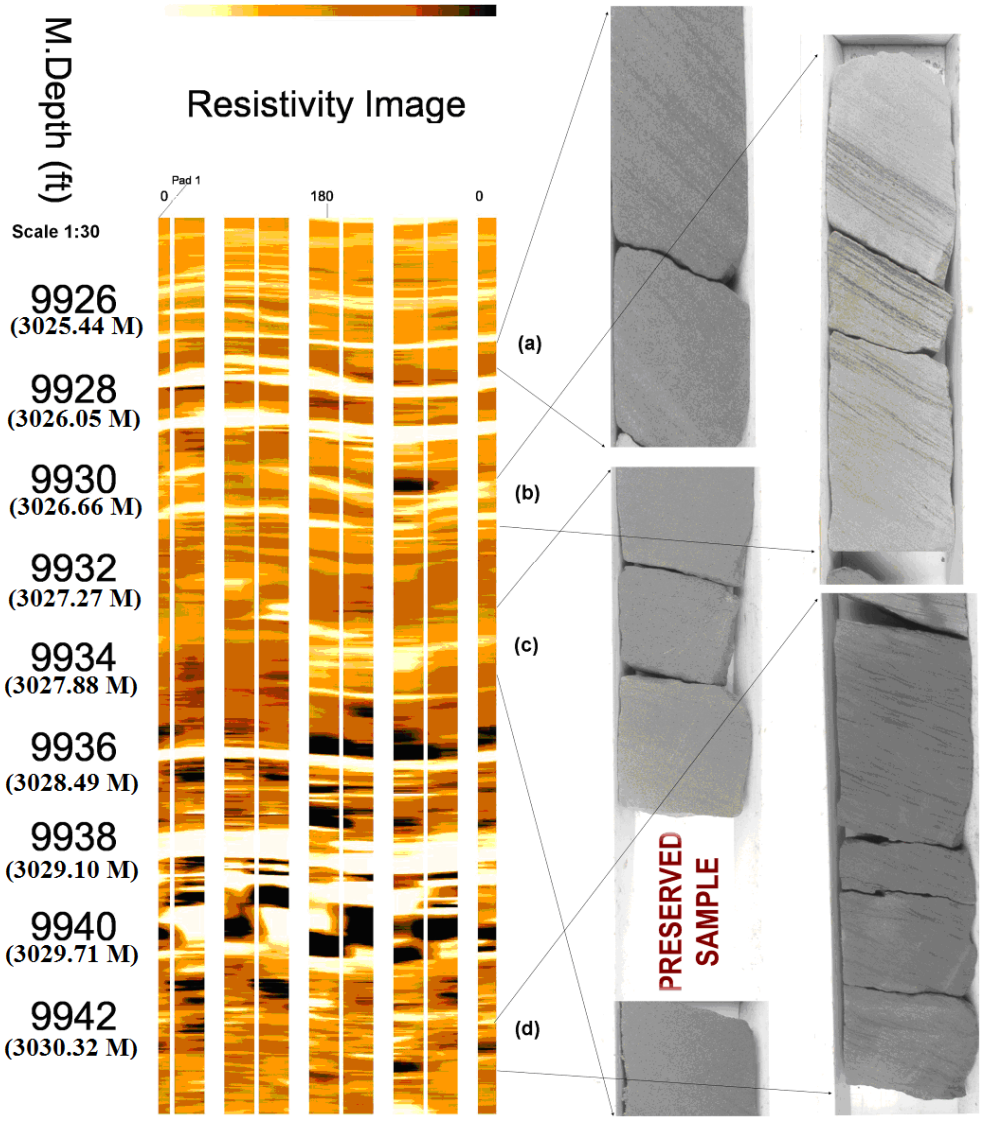

Figure 7.1*: The interval of the resistivity image chosen for classifier training and protocol development. The interval consists of four classes (a) cross bedded sandstone, (b) carbonate cementation, (c) horizontally-stratified sandstone, and (d) shale, each shown with the corresponding core photographs. Due to the deviation of the well, planar bedding also appears to be dipping. The dipping bed and planar bed classes are categorised taking into account the deviation of the well.*

Hence, to enable better lithofacies detection from image logs, we further process the log data in advance of applying the classification methodology. Specifically we create two filters, based on logs, which provide the following information:

1. Sand- shale filter created from Neutron Density Separation to mark sand and shale bed boundaries and,
2. Dip estimation from the image log using uncertainty-based sinusoid fitting to identify horizontally stratified beds and dipping beds.

The creations of each of these filters are explained below.

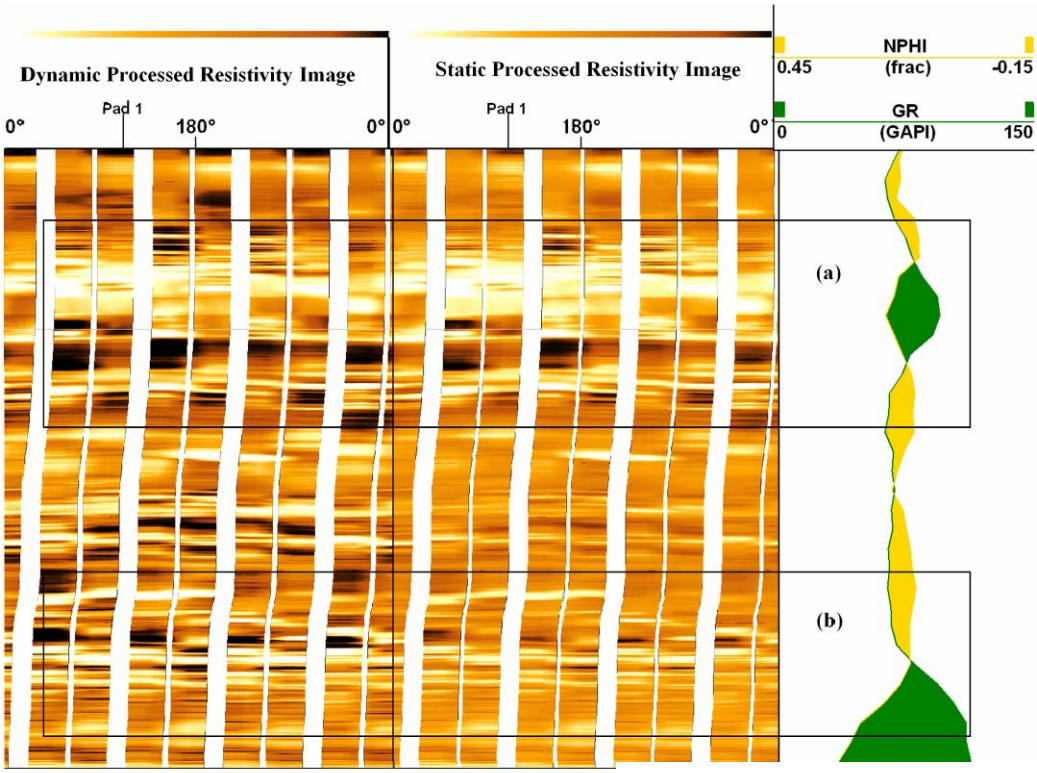

Figure 7.2*: Image log (left) showing (a) clear sand shale distinction, and (b) no obvious distinction between sand and shale. On the other hand, the standard gamma log and neutron log show a clear distinction between the sand (yellow shaded region) and shale (green shaded region) in both (a) and (b)(right).*

7.2.1 Filter 1; Neutron Density separation

Standard logs especially the neutron and density logs discriminate the difference between sand and shale in a robust manner. Hence, this information is used to constrain the image segmentation in such a way that adjacent, similar pixels are grouped into objects in each sand or shale unit separately; that is any object can not cross a sand-shale boundary. In the data set used, the separation between neutron and density logs showed a clear distinction between sand and shale sections. So both neutron and density logs are converted into a compatible scale (limestone porosity units, PU, say). The separation between them is then related to lithology. A method from Gupta and Johnson (2001) is used for this purpose. The theoretical limit that is used for the conversion of the density log from g/cm^{-3} to PU is given in Table 7.1. Using these equivalent values the density log is quantified in PU, and the resulting neutron-density separation curve is calculated. The new curve produced is named *NDSEP (Neutron-Density Separation)*,

$$NDSEP = N_{\varphi} - D_{\varphi} \tag{7.1}$$

where N_{φ} is the neutron porosity and D_{φ} is the density porosity, both in PU. The curve tends to produce a small or negative value in sand horizons and a larger, positive value in shale sections.

Neutron density separation – the density log can be scaled in neutron porosity units where: 0pu ≡ $2.7gcm^{-3}$ (equivalent to a log value representing 100% carbonate) 100pu ≡ $1gcm^{-3}$ (equivalent to a log value representing pure fresh water)

Table 7.1*: Theoretical limits for the calculation of neutron density separation*

7.2.2 Filter 2; Dip estimation

As an image log is presented as an unrolled view of the borehole, any non-horizontal, planar bed in the formation appears to have a sinusoidal shape in the image (figure 7.3). The data used in this study are from a deviated well, so the entire formation appears to be dipping relative to the well due to the well inclination. Hence, to distinguish horizontally-stratified beds from cross-beds, an algorithm is developed to automatically select the set of best fitting sinusoids at each pixel depth and to calculate the bed orientations from these sinusoids. The deviation of the well is subtracted from the obtained dips at each depth, and hence we calculate the actual orientation of each horizon.

Various automated dip analysis methods have been proposed in literature (Antoine, 1990; Rabiller et al., 1997; Torres et al., 1990; Ye et al., 2001; Ye, 1995). However, the proposed method is different from these because here the best fitting sinusoids are obtained within a formal uncertainty limit, at every pixel depth in the image log. As we calculate the best fitting sinusoids at every depth rather than one in a predefined window, it is easy to distinguish fractures from bed orientations. This is because the stratification planes are generally seen in groups, while fractures are seen as single anomalous sinusoids at specific depths. Hence any anomalous events either in the continuous record of the dip angle measurement that is obtained or in the best-fitting sinusoid, could be cross checked to see whether it indicates the presence of a fracture.

The proposed methodology is based on the pixel intensities in the image, finding a continuous sinusoidal path that runs through the image from left to right at each depth. The best fitting sinusoids are those along which the pixel intensities are most similar. Hence this methodology is not sensitive

to occurrences of vacuoles, nodules or vugs (as they will show local contrast in the spectral values), which is another important advantage for the geological interpretation of the dip trends.

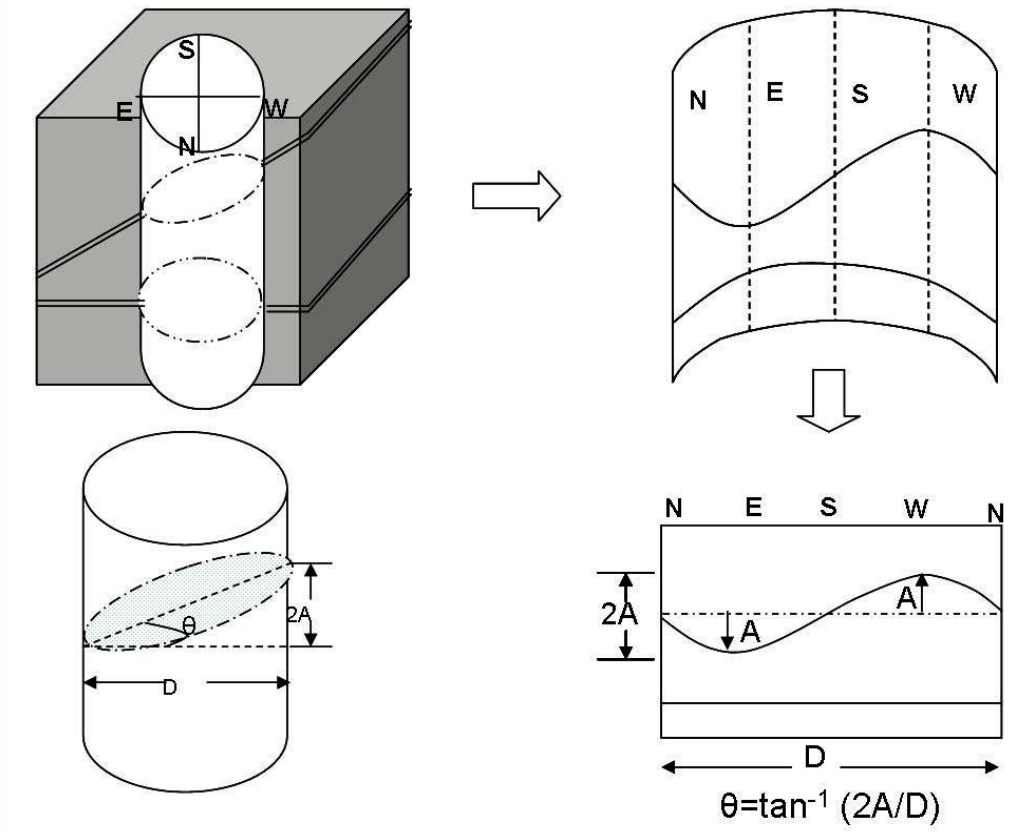

***Figure 7.3**: Illustration of sinusoid formation and dip calculation. The image derived from the cylindrical borehole (top left) and its presentation on a flat surface as an unrolled view of the borehole (top right); any non- horizontal bed in the formation appears to have a sinusoidal shape in the image. From this sinusoid we could calculate the angle at which the bed is dipping as illustrated (bottom left and right).*

All possible sine curves passing through the same depth point, *Z,* are given by,

$$Y = Z + A[\sin(\theta - \phi) + \sin\phi] \tag{7.2}$$

Here A is the amplitude of the sinusoid, θ is the azimuth and ϕ is the phase. Figure 7.4 shows sine curves of different phases and amplitudes passing through the same depth point. A set of many possible sinusoids similar to 7.4 (c) are calculated at each depth in the well, and the gray scale values, g_i: i=1,.,N, corresponding to N pixels on each sinusoid are determined from the image log. The average value, and the standard deviation, σ, of the values along each sinusoidal path are calculated as,

$$\mu = \sum_{i=1}^{N} \frac{g_i}{N} \tag{7.3}$$

and

$$\sigma = \sqrt{\sum_{i=1}^{N} ([\mu - g_i]^2)} \tag{7.4}$$

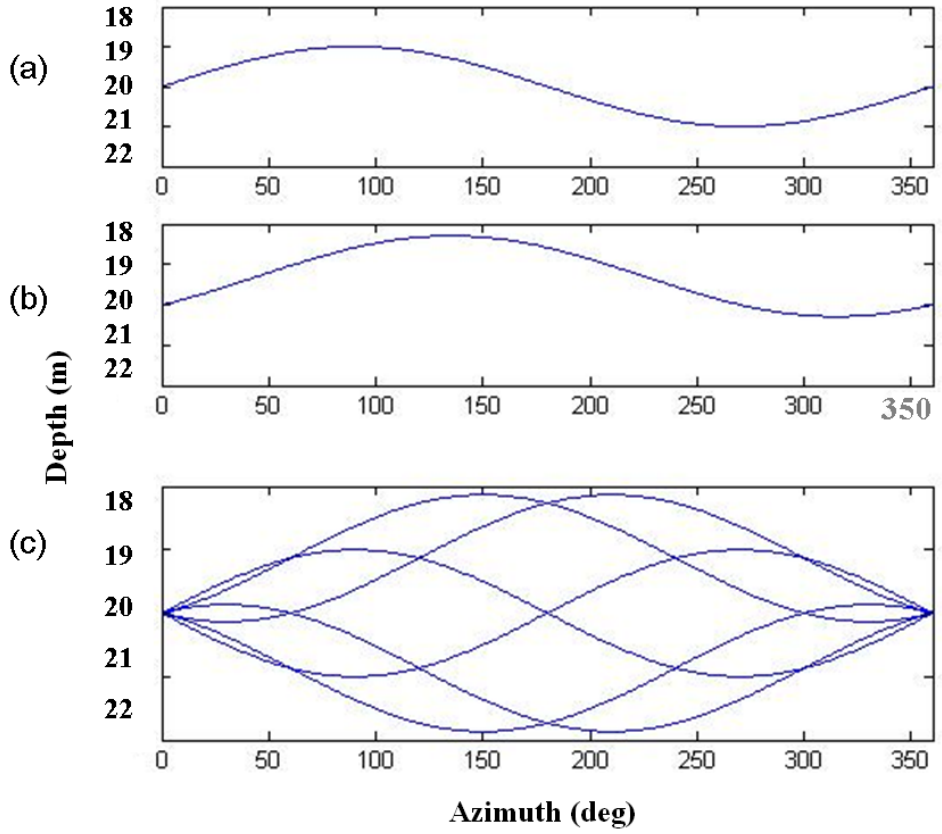

Figure 7. 4*: Illustration of the sine equation 3 with Z=20 and A=1 (a) When the phase ϕ =0 (b) When ϕ =45 (Note that the depth point is constrained to 20 at azimuth zero). (c) Sine curves of different phases and amplitudes passing through the same depth point.*

This standard deviation is normalized by the average grayscale value along the sinusoid so that the standard deviation of intensities should not be dominated by background intensity variations from depth to depth. The normalized standard deviation, χ , is therefore

$$\chi = \frac{\sigma}{\mu} \tag{7.5}$$

The minimum χ value, say "Normalized minimum Standard deviation Criteria", NSC, provides us with the best fitting sinusoid at that depth and if D is the diameter of the well (can be obtained from the caliper logs), then the dip is given by

$$\text{Dip} = \tan^{-1}\left[\frac{(2A)}{D}\right] \tag{7.6}$$

Figure 7.5 shows an example of the best fitting sinusoid calculated at each depth using this methodology, along with the corresponding dip values (blue line). An image log with manually picked sinusoids is also given in the same figure; we can see a good match between the automated sinusoid fits with the manually picked sinusoids. Also the algorithm picked sinusoids at every depth even in intervals where it was difficult to pick sinusoids manually.

Since the data themselves are uncertain to some extent, all curves that have *NSC* values close to that minimum value are potential dipping planes since they are also consistent with the data. Hence an uncertainty limit up to which the *NSC* can vary is introduced, within acceptable limits *NSC + 5%* in this study. From the so obtained set of all possible sinusoids, a range of possible dips or structures are calculated for each depth. The red dotted line in the *NSC* plot of Figure 7.5 shows the limit up to which *NSC* is allowed to vary, and the red dots in the dip plot show all possible dip values that can occur when *NSC* is allowed to vary up to the introduced uncertainty limit. Based on the resulting set of dips at each depth and on the deviation of the well, a filter is created to distinguish cross-beds from planar lamination; all dips that are approximately equal to the well deviation (the shaded region in the dip plot) are taken as planar

lamination, the rest are taken as dipping beds and those depths were the dip fall in both the criteria are defined as uncertain regions.

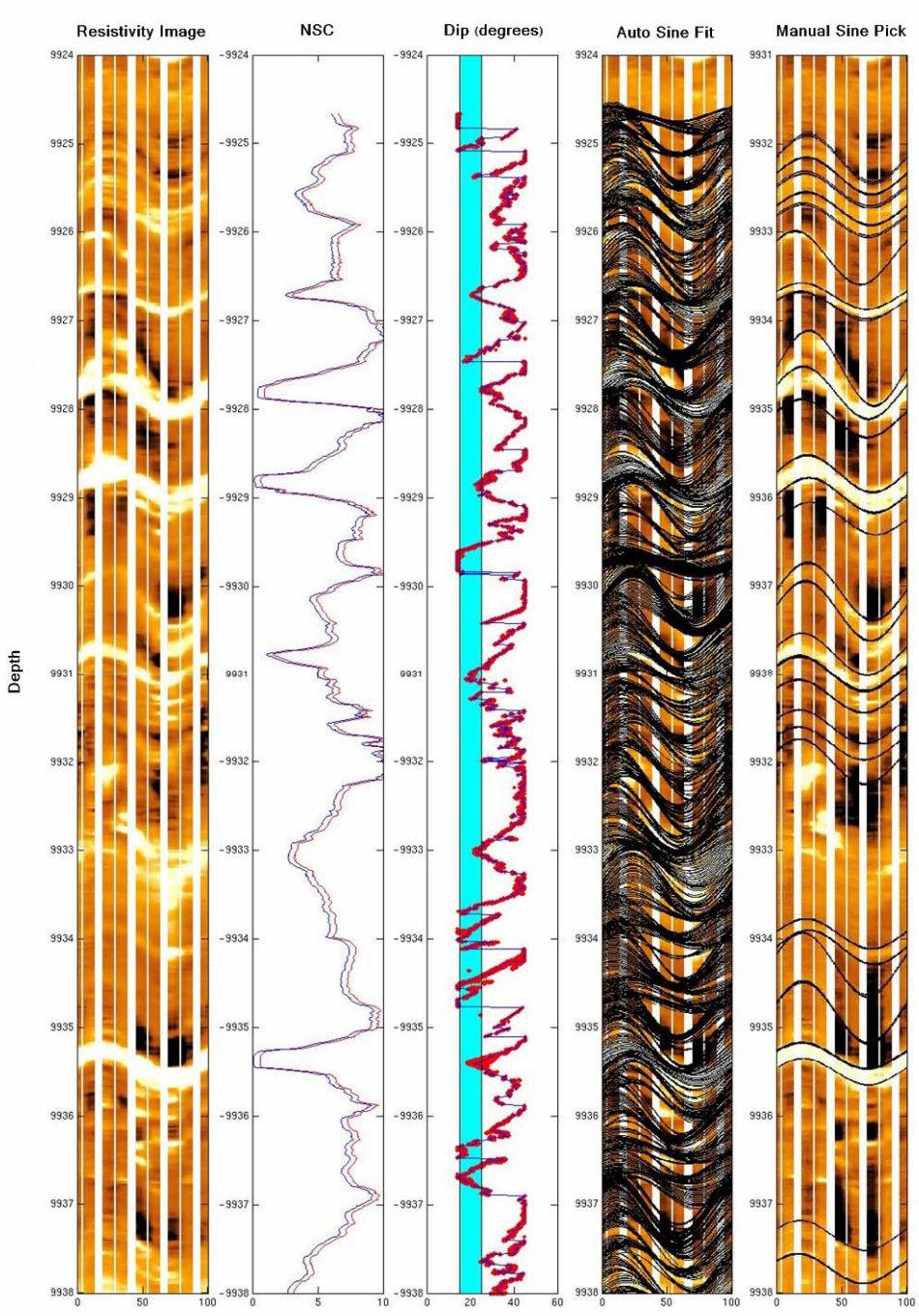

Figure 7. 5*: An example of automated sinusoid fitting using the NSC. From left*

to right are the depth interval (in feet), image log used, NSC (blue line) and the introduced uncertainty limit up to which the NSC could vary (red line), dip corresponding to the best fitted sinusoid (blue line) and all possible dip values that can occur when NSC is allowed to vary up to the introduced uncertainty limit (red dots), Image log along with the best fitted sinusoids, image log along with the manually picked sinusoid. As the deviation of the well varied from 18 degree to 22 degree, all dips that are approximately equal to the well deviation are taken as planar lamination, hence a tolerance of +/- 3 degree to this value is taken as horizontal beds as shown by the blue shaded region in the dip plot, the rest are taken as dipping beds, and those depths where the range of dips spans in both criteria are defined as uncertain regions.

7.2.3 Protocol development

A protocol in object-based image analysis is a set of rules and controlling parameters that are arranged in a sequential order and work together to automate image classification. The main processes include image segmentation, knowledge-base design, and image classification (chapter 2).

Image segmentation: The aim of image segmentation is to create objects that can be grouped into appropriate classes in the classification process. The image objects formed during segmentation are thus the basic units used for a successful classification. As the image log doesn't distinguish sand, shale intervals and cross bed and planar lamination intervals properly, it is difficult to create image-objects to distinguish these classes from image logs alone. Hence, in this 'difficult data set' the segmentation of the image log is constrained using the filters; Sand-shale filter created from Neutron Density Separation and Dip estimation from the image log using uncertainty-based sinusoid fitting, in such a way that adjacent, similar pixels are grouped into objects in each unit separately. That is, no groupings of adjacent, similar pixels are allowed to cross the boundaries defined by the filters. Hence, the method

successfully distinguishes objects that belong to each of the classes; sand, shale, cross bed and planar laminations. Other filters can also be generated to enhance the image classification if needed, for example there could be a bad data filter based on caliper logs.

Knowledge based design: A *priori* counting and naming of the classes is done based on examining core, core photographs and other geophysical logs. Based on this knowledge, a class hierarchy, which contains all classes in the desired classification scheme, is developed. The class hierarchy developed for the data set used in this study is given in figure 7.6.

The classification of the image objects is then performed by a supervised classification, based on fuzzy logic (Benz et al., 2003) where all objects in the image are given a value between 0 and 1, which represents the likelihood of their being a member of different classes in the class hierarchy. The classification is carried out using classifiers; nearest neighbour (Chapter 2) classifiers and membership functions (chapter 2). The classifiers used to distinguish each class in the class hierarchy are shown in figure 7.6.

The FMI image log consists of white vertical stripes throughout the image resulting from spatial gaps between the pads used to acquire the data (Chapter 1). In the previous study (chapters 3 and chapter 6) we spliced the image to remove these regions where data is absent. However, in this study, this no-data region has been classified into a separate class based on its spectral property and further image analysis has been focused on the image log where we have data. This classification can be done using a Nearest Neighbour classifier which

can be trained by selected samples to represent the entire feature range corresponding to the data region and no-data region. The feature ranges defined by these selected samples are then used to train the classifier for further classification. The no-data region corresponds to pure white regions with spectral value 0, 0, 0 and can be easily defined by samples. Due to the same reason a Membership Function can also be used as a classifier which can describe classes based on predefined rules to formulate knowledge about the image content. That is, a logic operator can be used to define the spectral value 0, 0, 0 as no-data and the rest as data regions. In order to avoid any misclassification of the no-data regions with carbonate concretions which are also represented by white or light colour in the image log (chapter 6), the no data regions can be colour coded. In this study, the image log was prepared with blue background which has spectral value 0, 0, 255 from TerraStation software, and this spectral value was used to train the classifier to distinguish data from no-data regions without incorporating any carbonate concretions into this no-data class.

The data region is then divided into sand, uncertain and shale regions based on NDSEP filter. Membership Function is used here to formulate knowledge based on the filter to mark the bed boundaries. Further, the sand and shale regions are analysed to classify any carbonate cements present in these intervals. As carbonate cemented regions are well marked in an image log due to their high resistivity, the classifier can be either trained to distinguish this region by selecting samples to train Nearest Neighbour or by incorporating the spectral range directly by using Membership Function classifier. Then, the non-carbonate cemented sands are classified into cross beds, planar lamination and

uncertain regions based on the Dip filter. Membership Function is used here to formulate knowledge based on the filter to mark the bed boundaries.

Classification: Classification is a process of assigning each segmented image object into appropriate classes (to different lithofacies in this case) based on the above classifier training. The principle of image classification is that each object is assigned to a class based on its characteristic features, by comparing it to the predefined feature ranges (obtained from the discussed classifier training) in the feature space (intuitively, a feature space is like a cross plot of all features used). Doing so for all image objects results in the image classification (chapter 2 and examples of image classification using this methodology on different kinds of images are shown in chapters 4, 5 and 6).

The classification result is then compared with the visual interpretation of the core photograph, and is further revised if need be (Chapter 5 and 6). The refined knowledge base incorporating the expertise of an image interpreter is saved as a so-called class hierarchy 'mask' (chapter 5), which acts as a library of defined features and distinguishing feature ranges for each class in the class hierarchy. By calling this class hierarchy mask using the protocol, we incorporate the knowledge derived from the training above, and hence from the human interpreter to perform the classification. Figure 7.6 shows the class hierarchy developed for the image used in this study, and the types of classifier used to distinguish each class. However, the class hierarchy and class descriptors depend on the specific field, lithology or rock types considered. The order in which classes are arranged in the class hierarchy can be changed, provided class

descriptors are trained to suit the new arrangement to properly classify the data set.

The protocol (chapter 2 and 5) developed by experiments in the given data set now offers a powerful tool for automated lithofacies identification for any large interval of image log from similar geological setting. The protocol can be easily adapted when classifying images form different geological settings as explained in chapter 5.

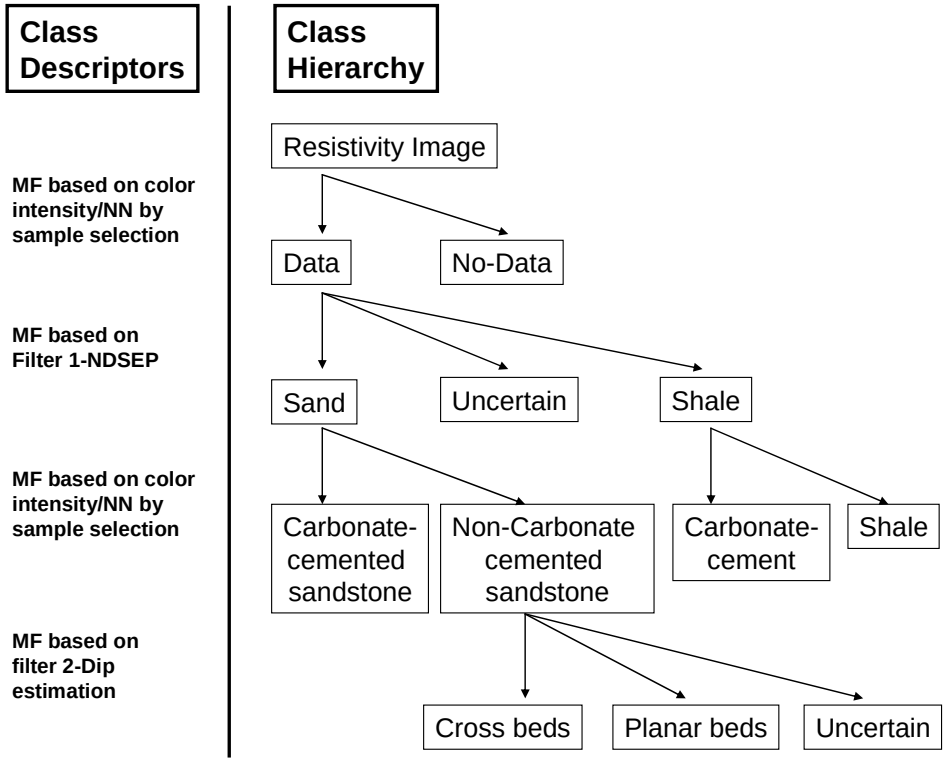

Figure 7. 6*: Class hierarchy developed for the data used in this study along with the class descriptors used in each stage. The 'no-data' class comprises regions were the image log is not recorded due to limited borehole coverage of the tool (figure 1). Two types of classification algorithms (class descriptors) are used in this classification scheme. A Membership Function (MF) is used when the class can be defined based on a single feature and hence can be defined easily by a simple function, for example by being greater than a*

particular feature value in a feature range. A Nearest Neighbour (NN) class descriptor is used when a class is defined based on two or more features and hence needs to operate in a multi- feature space; the classifier is then trained based on samples selected to define each class. Both classifiers operate based on fuzzy logic.

7.3 RESULTS

Once developed, the protocol is tested on the same training interval to ensure that it functions correctly and to compare the result with the ground truth – in this case the lithofacies classification created by a geologist based entirely on core. The result of this on the data set used in this study is explained in detail in this section.

The borehole image was calibrated with core photographs and other geophysical logs to create a class hierarchy that includes sandstone (horizontally stratified sandstone and cross-bedded sandstone), shale, carbonate, and uncertain regions. Initial trials to find a better lithofacies classification for the image logs for the given study area were performed on a small interval of data. Data was carefully selected for the initial protocol development so that the selected interval included all of the lithofacies that need to be identified as shown in figure 7.1.

As explained in figure 1.1 (chapter 1), an image log (FMI) does not have full circumferential borehole coverage. Hence the initial step was to distinguish the image log data and the background (gaps between the data) within the image. A Membership Function based on spectral intensity of the image log is used to do this. A Nearest Neighbour could also be used to do the same by selecting samples that belong to data and to the background.

In the next step the data is separated into sand and shale regions. As the image log used in this study did not show a clear distinction between sand and shale everywhere, a Membership Function based on the sand-shale filter defined earlier is used to do this. Constraining the segmentation of the high resolution image log with low resolution standard logs may not always be good practice, especially if we have thin beds. However, these are shallow water sands and typical (turbidite) thin beds are absent. Also the difficulty in sand-shale separation from image logs is a rare case. So in most cases, we may not need this filter. The uncertainty in determining an exact boundary between the sand and shale is taken into account by classifying the transition zones as uncertain regions. Further, the carbonate-cemented regions in the data are separated into a separate class. As the carbonate cements are seen in very bright white colours in the image log, a Membership Function based on spectral intensity is again used to distinguish them in the data (however again, using Nearest Neighbour classification for this is also possible). The classification result is shown in figure 7.7.

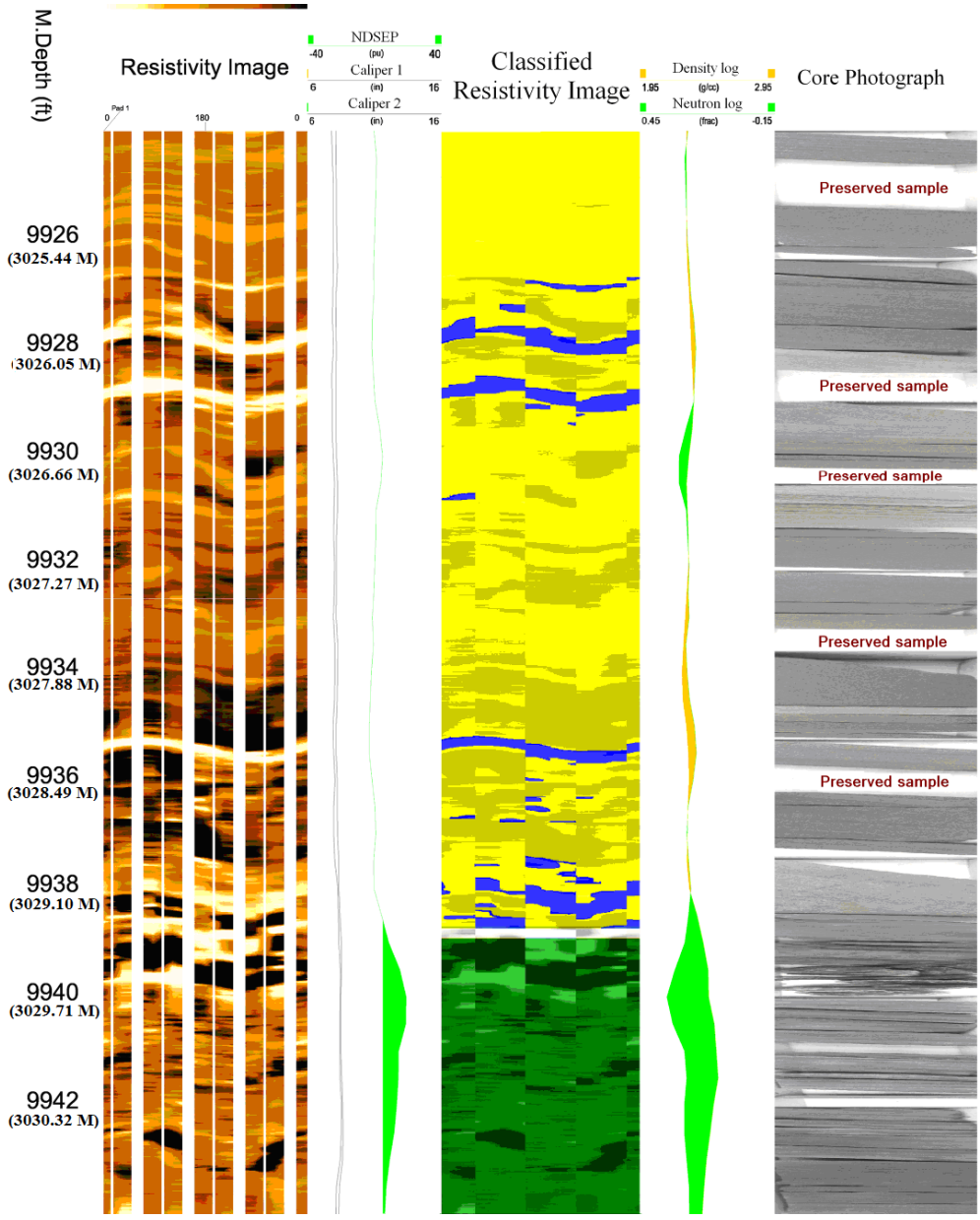

Figure 7. 7*: The classification result using the sand-shale filter. The figure shows, from left to right, the depth, image log used for the study, caliper logs and the neutron density separation (NDSEP in equation (1); green shaded region representing shale, and non-shaded region is sand) , classified image using object-based image analysis, neutron and density logs, and the core photograph. The image log is classified into sand (yellow shade), shale (green), carbonate cements (blue) and uncertain regions (white).*

Similarly, using the second filter created from dip estimation, the sand bed region is further divided into horizontally stratified sand beds (planar laminations), cross-bedded sands, and uncertain regions where it is difficult to define clearly whether it is a cross-bed or planar lamination based on the dips calculated within the range of uncertainty used. Since these subdivisions are formed under each parent class in the hierarchy, they carry features from parent classes in addition to their own features introduced by the new level of filters.

The automated image log classification including both filters is then compared over the same well interval with the independent lithofacies classification done by a geologist which was entirely based on core photographs. Figure 7.8 shows the image log interval used for this protocol testing phase, along with the automated lithofacies identification obtained form the same using the new methodology, the core photographs, and the geologist's qualitative lithofacies classification based on the core photographs.

Both the geologist's classification and automated classification identified the cross bed region at depth 9924 feet/3024.84 meter. This is followed by an uncertain region in the automated classification result, which may correspond to the erosion surface shown in the core photograph: the image log looks fairly homogeneous in spectral and textural properties which leads to the possibility of fitting both a high and low angle sinusoid at this depth, and hence this region is marked as an uncertain region. The planar lamination at depth 9925 feet/3025.14 meter has been identified by both classifications, though there is a slight variation in the thickness of the identified bed. The preserved sample region at 9925.5 feet/3025.29 meter appears to be of cross bed according to the automated

classification, followed by a good match of cross bedded interval by both classifications. The highly cemented interval (possibly carbonate cementation) at interval 9929 feet/3026.36 meter is not evident in the core photograph while the image log shows a robust indication of its presence so has only been identified by the automated classification scheme.

In the next interval we see a good match between the geologist's classification and that obtained from automated image classification, except in the carbonate-cemented region at the interval 9930-9931 feet/3026.66-3026.97 meter. This dispersed carbonate cement was not recorded in the image log. This may be because it is dispersed in sandstone and hence the interval does not have high resistivity as it is not fully non-porous and non-permeable. Other than this carbonate cement region and a few thin planar laminations identified from the image log, the rest of the automated result shows a good match with the geologist's interpretation.

Interval 9932 -9933 feet/3027.27-3027.58 meter is not imaged clearly in the core photograph and hence is marked as an uncertain region by the geologist, whereas it is found to be a cross bedded interval by the automated method. The next uncertain interval from the geologist at 9934 feet/3027.88 meter is most probably planar lamination as automated sinusoid fitting showed it is as planar laminations and the geologist also said it might be planar lamination (hence marked with dotted horizontal lines). The preserved sample at 9935 feet/3028.19 meter appears to belong to a planar lamination followed by a good match of both results up to depth 9936.5 feet/3028.65 meter.

The automated classification showed the interval that follows is planar lamination while the core photograph is not very clear in this interval and the geologist thinks it may be a cross bedded interval. However, the core can become tilted when arranged so it is possible that there is a misorientation in lamination or bedding direction between the two data sets in this non-vertical well. This interval is followed by a roughly matching classification (the carbonate bed detected by image classification is not present in the core photograph) which is followed by the shale interval (after the thin uncertain region defined from the sand-shale filter to account for its low depth-resolution being used to mark bed boundaries in high resolution image data).

However the result obtained from the image log integrating both standard logs (7.2.1) and the dip log (7.2.2) showed a reasonably good match with the independent core interpretation from the geologist. Hence, the developed protocol was tested on another interval of the data which was not included in the initial trials. The protocol was developed on an image interval with prominent cross bedded sand. To make the test more challenging, testing of the protocol was done on an image interval with prominent shale and planar laminated sand. Figure 7.9 shows the test result and its comparison with the core photo interpretation made independently by the geologist.

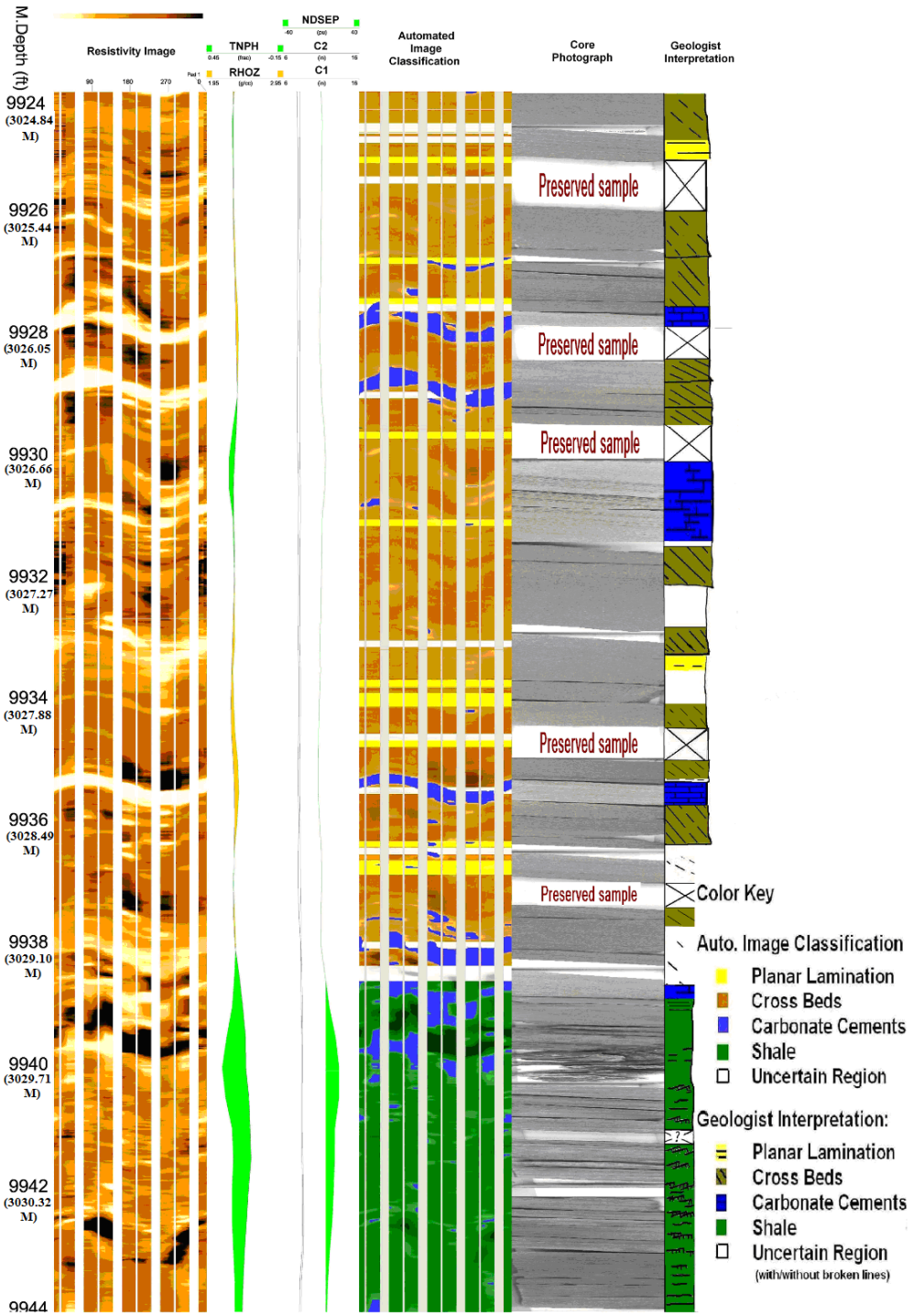

Figure 7. 8: The classification result using both the filters, NDSEP and dip estimation. The figure shows, from left to right, the depth interval, image log used for the study, neutron and density logs, caliper logs, and the derivative log-NDSEP, classified image using object-based image analysis, core photograph and the geologist interpretation based on core photograph. Color key is given to the right side of the figure

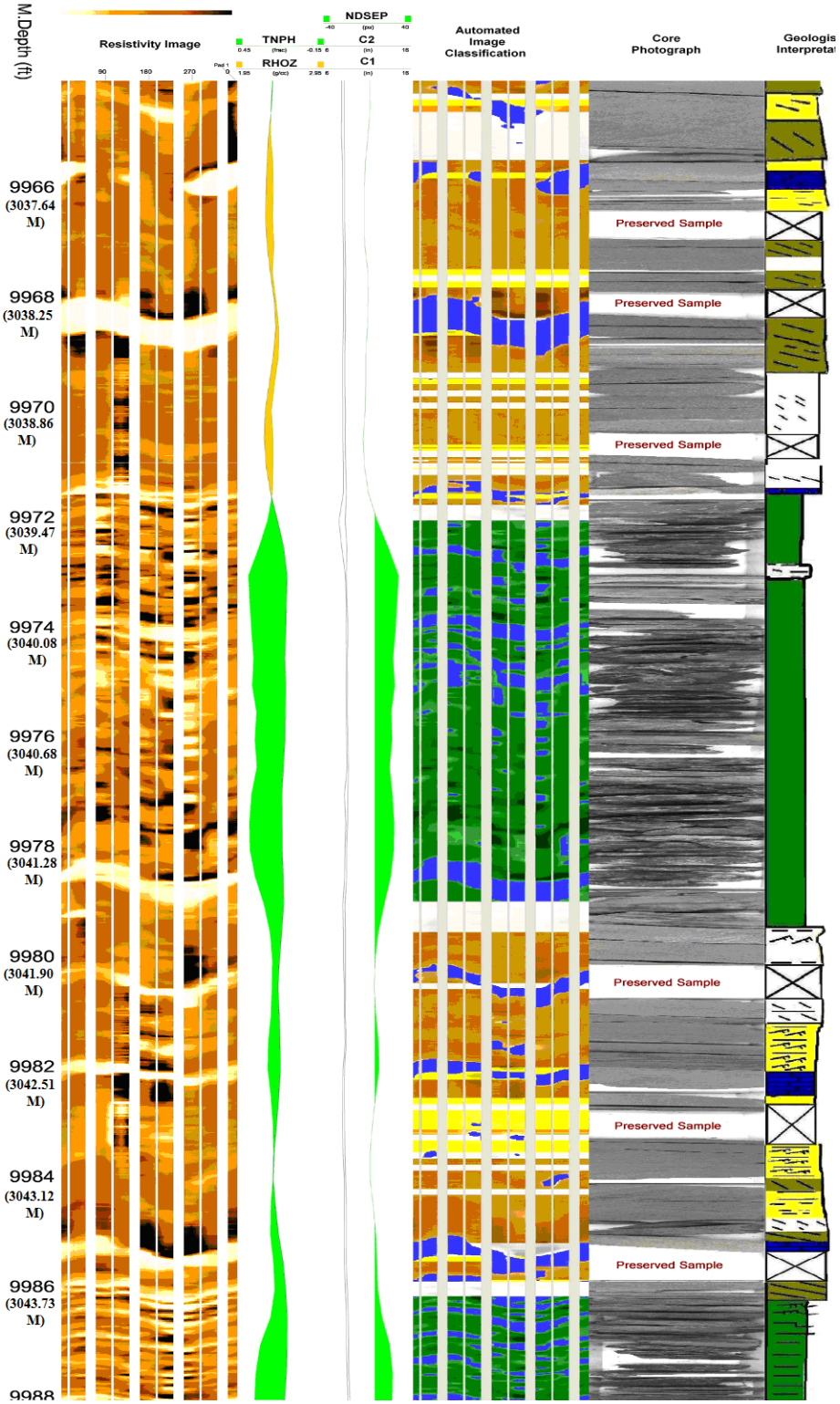

***Figure 7.9**: Testing of the classification protocol. The figure key and color key are similar to figure 7.8*

A one to one comparison of the result obtained from the automated method is made with the geologist's interpretation. This is done by comparing the results in a sliding window of every 0.2 feet/0.06 meter, and the outcome is summarised in the histogram plot shown in figure 7.10. According to the automated interpretation, out of the 120 window samples in the tested interval from 9964 feet/3037.03 meter to 9988 feet/3044.34 meter, 57 samples belonged to sand which are further divided into 11 planar laminated, 35 cross-bedded, and 11 carbonate cemented sand; 46 samples belonged to shale, 14 samples where classified as uncertain regions introduced from the sand-shale filter, and 3 samples remained as unclassified due to the shoulder effect of the sine fitting filter. According to the geologist's interpretation of the same interval, out of the 120 samples, 40 samples belonged to sand which are further divided into 14 planar laminated, 21 cross-bedded, and 5 carbonate cemented sand; 48 samples belonged to shale, 12 samples belonged to regions where core was absent or was taken as a preserved sample and hence the core photo was not available, and20 samples where the core photo was vague or does not show any clear feature to definitely classify into any regions, were marked as uncertain regions. However the geologist did mark the probable class for these uncertain regions with dashed lines, shown in both figures 7.8 and 7.9, as the non-colour coded regions other than the no-core regions which are marked with 'X'. Though these 'probable' regions are not assigned into any class, a qualitative, visual, comparison of the result is done with the automated result and it shows a good match as can be seen in both figures 7.8 and 7.9.

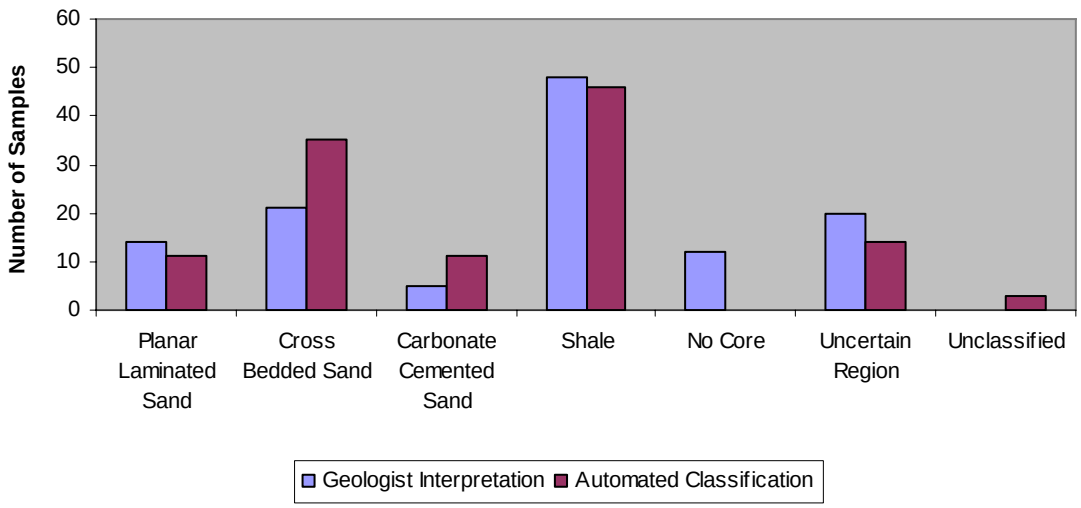

***Figure 7. 10**: Histogram comparing the classification result by a geologist based on core photographs, and the automated interpretation based on the image log.*

An accuracy assessment of the result was obtained by doing a one to one comparison of the classification result obtained by this automated method with that of the geologist's interpretation, using the data summarised above. For this, the no-core regions and uncertain regions defined by geologist have been excluded, but the uncertain regions defined by the automated method retained. The result is summarised in table 7.2. The result showed that out of the remaining 88 samples, 3 were unclassified due to the shoulder effect of the dip estimation filter, and 7 were uncertain regions defined by the filters, together estimated as uncertain regions. Out of the other 78 samples, 7 were miss-classified and 71 were classified correctly, giving an overall accuracy of 91.03%.

		Geologist's Interpretation					
Automated Classification		Planar Lamination	Cross Bedding	Carbonate-Cement	Shale	Uncertain	Unclassified
	Planar Lamination	7	1	0	0	-	-
	Cross Bedding	6	12	0	0	-	-
	Carbonate-Cement	0	0	5	0	-	-
	Shale	0	0	0	46	-	-
	Uncertain	1	4	0	2	0	-
	Unclassified	0	3	0	0	-	0

***Table 7.2**: Accuracy assessment of the automated classification obtained using the protocol is done by comparing the classification result with a geologist's interpretation.*

7.4 CONCLUSIONS

The object based image analysis methodology has been used to classify the lithofacies from a 'difficult' dataset. This study developed methods to integrate standard logs with image log data and the effective integration of standard logs with an image log which showed no prominent difference between every sand and shale region within some intervals, proved to be successful, providing better lithofacies discrimination. The dip estimation from the image log using the uncertainty-based sinusoid fitting proved to be helpful for an automated cross bed and planar lamination identification, taking into account the deviation of the well. Thus, this study showed one way to process difficult data sets and extract information from them by integrating other complementary information from standard logs and image derived logs.

Chapter 8

AUTOMATED INTERPRETATION OF IMAGE LOGS: CONCLUSIONS

Summary: The areas of study are summarized in this chapter by evaluating the results and conclusions drawn from the various approaches and methodologies adopted to address the problem of automated image log interpretation.

8.1 SUMMARY

The central theme of this study was to develop an effective methodology to automate the interpretation of image logs for lithofacies prediction. This has been approached in two different ways. The first method is an extension of already existing technique which is a pixel-based pattern recognition technique. In this method, textural analysis of the image log is performed to quantify image properties. These extracted quantitative properties along with the geologist's interpretation based on core photos were used to train a back propagation Neural Network which in can then be used for lithofacies identification from image logs of the same geological setting. The second method is a novel approach for image log interpretation, in which, identical neighbouring pixels in the image were grouped together as image-objects and the textural, spectral and spatial characteristics of the objects were calculated and related to various core-derived lithofacies.

It is inferred that the classification can be biased by the signatures of the data if one data type alone is used for lithofacies identification. Hence, the pixel-based image analysis technique is extended with the integration of conventional geophysical logs as inputs to the neural network for better lithofacies identification. Therefore, data of different resolutions (high resolution image log with low resolution standard logs) and dimensions (2-dimensional image log with 1-dimensional standard log) were combined. The standard existing petrophysical procedure for integration of these different resolution data is, up-scaling the high resolution image log to the low resolution of conventional log data, which in fact compromises the fine details recorded in the image log. Hence, in this study, the conventional logs were interpolated to match the scale of the image logs, whereby retaining the fine details of the information recorded in image logs. The integration of two dimensional image logs with one dimensional standard logs has been approached by extracting the properties of the image log in one dimension (as a function of depth) which was then integrated with conventional logs to train the neural network for lithofacies prediction.

The pixel-based image analysis method was applied on a 50 feet interval of image log data which is a sand interval with three major lithofacies types. The lithofacies were bioturbation (silty sand), cross-stratification and horizontal stratification. A sliding window of 5 pixel depths was chosen to calculate the averaged textural features from the image log as a function of depth. The textural features, along with conventional geophysical logs (neutron, gamma and density) were used to train a feed forward back propagation neural network. The geologist's interpretation based entirely on core photographs was used as the ground truth (bearing in mind that this may also contain inaccuracies). The trained neural network was tested on the entire dataset and

an accuracy assessment of the classification yielded 77.49% accuracy compared to ground truth.

As image logs are high resolution images of the electrical resistivity of the borehole wall, the pixel-based method does not fully utilize the scope of the dataset. This is because at a given depth, an averaged single feature value is derived from the image log that covers the entire circumference of the borehole wall. Also, the averaged feature value may not be the representative of a particular depth when the image properties are irregular in nature. Thus, methodologies that utilize the high resolution spatial information encoded in the image log need to be introduced.

A second methodology is developed which involves grouping identical neighboring pixels to form 'image-objects'. The spectral and textural features of the image-objects are then calculated, but this time the spatial information is preserved. A fuzzy set classification algorithm, either 'nearest neighbor' or a 'membership function' is then used to perform the classification. When the classes are distinguishable based on one or two features the membership function is used, and when a number of features are necessary for the classification nearest neighbor is used. In a nearest neighbor classifier, samples are chosen to define the range of the feature values that can distinguish various lithofacies present in the field. In a membership function, appropriate thresholds are defined in the feature range that can identify different lithofacies. The sample selection or threshold definition is done by an expert geologist and hence this method incorporates the knowledge and expertise of a geologist with respect to the local geological heterogeneity of the area.

Information from the conventional geophysical methods can be integrated into the methodology to complement the image logs in lithofacies prediction. This helps when the image log alone does not provide the necessary information for a successful interpretation. In this case, geophysical logs are imaged by color coding the log signatures to make them two dimensional. The spectral, spatial and textural details of the reservoir recorded in the image log along with conventional log signatures can yield a visual and realistic interpretation of the borehole wall.

Apart from integrating conventional logs, image-derived logs can also be integrated with image logs. A novel automated dip picking algorithm has been developed to mark bed boundaries between cross stratification and horizontal stratification for image log data from a deviated well. The proposed methodology is based on the pixel intensities in the image, finding a continuous sinusoidal path that runs through the image from left to right at each depth. The best fitting sinusoids are those along which the pixel intensities are most similar. Hence, this methodology is not sensitive to occurrences of vacuoles, nodules or vugs as they will show local contrast in the spectral values. A number of attempts to use sinusoid fitting for dip estimation in image logs can be found, but this method is different from those methods because the best fitting sinusoids are obtained within a formal uncertainty limit, at every pixel depth in the image log. As the best fitting sinusoids are calculated at every depth rather than one in a predefined window, it is easy to distinguish fractures from bed orientations. This is because the stratification planes are generally seen in groups, while fractures are seen as single anomalous sinusoids at specific depths.

Another major advantage of the new method is that the sequential arrangement of various steps that work together along with the defined feature ranges or thresholds for various classes can all be saved as a protocol. This protocol can be used to classify lithofacies from image logs from the same geological setting. Further, the method can easily be adapted to new fields with different geological settings with an appropriate modification to the geologist-defined lithofacies classes present in the field, plus features and the feature ranges that distinguish each of the classes.

In principle, object based image analysis is applicable to different image types and hence the method was first applied on an outcrop photograph. The outcrop photo was collected during a geological field trip to Thornton Lock area in south east Scotland and the outcrop consisted of sand-shale sequence. Hence, the objective was to test the new method to classify the sand-shale sequence. Spectral feature was used in sand-shale discrimination and textural features were used in sand-shale inter-bedded zones. The method demonstrated its effectiveness in classification when appropriate samples were chosen to define the specific spectral or textural feature ranges corresponding to each class. Thus, this application integrated a geologist's knowledge and the advantages of computer power in the successful classification of an image.

Next the method was applied to core photographs for automated lithology identification from a South Batra well (Nile delta). The lithology consisted of sand, shale and carbonate cement and spectral features were used in the classification algorithm. A protocol was developed with appropriate sample objects to define feature ranges for the classes, and was tested on the same core photograph section. The protocol was then tested on another core

photograph interval and an accuracy assessment of the classification showed 94.29% accuracy.

Following the successful application of the method to outcrop and core photograph interpretation, the method has then been applied to an image log interval in which the pixel-based methodology had already been tested. Similar to the pixel-based analysis, textural properties of the image-objects were used as the classification parameters. The classification results showed 84.41% accuracy. The calibration and comparison of the classification result with core based interpretation provided confidence in the extrapolation of results from depths with core control to intervals with poor or no core recovery. This is important because not every borehole intervals are cored due to borehole conditions and high cost.

The method has finally been applied on a 'difficult dataset' from a deviated well. The dataset is referred to as difficult because the image log did not show a clear distinction between every conductive and resistive region, while the standard logs and core photographs do so. Hence, for a successful lithofacies classification from this data set, the methodology was extended to incorporate the wealth of information from standard logs. Taking account of the well deviation, bed orientations were calculated using automated sinusoid fitting at every pixel depth in the image log within a formal uncertainty framework, and were used with image logs to identify horizontally stratified beds from dipping beds. Thus, this study demonstrated a practical approach to processing difficult data sets and extracting information from them by integrating other complementary information from standard logs and image derived logs.

The application of the pixel-based and object-based image analysis methodologies on the same dataset concluded that the object-based method yields a better lithofacies classification compared to the pixel-based method. It did not only improve the classification but also resulted in much more realistic bed boundary identification and hence demonstrated the added advantage of utilizing the image properties in two dimensions (as a function of borehole depth and circumference), preserving the spatial characteristics inherent within the image in the classification result. Also, the pixel-based image analysis failed to detect fine heterogeneities since an averaged image property in a defined window is calculated. Moreover the accuracy assessments show that the pixel-based method yields 77.49% accuracy, while the object-based method yields a much better accuracy of 84.41%.

The automation of image log classification proved to be useful in dealing with virtually any quantity of data. There is an amount of effort required in selecting representative training data, but this is a common problem for all modeling methods relying upon real data. On the other hand, this allows the incorporation of the expertise of an experienced geologist within the automated procedure of physical data analysis, and hence human logic and reasoning are involved in effective automated image log classification. The incorporation of the expertise of a geologist into a classification scheme offers a robust and repeatable result, which is not subject to variations depending on the interpreter's state of mind, and can result in less variation depending on their individual character (e.g., how certain they have to be before they make a definite classification) since the algorithm can be trained using input from multiple interpreters, thus mediating their individual influence on the result.

8.2 MAIN CONCLUSIONS

- This thesis is an attempt to develop an effective methodology to automate/semi-automate the image log classification for lithofacies prediction
- Main challenges addressed are,
    - Quantification of features from image log
    - Effective integration of data of different resolution and dimensions
    - Incorporation of expertise of one or more geologists/experts
    - Methodology being easily adaptable to different geological settings
- Quantification of features from image logs have been approached using two methodologies
    - Pixel-based pattern recognition technique
    - Object-based image analysis
- Pixel-based pattern recognition technique: Textural features were extracted from image log in the form of one dimensional curves (single averaged property at each depth)
    - Textural features were quantified successfully. However, spatial distribution of properties was lost, resulting in misclassifications.
    - In case of any irregular textural features recorded in the image log only an averaged feature value is obtained which is not a true representation of the geology.
    - Quantification and averaging of textural features in windows could lead to missing of thin bed information. Also, this can

lead to erroneous bed boundary determination and hence errors in bed thickness calculation.

- Further, when properties are studied at pixel level, there is a probability for adjacent pixels to be classified into the same class unless there is a significant difference in pixel values.

- All these disadvantages are being taken care of by using object- based image analysis
- Object- based image analysis: Image log being segmented into objects - group of pixels- and textural and spectral features of these objects are calculated. Hence, along with the spectral and textural image properties, the spatial information is also quantified.

- Lithofacies classification being biased by one data type is avoided by introducing an effective data integration method which could accommodate data of different resolution and dimension, for example, image logs, standard logs, geologists interpretation based on core.
- To account for the difference in resolution of the image log and standard logs, the standard logs are linearly interpolated in such a way that the data exist at the same increments as the image log.
- The integration of data of different dimensions has been approached in two different ways
  - Quantifying features from image log in the form of one dimensional curves
  - Image the one dimensional standard logs to two dimension and depth match with image logs.
- It has been found that the evaluation of data in two-dimension preserves the actual spectral, spatial and textural details of the subsurface recorded in the image log. It enables the visualization of

the exact arrangement of lithofacies in the reservoir compared to the modeled lithofacies prediction quantified from one dimensional image log properties.

- In object-based image analysis, any number of imaged data, for example- standard logs, geologist's interpretation, core data, local geological information or expertise of one or more geologists/experts can be incorporated to assist in image log classification.
- Classification of quantified image properties along with other incorporated data such as standard logs into lithofacies classes has been approached in two different ways
    - Neural network
    - Fuzzy-set classifier
- Since fuzzy logic can model imprecise human thinking and can represent linguistic rules, this study proves fuzzy logic to be ideal for interpreting lithofacies (as training data are based on interpretation by a geologist). Nearest Neighbour or Membership function or combination of both which are based on fuzzy logic have been used as class descriptors in this study.
- The selection of classifier is dependant on number of features of the image-objects that need to be used for a successful image classification. If a class can be separated from other classes by one or very few features the application of Membership Function is recommended, otherwise the Nearest Neighbour approach is preferred which can operate in multi dimensional feature space.
- A protocol containing the sequential arrangement of all classification steps involved in the object-based image analysis has been developed to automate the lithofacies classification from the image logs.

- The designed protocol can be directly applied to datasets from the same field and can be easily adapted to different fields with minimum supervision. This makes the method easily adaptable to different geological setting because, the protocol can be easily edited according to data or field requirements.
- The method is applicable to many geological image types and the application of the method on core photos, outcrop photos and different image log data sets proved it to be robust for geological interpretation. The method is repeatable and can be used to process large amounts of data.
- It is concluded that the developed method can be used in the automated interpretation of image logs from the same geological setting, but this needs tested for performance. This feature of the method is expected to have a real application as hundreds of wells are drilled in the same field nowadays. The method can thus provide an in situ interpretation of lithology or lithofacies in the field.

REFERENCES

Antoine, J. N., and J. P. Delhomme, 1990, A Method to Derive Dips from Bed Boundaries in Borehole Images: SPE 20540, p. 121-130.

Baatz, M., N. Arini, A. Schape, G. Binnig, and B. Linssen, 2006, Object-Oriented Image Analysis for High Content Screening: Detailed Quantification of Cells and Sub Cellular Structures with the Cellenger Software: International Society for Analytical Cytology, v. 69, p. 652-658.

Baatz, M., and A. Schape, 2000, Multiresolution Segmentation - An Optimization Approach for High Quality Multi-Scale Image Segmentation, Angewandte Geographische Informationsverarbeitung XII, Ed. J. Strobl et al. AGIT Symposium, Salzburg, Germany, p. 12-23.

Bagheri, A. M., B. Biranvand, S. Rezazadeh, M. Fasih, and H. Bakhtiari, 2005, Integrated Analysis of Core and Log Data to Determine Reservoir Rock Types and Extrapolation to Uncores Wells in a Heterogeneous Clastic and Carbonate Reservoir, International Symposium of the Society of Core Analysis Toronto, Canada.

Barr, S., S. Revillon, T. Brewer, P. Harvey, and J. Tarney, 2002, Determining the Inputs to the Mariana Subduction Factory: Using Core-Log Integration to Reconstruct Basement Lithology at ODP hole 801C: Geochem. Geophys. Geosyst., v. 3, p. 1-26.

Bartetzko, A., H. Paulick, G. Iturrino, and J. Arnold, 2003, Facies Reconstruction of a Hydrothermally Altered Dacite Extrusive Sequence: Evidence from Geophysical Downhole Logging Data (ODP Leg 193): Geochem. Geophys. Geosyst., v. 4, p. 1-24.

Benz, U. C., P. Hofmann, G. Willhauck, I. Lingenfelder, and M. Heynen, 2004, Multi-Resolution, Object-Oriented Fuzzy Analysis of Remote Sensing Dta for GIS-Rady Iformation: ISPRS Journal of Photogrammetry and Remote Sensing, v. 58, p. 239-258.

Benz, U. C., P. Hofmann, G. Willhauck, I. Lingenfelder, and M. Heynen, 2003, Multi-Resolution, Object-Oriented Fuzzy Analysis of Remote

Sensing Data for GIS-Ready Information, Definiens Imaging GmbH, Trappentreustr. 1, D-80339 Munich, Germany.

Bhatt, A., 2002, Reservoir Properties from Well Logs Using Neural Networks, Norwegian University of Science and Technology, Trondheim.

Bhatt, A., and H. B. Helle, 2002, Determination of Facies From Well Logs Using Modular Neural Networks: Petroleum Geoscience, v. 8, p. 217-228.

Bishop, C. M., 1996, Neural Networks for Pattern Recognition, Oxford University Press.

Blackbourn, G. A., 1990, Cores and Core Logging for Geologists: aithness, Whittles Publishing.

Blaschke, T., and J. Strobl, 2001, What's Wrong With Pixels? Some Recent Developments Interfacing Remote Sensing and GIS: GIS, v. 6, p. 12-17.

Bond, C. E., A. Gibbs, Z. K. Shipton, and S. Jones, 2007, What Do You Think This Is? 'Conceptual Uncertainty' in Geoscience Interpretation: GSA Today, v. 17, p. 4-10.

Brown,S.,(1984) Chapter 6, Jurassic. In: Introduction to the Petroleum Geology of the North Sea. Ed. Ken Glennie. Blackwell Scientific Publications. pp. 236

Bruke, J. A., R. L. Campbell, and A. W. Schmidt, 1969, The Lithoporosity Cross Plot, Society of Professional Well Log Analysts 10th Annual Symposium Transactions, p. 1-29.

Bush, J. M., W. G. Fortney, and L. N. Berry, 1987, Determination of Lithology from Well Logs by Statistical Analysis: SPE Formation Evaluation, v. 2, p. 412-418.

Cannon, S. J. C., M. R. Giles, M. F. Whitaker, M. P. Please, and S. V. Martin, 1992, A Regional Reassessment of the Brent Group, UK sector, North Sea: In: Geology of the Brent Group (Ed. by A.C. Morton, R.S. Haszeldine, M.R. Giles and S. Broom), Geological Society Special Publication, v. 61, p. 81-107.

Chang, H.-C., Kopaska-Merkel, C. D.C, H-U., , and S. R. Durrans, 2000, Lithofacies Identification Using Multiple Adaptive Resonance Theory Neural Networks and Group Decision Expert System: Journal of Computers and Geosciences, v. 26, p. 591-601.

Chang, H. C., D. C. Kopaska-Merkel, and H. C. Chen, 2002, Identification of lithofacies using Kohonen self-organizing maps: Computers & Geosciences, v. 28, p. 223-229.

Chen, G. H., W. S. Wu, and K. Y. Mao, 2001, Identifying Formation Lithology Using Formation Microscanner Images: Petroleum Exploration and Development, v. 28, p. 53-55.

Cheung, P. S., 1999, Microresistivity and Ultrasonic Imagers: Tool Operations and Processing Principles with reference to commonly encountered Image Artifacts.: In: Lovell, M.A., Willianmoson, G. and Harvey, P.K. (eds.), 1999, Borehole Imaging; Applications and Case Histories, Geological Society Special Publication v. 159, p. 45-57.

Chikhi, S., M. Batouche, and H. Shout, 2005, Hybrid Neural Network Methods for Lithology Identification in the Algerian Sahara: International Journal of Computational Intelligence, p. 25-33.

Chitale, D. V., 2005, Borehole Imaging in Reservoir Characterization: Implementation of a Standard Interpretation Workflow for the Clasitic and Carbonate Reservoirs, SPWLA 46th Annual Logging Symposium, New Orleans, Louisiana.

Clavier, C., and D. H. Rust, 1976, MID Plot: A NEw Lithology Technique: The Log Analyst, v. 17, p. 16-24.

Cooper, P., H. M. Arnaud, and P. G. Flood, 1995, Formation MicroScanner Logging Responses to Lithology in Guyot Carbonate Platforms and their Implications: sites 865 and 866: Proc. Ocean Drilling Program Science Results, v. 143, p. 329-372.

Coulde, S. R., and E. Pottier, 1996, A Review of Target Decomposition Theorems in Radar Polarimetry: IEEE Transactions on Geosciences and remote sensing v. 34, p. 498-518.

Cuddy, S., 2000, Lithofacies and Permeability Prediction from Electrical Logs Using Fuzzy Logic: Society of Petroleum Engineers Reservoir Evaluation and Engineering, v. 3, p. 319-324.

Curlander, J., and W. Kober, 1992, Rule Based System for Thematic Classification in SAR Imagery: Proc. IGARSS. IEEE Press, New York, p. 854-856.

Curtis, A., and R. Wood, 2004, Geological Prior Information; Informing Science and Engineering: Geological Society of LOndon Special PUblications, v. 239.

Darwish, A., K. Leukert, and W. Reinhart, 2003, Image Segmentation for the Purpose of Object-Based Classification, Proceedings of IGARSS 2003 IEEE, Toulouse.

Delfiner, P., O. Peyret, and O. Serra, 1987, Automatic Determination of Lithofacies from Well Logs: SPE Formation Evaluation, v. 2, p. 303-310.

Delhomme, J. P., 1992, A Quantitative Characterization of Formation Heterogeneities Based on Borehole Image Analysis, 33rd Annual. Logging Symposium, Society of Professional Well Logging Analysts.

Derek, H., R. Johns, and E. Pasternack, 1990, Comparative Study of a Backpropagation Neural Network and Statistical Pattern Recognition in Identifying Sandstone Lithofacies: Conference on Artificial Intelligence in Exploration and Production A &M, p. 41-49.

Doveton, J. H., ed., 1994, Geologic Log Analysis Using Computer Methods: American Association of Petroleum Geology Computer Applications in Geology, v. 2.

Dubois, M. K., G. C. Bohling, and Chakrabarti, 2005, Comparision of Rock Facies Classification using Three Statistically Based Classifiers: Kansas Geological Survey, KGS Open File Report 2004-64.

Duda, R. O., P. E. Hart, and D. G. Stork, 2001, Pattern Classification, New York, Wiley.

Erlandsen, S. M., 2000, Production Experience from Smart Wells in the Oseberg Field, SPE Annual Technical Conference and Exhibition, Dallas, TX.

Elphick, R. Y., and W. R. Moore, 1999, Permeability Calculations from Clustered ElectroFacies, A Case Study in Lake Maracaibo Venezuela, SPWLA 40th Annual Logging Symposium.

Fagerberg, J., D. Mowery, and B. Verspagen, 2009, Innovation, Path Dependency, and Policy. The Norwegian Case, Oxford University Press.

Gaillot, P., T. Brewer, P. A. Pezard, and E.-C. Yeh, 2007, Contribution of Borehole Digital Imagery In Core-Log-Seismic Integration: J. Scientific Drilling, v. 5, p. 50-53.

Gamanya, R., P. De Maeyer, and M. De Dapper, 2007, An Automated Satellite Image Classification Design Using Object-Oriented Segmentation Algorithms: A Move Towards Standardization: Expert Systems with Applications, v. 32, p. 616-624.

Geng, H. J., G. W. Wang, J. Li, Q. Hong, and M. J. Qin, 2002, Image Interpretation Modes and the Typical Interpretation Chart for Imaging Well Logging: JOurnal of Jianghan Petroleum Institute, v. 24, p. 26-29.

Gill, D., A. Shomrony, and H. Fl, 1993, NUmerical Zonation of Log Studies and Logfacies Recognition by Multivariate Clustering: AAPG Bulletin, v. 77.

Goodall, T., N. K. Moller, and T. M. Ronningsland, eds., 1998, The Integration of Electrical Image Logs with Core Data for Improved Sedimentological Interpretation: Core-Log Integration, v. 136, Geological Society, London, Special Publications, 237-248 p.

Gopal, S., and C. Woodcock, 1996, Remote Sensing of Forest Change Using Artificial Networks: IEEE Transactions on Geosciences and remote sensing, v. 34, p. 398-404.

Graue, E., W. Helland-Hansen, J. Johnsen, L. Lomo, A. Nottvedt, K. Ronning, A. E. Ryseth, and R. Steel, 1987, Advance and Retreat of the Brent Delta System, Norwegian North Sea: in Brooks J. &

Glennie K.. Petroleum Geology of North West Europe. Graham & Trotman, p. 915–937.

Gurney, K., 1997, An Introduction to Neural Networks, UCL Press.

Hall, J., M. Ponzi, M. Gonfalini, and G. Maletti, 1996, Automatic Extraction and Characterization of Geological Features and Textures from Borehole Images and Core Photographs: SPWLA 37th Annual Logging Symposium

Haller, D., and F. Porturas, 1998, How to Characterise Fractures in Reservoirs using Borehole and Core Images: Case Studies. In: Harvey, P. K. & Lovell, M. A. (eds.): Geological Applications of Wireline Logs, Geological Society Special Publication Classic, p. 3-10.

Haralick, R. M., 1979, Statistical and Structural Approaches to Texture: Proceeding of the IEEE, v. 67, p. 786-804.

Haralick, R. M., K. Shanmugam, and I. Denstien, 1973, Textural Features for Image Classification: IEEE Transactions on Systems, Man and Cybernetics, v. 6, p. 610-621.

Harris, D. A., J. J. M. Lewis, and D. J. Wallace, 1993, The Identification of Lithofacies types in Geological Imagery Using Neural Networks: Eurocaipep, p. 20-22.

Hauger, E., R. Lovlie, and P. Van Veen, 1994, Magneteostratigraphy of the Middle Jurassic Brent Group in teh Oseber Oil Field, Northern North Sea: Mar. Petroleum Geology, v. 11, p. 375-388.

Haverkamp, D., and C. Tsatsoulis, 1992, The Use of Expert Systems in Combination with Active and Passive Microwave Data to Classify Sea Ice: NASA Report, p. 1625-1627.

Hay, G., J.,, P. Dube, A. Bouchard, and D. Marceau, J., 2001a, A Scale-Space Primer for Exploring and Quantifying Complex Landscapes.: Ecological Modelling, v. 153, p. 27-49.

Hay, G., J.,, D. Marceau, J., P. Dube, and A. Bouchard, 2001b, A Multiscale Framework for Landscape Analysis: Object-Specific Analysis and Upscaling: Landscape Ecology, v. 16, p. 471-490.

Hay, G., J.,, K. O. Niemann, and D. Goodenough, G., 1997, Spatial Thresholds, Image-Objects and Upscaling: A Multi-Scale Evaluation: Remote Sensing of Environment, v. 62.

Hay, G., J.,, K. O. Niemann, and G. McLean, 1996, AN Object-Specific Image-Texture Analysis of H-Resolution Forest Imagery: Remote Sensing of Environment, v. 55, p. 108-122.

Helland-Hansen, W., M. Ashton, L. Lomo, and R. Steel, 1992, Advance and Retreat of the Brent Delta: Recent Contributions to the Depositional Model: In: Geology of the Brent Group (Ed. by A.C. Morton, R.S. Haszeldine, M.R. Giles and S. Broom), Geological Society Special Publication, v. 61, p. 109-127.

Horng, M. H., X. J. Huang, and J. H. Zhuang, 2003, Texture Feature Coding Method for Texture Analysis and It's Application: Journal of Optical Engineering, v. 42, p. 228-238.

Hruska, M., W. Corea, D. Seeburger, W. Schweller, and W. H. Crane, 2009, Automated Segmentation of Resistivity Image Logs Using Wavelet Transform: Mathematical Geoscience, v. 41, p. 703-716.

Hua, C., L. Ning, X. Chengwen, L. Xingli, L. Duoli, W. Caizhi, and W. Dacheng, 2009, Automatic Discrimination of Sedimentary Facies and Lithologies in Reef-Bank Reservoirs Using Borehole Image Logs: Applied Geophysics, v. 6, p. 17-29.

Hurley, N., ed., 2004, Borehole Images: Basic Well Log Analysis, v. 16, AAPG Methods in Exploration Series, 151-163 p.

Hurley, N. F., and T. Zhang, 2009, Method for Characterizing a Geological Formation Traversed by a Borehole, Unites States Patent Application Publication, Schlumberger Technology Corporation, Cambridge, MA (US).

Hurley, N. F., and t. Zhang, 2009, Method to Generate Fullbore Images Using Borehole Images and Multipoint Statistics, SPE 120671: Society of Petroleum Engineers, presented at Middle East Oil and Gas Show and Conference, Bahrain.

Johannessen, E. P., and A. Nottvedt, 2008, Norway Encircled by Coastal Plains and Deltas: In Ramberg, I. B. and Nottvedt, A., The Making of a Land - Geology of Norway. NGF, p. 356-383.

Ke, S. Z., 2008, Full 3-D Numerical Modeling of Borehole Electric Image Logging and The Evaluation Model of Fracture: Science in China Series D-Earth Sciences, v. 51, p. 170-173.

Knecht, L., B. V. Jacques, J. P. Leduc, and B. Mathis, 2004, Improved Formation Evaluation In Thin Beds Using Petrophysical Images, SPWLA 45th Annual Logging Symposium, Noordwijk, The Netherlands.

Knecht, L., B. Mathis, J.-P. Leduc, T. Vandenabeele, and R. D. Cuia, 2003, Electrofacies and Permeability Modeling in Carbonate Reservoirs Using Image Texture Analysis and Clustering Tools, Society of Petrophysics and Well Log Analysts (SPWLA) 44th Annual Looging Symposium.

Kohonen, T., 1984, Self-Organising and Associative Memory: Springer Series in Information Sciences, v. 8: New York, Springer-Verlag.

Kowalik, W. S., W. C. Corea, W. H. Crane, and W. J. Schweller, 2009, Automated Borehole Image Interpretation, United States Patent, USA, Chevron U.S.A. Inc, San Ramon, CA (US).

Kraipeerapun, P., C. C. Fung, and K. W. Wong, 2006, Lithofacies Classification from Well Log Data using Neural Networks, Interval Neutrosophic Sets and Quantification of Uncertainty: Proceedings of World Academy of Science, Engineering and Technology, Vol 16, p. 280-284.

Kuchinski, R., and P. Kalathingal, 2010, Expanding the Role of Resistivity Image Logs Using Improved Acquisition and Interpretation Techniques, Society of Petroleum Engineers, Tunis, Tunisia.

Laws, K. I., 1980, Testural Image Segmentation: Technical Report USCIPI Report 940, Dept of Electrical Engineering., Image Processign Institute, University of Southern Californica, Los Angeles, January 1980.

Leduc, J. P., V. Delhaye-Prat, P. Zaugg, B. Mathis, and A. Leyay, 2002, FMI Based Sedimentary Facies MOdeling Surmont Lease, Presented at the 75th CSPG Convention, Athabasca, Vanada.

Li, C. L., and C. C. Zhou, 2008, A new Method to Calculate Lithological Profile with Micro-Resistivity Imaging Log: Well Logging Technology, v. 32, p. 45-48.

Linek, M., 2003, Interpretation of FMS Image Data Referring to pore space analysis of continential Flood Basalts, an Example of ODP hole 917 A, East Greenland Margin, Technische Universitat, Bergakademine Frieberg, Germany.

Linek, M., M. Jungmann, T. Berlage, R. Pechnig, and C. Clauser, 2007, Rock Classification Based on Resistivity Patterns in Electrical Borehole Wall Images: Journal of Geophysics and Engineering, v. 4, p. 171-183.

Lofts, J. C., and L. T. Bourke, eds., 1999, The Recognition of Artefacts form Acoustic and Resistivity Borehole Imaging Devices: Borehole Imaging: Applications and Case HIstories, v. 159, Geological Society Special Publication, 59-76 p.

Loseth, T. M., A. E. Ryseth, and M. Young, 2009, Sedimentology and Sequence Stratigraphy of the Middle Jurassic Tarbert Formation, Oseberg South Area (Northern North Sea): Basin Research, v. 21, p. 597-619.

Lovell, M. A., P. K. Harvey, T. S. Brewer, C. Williams, P. D. Jackson, and G. Williamson, 1997, Application of FMS Images in the Ocean Drilling Program: An Overview: (in Geological Evolution of Ocean Basins: Results form the Ocean Drilling Program): Geological Society Special Publications, v. 131.

Luthi, S. M., 1990, Sedimentary Structures of Clastic Rocks Identified from Electrical Borehole Images: Geological Applications of Wireline Logs, v. 48, p. 3-10.

Luthi, S. M., 1994, Textural Segmentation of Digital Rock Images into Bedding Units using Textural Energy and Cluster Labels: Mathematical Geology, v. 26, p. 181-196.

Luthi, S. M., 2001, Geological Well Logs, Their Us ein Geological Modelling: Springer-Verlag Berlin and Heidelberg.

Ma, X. P., J. L. Zhang, and H. J. Zhao, 2009, Application of Artificial Neural Networks in Lithofacies Interpretation Used for 3D Geological Modelling: 2009 Isecs International Colloquium on Computing, Communication, Control, and Management, Vol Iv, p. 451-454.

Machecler, I., and J.-P. Nadal, 2004, Pre-attentive segmentation of oriented textures: Journal of Geophysics and Engineering, v. 1, p. 312-326.

Maddock, R., and R. Ravnas, 2010, Applications of Oil-Base Mud Earth Imager for a High Temperature and High-Pressure Exploration Well, in M. Poppelreiter, Garcia-Carballido, and Kraaijveld, M., ed., Dipmeter and Borehole Image Log Technology: AAPG Memoir 92, p. 129-144.

Maiti, S., R. K. Tiwari, and H. J. Kumpel, 2007, Neural Network Modelling and Classification of Lithofacies Using Well Log Data: A Case Study from KTB Borehole Site: Geophysical Journal International, v. 169, p. 733-746.

Martin, R., 2004, Automated Lithofacies Predictions from Well Logs: PhD Thesis thesis, University of Edinburgh, Edinburgh, 343 p.

Martinius, A. W., C. R. Geel, and J. Arribas, 2002, Lithofacies Characterization of Fluvial Sandstones from Outcrop Gamma-Ray Logs (Loranca Basin, Spain): The Influence of Province: Petroleum Gecoscience, v. 8, p. 51-62.

Masters, T., 1993, Principle Neural Network Tecipes in C+, Academic Press.

Mathis, B., j. P. Leduc, and T. Vandenabeele, 2003, From the Geologists' Eye to the Synthetic Core Descriptions: Geological Log Modeling Using Well-Log Data, AAPG Annual Meeting, Salt Lake City, Utah.

Mathis, B., J. P. Leduc, and T. Vandenabeele, 2004, From the Geologists' Eye to the Synthetic Core Descriptions: Geological Log

Modeling Using Well-Log Data, AAPG Annual Meeting, Salt Lake City, Utah.

Melrose_Resources_plc, 2004, Annual Report and Accounts.

Melrose_Resources_plc, 2008, Shareholder and Analysts Visit to Egypt.

Metzler, V. a. T., C, 2002, A Noval Object-Oriented Approach to Image Analysis and Retrieval: Fifth IEEE Southwest Symposium on Image Analysis and Interpretation (SSIAI'02).

Mirowski, P., 2005, System and Method for Inferring Geological Classes, in U. Patent, ed., UK patent GB 2 397 664 B, UK.

Mitchell, T., 1997, Machine Learning, McGraw-Hill International Publishing.

Norwegian_Petroleum_Directorate, OLJEDIREKTORATET . Oseberg.

NPD, Statfjord Formation: The NPD's Fact Pages.

Onu, C., P. Buffer, J. Lofts, and S. Morris, 2008, Sedimentological Characterization and Application of a High-Definition While Drilling Borehole Electrical Imager, Brent Group, North Sea, SPWLA 49th Annual Logging Symposium, Edinburgh, Scotland.

Ozkaya, S. I., 2003, Fracture Length Estimation from Borehole Image Logs: Mathematical Geology, v. 35, p. 737-753.

Passey, Q. R., K. E. Dahlberg, K. B. Sullivan, H. Yin, R. A. Brackett, Y. H. Xiao, and A. G. Guzman-Garcia, 2006, Petrophysical Evaluation of Hydrocarbon Pore-Thickness in Thinly Bedded Clastic Reservoirs, in N. AAPG Archie Series, ed., Chapter 9, Borehole Image Logs in Thinly Bedded Reservoirs, p 109-131, AAPG Special Volumes.

Pezard, P., M. Lovell, and R. Hiscott, 1992, Downhole Electrical Images in Volcaniclastic Sequences of the Izu-Bonin Forearc Basin, Western Pacific: Proc. Ocean Drilling Program Science Results, v. 126, p. 603-623.

Pierce, E., F. Ulaby, K. Sarabandi, and M. Dobson, 1994, Knowledge Based Classification of Pllarimetric SAR Images: IEEE Transactions on Geosciences and remote sensing v. 30, p. 697-705.

Polson, D., and A. Curtis, 2010, Dynamics of Uncertainty in Geological Interpretation: Journal of the Geological Society, London, v. 167, p. 5-10.

Poppelreiter, M., C. Garcia-Carballido, and M. A. Kraaijveld, eds., 2010, Dipmeter and Borehole Image Log Technology: AAPG Memoir 92.

Prensky, S. E., ed., 1999, Advances in Borehole Technology and Applications: Borehole Imaging: Applications and Case HIstories, v. 159, Geological Society Special Publications, 1-43 p.

Price, D., A. Curtis, and R. Wood, 2008, Statistical Correlation between Geophysical Logs and Extracted Core: Geophysics, v. 73, p. E97-E106.

Prioul, R., and J. Jocker, 2009, Fracture Characterization at Multiple Scales Using Borehole Images, Sonic Logs, and Walkaround Vertical Seismic Profile: Aapg Bulletin, v. 93, p. 1503-1516.

Prosser, J., S. Buck, S. Saddler, and V. Hilton, 1999, Methodologies for Multi-Well Sequence Analysis Using Borehole Image and Dipmeter Data, in M.A. Lovell, Williamson, G., Harvey P.K., ed.,Borehole Imaging: Applications and Case Histories.: Geological Society Special Publication, v. 159, p. 91-121.

Rabiller, P., and L. Schulbaum, 2001, Sedimentary bodies Identification Using the Phase Coefficients of the Wavelet Transform, SPWLA 42nd Annual Logging Symposium.

Rabiller, P., N. Keskes, and S.-J. Ye, 1997, Automatic High Resolution Sedimentary Dip Detection on Borehole Imagery, SPWLA 38th Annual Logging Symposium.

Rankey, E. C., and J. C. Mitchell, 2003, That's Why It's Called Interpretation: The Role of Horizon Uncertainty On Seismic Attribute Analysis: Leading Edge, v. 22, p. 820-828.

Reed, T. R., and J. M. Hans Du Buf, 1993, A review of recent texture segmentation and feature extraction techniques: Computer Vision, Graphics, and Image Processing: Image Understanding, v. 57, p. 359-372.

Reid, R. R., and M. B. Enderlin, 1998, True Pay Thickness Determination of Laminated Sand and Shale Sequence Using Borehole Resistivity Image Logs, SPWLA 39th Annual Logging Symposium.

Rich, E., and K. Knight, 1991, Artificial Intelligence, McGraw-Hill College.

Userguide_eCognition, 2003.

Rider, M., 2004, The Geological Interpretation of Well Logs, Whittles Publishing.

Rider, M., T. Goodall, and T. Dodson, 1999, A Pre-Development Turbidite Reservoir Evaluation Using FMS Electrical Images: in, M.A. Lovell, Williamson, G., Harvey P.K., ed.,Borehole Imaging: Applications and Case Histories, ed, Geological Society Special Publications, v. 159, p. 123-137.

Roger, S. J., J. H. Fang, C. L. Karr, and D. A. Stanley, 1992, Determination of Lithology from Wireline Well Logs using a Neural Network: American Association of Petroleum Geologist's Bulletin, v. 76, p. 731-739.

Rojas, R., 1996, Neural Networks, Springer-Verlag, Berlin.

Roumi, M., 2009, Implementing Texture Feature Extraction Algorithms on FPGA: MSc Thesis thesis, Delft University of Technology, Mekelweg.

Russell, S. D., M. Akbar, B. Vissapragada, and G. M. Walkden, 2002, Rock Types and Permeability Prediction from Dipmeter and Image Logs: Shuaiba reservoir (Aptian), Abu Dhabi: Aapg Bulletin, v. 86, p. 1709-1732.

Ryseth, A., 2000, Differential Subsidence in the Ness Formation (Bajocian), Horda Platform Area, Northern North Sea: Facies Variability, Accommodation Space Development and Sequence Stratigraphy in a Deltaic Distributary System: Norwegian Journal of Geology, v. 80, p. 9-26.

Ryseth, A., H. Fjellbirkelano, I. Osmundsen, O. Skaalnes, and E. Zachariassen, 1998, High-Resolution Stratigraphy and Seismic Attribute Mapping of a Fluvial Reservoir Unit: Ness Formation, Oseberg Field: Aapg Bulletin, v. 82, p. 1627-1651.

Schiewe, J., 2002, Segmentation of High-Resolution Remotely Sensed Data - Concepts, Applications and Problems, Symposium on geospatial theory, Processings and applications, Ottawa.

Schlumberger, 1994, FMI Fullbore Formation MicroImager: Schlumberger Educational Services.

Scott, E., 1992, The Paleoenvironments and Dynamics of the Rannoch-Etive Nearshore and Coastal Successions, Brent Group, Northern North Sea: In: Geology of the Brent Group (Ed. by A.C. Morton, R.S. Haszeldine, M.R. Giles and S. Broom), Geological Society Special Publication, v. 61, p. 129-148.

Serpico, S., and F. Roli, 1995, Classification of Multisensor Remote Sensing Images by Structured Neural Networks: IEEE Transactions on Geosciences and remote sensing v. 33, p. 562-577.

Serra, J., 1982, Image Analysis and Mathematical MOrphology: Academic Press.

Serra, O., 1989, Formation MicroScanner Image Interpretation: Schlumberger Education Services, Houston, 117.

Sognesand, S., 1997, Reservoir Management of the Oseberg Field During Eight Years' Production, offshore Europe: Continuous Change : Learning from the 21st Century, Aberdeen.

Sun, Q., Y. Liang, Q. Tan, and S. Zhang, 2009, Research on Vehicle Information Extraction from High-Resolution Satellite Images, Proceedings of the 9th International Conference of Chinese Transportation Professionsla (ICCTP 2009), p. 1825-1831.

Thapa, B. B., P. Hughett, and K. Karasaki, 1997, Semi-Automatic Analysis of Rock Fracture Orientations from Borehole Wall Images: Geophysics, v. 62, p. 129-137.

Torres, D., R. W. Strickland, and M. V. Gianzero, 1990, A New Approach to Determining Dip and Strike Using Borehole Images, SPWLA 31st Annual Logging Symposium.

Tsatsulis, C., 1993, Expert Systems in Remote Sensing Applications: IEEE Geosciences and remote sensing Newsletter June, p. 7-15.

Tuceryan, M., and A. K. Jain, eds., 1998, Texture Analysis The Handbook of Pattern Recognition and Computer Vision, v. Chapter 2.1: New York, World Scientific, 207-248 p.

Tyagi, A. K., and A. Bhaduri, 2002, Porosity Analysis Using Borehole Electrical Images In Carbonate Reservoirs, 43rd Annual Logging Symposium, Society of Professional Well Logging Analysts.

Ursula C. Benz, P. H., Gregor Willhauck, Iris Lingenfelder, Markus Heynen, 2003, Multi-resolution, object-oriented fuzzy analysis of remote sensing data for GIS-ready information, Definiens Imaging GmbH, Trappentreustr. 1, D-80339 Munich, Germany.

Userguide_eCognition, 2003.

Van De Wouver, G., 1998, Wavelets for multiscale: PhD Thesis thesis, University of Antwerp.

Van Gool, L., P. Dewaele, and A. Oosterlinck, 1985, Texture Analysis Anno 1983: Computer Vision, Graphics, and Image Processing, v. 29, p. 336-357.

Wadge, G., D. Benaouda, G. Ferrier, R. B. Whitmarsh, R. G. Rothwell, and C. Macleod, eds., 1998, Lithological Classification within ODP Holes using Neural Network Trained from Integrated Core-Log Data. : Core-Log Integration, v. 136, Geological Society Special Publication, 129-140 p.

Wang, X., and N. D. Georganas, 2009, GLCM Texture Based Fractal Method for Evaluating Fabric Surface Roughness: IEEE Trans. On Instrumentation and Measurements, v. 99, p. 1-13.

www.oilegypt.com, 2005.

Xie, X., 2008, A review of Recent Advances in Surface Defect Detection using Texture Analysis Techniques: Electronic Letters on Computer Vision and Image Analysis, v. 7, p. 1-22.

Ye, S.-J., P. Rabiller, and N. Keskes, 2001, Method for Automatic Detection of Planar Heterogeneities Crossing the Stratification of an Environment, in U. S. Patent, ed., Elf Exploration Production (FR).

Ye, S.-J., and P. Rabiller, 2000, A New Tool for Electro-Facies Analysis: Multi-Resolution Graph-Based Clustering, SPWLA 41th Annual Logging Symposium.

Ye, S. J., P. Rabiller, and N. Keskes, 1998, Automatic High Resolution Texture Analysis on Borehole Imagery, SPWLA 39th Annual Logging Symposium.

Ye, S.-J., P. Rabiller, and N. Keskes, 1997a, Automatic High Resolution Sedimentary Dip Detection on Borehole Imagery: SPWLA 38th Annual Logging Symposium.

Ye, S. J., J. Shen, N. Keskes, and P. Rabiller, 1997b, Sinusoid Recognition and Texture Analysis of Electrical Borehole Images: Scia '97 - Proceedings of the 10th Scandinavian Conference on Image Analysis, Vols 1 and 2, p. 339-346.

Ye, S.-J., Shen, J., and Keskes, N.,, 1995, Automatic identification of beddignplanes from electrical borehole images: 9th Scandinavian conference on image analysis.

Yielding, G., M. E. Badley, and A. M. Roberts, 1992, The Strutural Evolution of Brent Province: in: Geology of the Brent Group (Ed. by A.C. Morton, R.S. Haszeldine, M.R. Giles and S. Broom), Geological Society Special Publication, v. 61, p. 27-43.

Zhang, Y., and T. Maxwell, 2006, A Fuzzy Logic Approach to Supervised Segmentation for Object Oriented Classification, ASPRS 2006 Annual Conference Reno, Nevada.

Zhang, J., and T. Tan, 2002, Brief Review of Invariant Texture Analysis Methods: Pattern Recognition, v. 35, p. 735-747.

Zhang, Y. J., 2005, Image Analysis, Beijing, Tsinghua University Press.

Zhang, Y., H. A. Salisch, and J. G. McPherson, 1999, Application of Neural Networks to Identify Lithofacies from Well Logs: Exploration Geophysics, v. 30, p. 45-49.